LABORATOIRE EUROPÉEN POUR LA PHYSIQUE DES PARTICULES
CERN EUROPEAN LABORATORY FOR PARTICLE PHYSICS

CERN-LHC-2008-XXX
MoEDAL-TDR 1.0
June 8, 2009

MoEDAL

$$\nabla.\mathbf{E} = 4\pi\rho_e$$

$$\nabla.\mathbf{B} = 4\pi\rho_m$$

$$-\nabla\times\mathbf{E} = \tfrac{1}{c}\tfrac{\partial\mathbf{B}}{\partial t} + \tfrac{4\pi}{c}\mathbf{j_m}$$

$$\nabla\times\mathbf{B} = \tfrac{1}{c}\tfrac{\partial\mathbf{E}}{\partial t} + \tfrac{4\pi}{c}\mathbf{j_e}$$

$$\mathbf{F} = q_e\left(\mathbf{E} + \tfrac{\mathbf{v}}{c}\times\mathbf{B}\right) + q_m\left(\mathbf{B} - \tfrac{\mathbf{v}}{c}\times\mathbf{E}\right)$$

TECHNICAL DESIGN REPORT OF THE MoEDAL EXPERIMENT

CERN-LHCC-2009-006 / MoEDAL-TDR-001
08/06/2009

The MoEDAL Collaboration

- The University of Alberta, Edmonton, Alberta (Canada)
  J. L. Pinfold [1] *, R.Soluk, Y, Yao*

- Physics Department of the University of Bologna INFN Section of Bologna, viale Berti Pichat 6/2, 40127 Bologna (Italy)
  S. Cecchini, G. Giacomelli, M. Giorgini, L. Patrizii, G. Sirri

- CERN, Geneva (Switzerland)
  D. H. Lacarrère

- The University of Cincinnati, Cincinnati, Ohio (USA)
  K. Kinoshita

- Institute of Experimental and Applied Physics (IEAP), Czech Technical University in Prague, Prague, Horsk 3a/22, 128 00 Praha 2 (Czech Republic)
  J. Jakůbek, M. Platkevič, S. Pospíšil, Z. Vykydal

- DESY, Hamburg (Germany)
  T. Hott

- The University of Montreal, Montreal, Quebec (Canada)
  A. Houdayer, Claude Leroy

- Northeastern University, Boston, Massachusetts (USA)
  J. Swain

- Institute for Space Sciences, P.O.Box MG-23, Ro 077125, Bucharest-Măgurele, (Romania)
  D. Felea, D. Haşegan, G. E. Păvălaş and V. Popa.

[1]Spokesman and contact person - **J. L. Pinfold**: pinfold@phys.ualberta.ca

Technical Design Report of the MoEDAL Experiment

S. Cecchini (2), G. Giacomelli (2), D. Felea (9), M. Giorgini (2), D. Hasegan (9), T. Hott (6), A. Houdayer (6), J. Jakůbek (4), K. Kinoshita (5), D. H. Lacarrère (3), C. Leroy (6), L. Patrizii (2), G. E. Pavalas (9), J. L. Pinfold (1), M. Platkevič (4), S. Pospíšil (4), V. Popa (9), R. Soluk (1), G. Sirri (2), J. Swain (8), E, Z. Vykydal (4), Y. Yao (1).

(The MoEDAL Collaboration)

1. University of Alberta, Edmonton, Canada
2. University of Bologna, Bologna, Italy
3. CERN, Geneva, Switzerland
4. IEAP, Czech Technical University in Prague, Czech Republic
5. University of Cincinnati, Cincinnati, Ohio, USA
6. DESY, Hamburg, Germany
7. University of Montreal, Montreal, Canada
8. Northeastern University, Boston, Massachusetts, USA.
9. Institute of Space Sciences, Bucharest, Romania

Contents

1 Overview **1**

1.1 Physics Program . . . 2

1.1.1 The Search for the Magnetic Monopole . . . 2

1.1.2 SMPs with Single Electrical Charge . . . 7

1.1.3 SMPs with Multiple Electrical Charge . . . 11

1.2 Signal and backgrounds . . . 14

1.2.1 Physics Impact . . . 15

1.3 Physics and Detector Simulation . . . 17

1.3.1 Magnetic Monopole Simulation . . . 18

1.3.2 Simulation of Microscopic Black Hole Remnant Production . . . 19

1.3.3 Detector Simulation . . . 19

1.4 Experimental Overview . . . 20

1.4.1 Track-Etch Detectors . . . 20

1.4.2 Data taking and analysis . . . 23

1.4.3 Proposed run scenario . . . 25

2 The MoEDAL Detector **26**

2.1 Track Etch Detector Properties . . . 28

2.2 Detector Unit Design . . . 30

2.3 Detector mounting system . . . 31

2.4 Detector installation . . . 32

2.5 MoEDAL Radiation Environment . . . 33

2.5.1 Activation and Intervention . . . 36

2.5.2 Radiation Tolerance of Nuclear track Etch Detectors . . . 41

2.5.3 Monitoring of Radiation Levels in the VELO/MoEDAL Cavern . . . 41

2.6 Interface/integration/interference Issues With LHCb and With the LHC machine . . . 42

2.6.1 LHCb Experimental Area - Brief Description and Environmental Constraints . . . 42

2.6.2 Interference Issues with LHCb Experiment . . . 44

2.6.3 Integration at the VELO area (RB84) . . . 45

2.6.4 Interference Issues with LHC Machine . . . 46

3 Plastic Etching, calibration and Signal Extraction **48**

3.1 Etching of plastic track etch detectors . . . 48

3.2 Calibration 49
3.3 Signal Extraction 51

4 Safety Issues and Irradiated Plastic Handling 53

4.1 Plastic Flammability 53
4.2 Irradiated Plastic handling 53

5 Project Planning 56

5.1 Organization 56
5.2 Responsibility for Construction and Installation, Plastic Analysis and Radiation Monitoring 58
5.3 Construction/Installation Schedule and Budget 58
5.4 Request for experimental conditions and other support 59

Appendices 60

A MoEDAL - A Heavy-Ion Running Scenario 60

A.1 Searching for Magnetic Monopoles with Heavy Ions 60
A.2 Detecting Strangelet Production 60
A.3 Searching for Q-balls 62
A.4 Search for Abnormal Nucleus Production 62

B Chemical and Physical Properties of the MoEDAL NTDs 62

B.1 The Polyallyl Diglycol Carbonate Polymer CR 39 62
B.2 Lexan/Makrofol 63

1 Overview

In 2009 the LHC will open up a new energy regime in which we can search for new physics beyond the Standard Model. The search strategy for exotics planned for the main LHC detectors can be extended with dedicated experiments designed to enhance, in a complementary way, the physics reach of the LHC. The MoEDAL (Monopole and Exotics Detector at the LHC) project is such an experiment. The prime motivation of MoEDAL is to directly search for the Magnetic Monopole and other highly ionizing Stable (or pseudo-stable) Massive Particles (SMPs) at the LHC.

If massive long-lived charged, multiply charged or magnetically charged particles exist and are produced at the LHC they may travel with a velocity significantly slower than the speed of light. The main LHC experiments are designed to detect conventionally charge particles produced with a velocity (β =v/c) large enough to fall into LHC trigger window of 25 ns. One of the principal constraints on the design of a collider experiment and its ability to measure slow-moving SMPs is the bunch crossing time. The LHC crossing time of 25 ns, is considerably shorter than that at LEP (25μs), the Tevatron (396 ns) or HERA (96 ns). For an SMP at the LHC to be detected, or triggered on, in a certain detector system and be associated to the correct bunch crossing, it should arrive at most 25 ns after the default arrival time of a particle traveling at the speed of light [1][2]. Later arrival would imply triggering or detection within the next crossing time window. The large size of the ATLAS and CMS detectors[2] ensures that this will be an important source of inefficiency in detecting SMPs. For example, it is only possible to reconstruct the track of a slowly moving SMP in the ATLAS central muon chambers within the correct bunch crossing window if $\beta \gtrsim 0.5$ [1].

Very highly ionizing particles can be absorbed before they penetrate the detector fully. Even if penetration is sufficient to register the particle's passage further problems in measuring dE/dx for unknown massive particles could arise due to saturation of the electronics used in the tracking detectors. For such searches the electronics must have a wide enough dynamic range otherwise large values of dE/dx become unmeasurable due to saturation. This is particularly true for magnetic monopoles, for which dE/dx is significantly larger than that for electrically charged particles, but may already play a role for slow electrically charged ones. Although saturated hits have a tracking resolution much worse than that of typical unsaturated data, the presence of many saturated channels is itself a distinctive feature of the presence of a high-mass charged particle. Saturation of electronics as a consequence of highly ionizing particles may in particular have a non-negligible effect in the future LHC collider experiments where the resulting dead time as a result of electronics saturation may be of the order of the bunch crossing time.

Even if the SMP travels through the detector within the appropriate timing window, additional problems may arise from its low velocity. The sampling time and reconstruction software of each sub-detector is optimised assuming particles travelling at luminal speed. Hence, the quality of the read-out signal or reconstructed track or cluster may be degraded for an SMP, especially for sub-systems far away from the interaction point. Detector simulations so far suggest that it will still be possible to trigger and measure slowly moving particles at ATLAS and CMS [3][1]. However, this is an area which must continue to be studied as the simulation programs are further developed and the detectors better understood.

The MoEDAL experiment will complement the search capabilities of the general purpose LHC detectors allowing searches for electrically and magnetically charged SMPs with Z/β - actual or effective - potentially as low as 5, where Z is the electric charge. The present upper limit on the SMP electric charge to which ATLAS and CMS will be sensitive is

[2]The central ATLAS and CMS muon chambers extend to 10 and 7 m, respectively

still unclear. However, it is likely to be substantially below the reach of MoEDAL. The MoEDAL experiment bypasses the experimental challenges of detecting magnetic monopoles with active detectors, by using the passive plastic track technique which does not require a trigger. Also, track-etch detectors provide a tried and tested method to detect and accurately measure the track of a highly ionizing particle and also its Z/β. Importantly, heavy-ion beams provide a demonstrated calibration technique using energy depositions very similar to that of the hypothetical particles sought.

Our acceptance calculations indicate that MoEDAL will have a calibrated sensitivity to monopoles with a mass of several TeV and a magnetic charge as high as three ($3g_D$). In addition, our Nuclear Track Detectors (NTDs) will be able to record the tracks of highly ionizing particles with magnetic/electric charges greater than $3g_D$ ($\equiv$ 206e), the detection of even one magnetic monopole that fully penetrated a MoEDAL NTD stack expected to be distinctive.

1.1 Physics Program

The search for highly ionizing SMPs at the LHC can be divided into three main categories. The first category is that of massive magnetically charged particles such as the magnetic monopole [4] [5] or the dyon [6].

Another open question in modern physics is the existence of SMPs with single electrical charge providing a 2nd category of particle that is heavily ionizing by virtue of its small β. The most obvious possibility for an SMP is that one or more new states exist which carry a new conserved, or almost conserved, global quantum number. SUSY with R-parity, extra dimensions with KK-parity, and several other models fall into this category. The lightest of the new states will be stable, due to the conservation of this new parity, and depending on quantum numbers, mass spectra, and interaction strengths, one or more higher-lying states may also be stable or meta-stable. The third class of hypothetical particle has multiple electric charge such as the black hole remnant [7], or long-lived doubly charged Higgs boson [8].

SMPs with magnetic charge, single or multiple electric charge and with Z/β as low as five can in principle be detected by the CR39 nuclear track detectors, putting them within the physics reach of the MoEDAL experiment.

Running in heavy-ion mode MoEDAL would be sensitive to: monopole production [9], [10],[11], [12]; strangelets [13], [14], [15], [16]; and, and Q balls [17] - as described in Appendix A. However, heavy-ion running to is not foreseen at Point 8, where MoEDAL is deployed.

1.1.1 The Search for the Magnetic Monopole

In 1931 Dirac introduced the magnetic monopole in order to explain the quantization of the electric charge, which follows from the existence of at least one free magnetic charge [18]. He established the basic relationship between the elementary electric charge e and the basic magnetic charge:

$$eg = n\hbar c/2 = ng_D \tag{1}$$

where n is an integer, n = 1, 2, ... The magnetic charge $g = ng_D$; $g_D = \hbar c/2e = 68.5e$ is called the unit Dirac charge. The existence of magnetic charges and of magnetic currents would symmetrize in form Maxwell's equations, but the symmetry would not be perfect since $e \neq g$. But, if the couplings are be energy dependent they could converge to a single common value at very high energies [19]

There is no real prediction of the mass of classical Dirac magnetic monopole. One may have a rough estimate assuming that the classical monopole radius is equal to the classical electron radius: from which $r_M = g^2/(m_M c^2) = r_e = e^2/m_e c^2$ from which $m_M = g^2 m_e/e^2 \approx n.4700.m_e = n.2.4$ GeV/c^2. Thus the mass should be relatively large and even larger if the basic charge is e/3 and if n > 1.

Grand Unification magnetic monopoles, with masses of the order of 10^{15} GeV are well beyond the reach of any presently conceivable man-made accelerator. Never-the-less there are models where monopoles could appear in a mass range accessible to the LHC. Examples include:

- The electroweak Cho-Maison monopole [20];
- The Troost-Vinciarelli monopole [21] with mass that depends on the matter field (10^4 GeV/c^2 with IVB matter fields, 10^2 GeV/c^2 with ρ matter fields and 50 GeV/c^2 with spin-1/2 matter fields);
- A Superstring model [22] where, monopoles/dyons with a mass low enough ($\sim$1 TeV/c^2) to be detected at the LHC are hypothesized.

Since 1931 searches for classical Dirac monopoles have been carried carried out at each new accelerator at the high energy frontier. Relatively simple search experiments were employed and recently also large collider detectors [5] were used. In fact, monopole searches have been carried out in e^+e^-, ep, $p\bar{p}$, and pp interactions at various high energy colliders. For example, searches at the Fermilab collider [23] seem to exclude MMs with masses up to 850 GeV. Experiments at the LEP2 collider excluded masses below 102 GeV [24]. The limits produced on magnetic monopole production depend on the physical process by which the monopole is presumed to be produced.

For example, for Dirac monopoles the most obvious mechanism is annihilation and pair production via the electromagnetic interaction. If one assumes a single-photon production process, then the amplitude for pair production is proportional to the magnetic charge. Ignoring higher order effects, one can then formulate a naive pair production cross section for monopoles of mass m, $\sigma_{D(m)}$, by multiplying the cross section for production $\mu^+\mu^-$ pair with invariant mass greater than $2m$ by the square of the charge ratio and making a phase space correction:

$$\sigma_{D(m)} = \left(\frac{g_D}{e}\right)^2 \times \sigma_{\mu\mu}(> 2m) \times (1 - 4\frac{m^2}{s}) \tag{2}$$

Monopole properties The main properties of magnetic monopoles are obtained from the Dirac relation. Many of the important properties of MMs are obtained from the Dirac relation and are summarized below:

- *Basic magnetic charge.* If n =1 and the basic electric charge is that of the electron, then the magnetic charge, $g_D = \hbar c/2e = 137e/2$, in general , $g_D = n\hbar c/2e$. The magnetic charge is larger if n > 1 and/or if the basic electric charge is e/3.
- *Electric charge.* Electrically charged monopoles (M), or dyons, may arise as quantum mechanical excitations or as M-p, M-nucleus composites.
- *Dimensionless magnetic coupling constant.* In analogy with the fine structure constant, $\alpha = e^2/cm \approx 1/137$, the dimensionless coupling constant is $\alpha_g = g_D^2/\hbar c \approx 34.25$. As it is greater than one, perturbative calculations cannot be used.
- *Spin.* The spin of the magnetic monopole is usually taken to be 1/2 or 0.

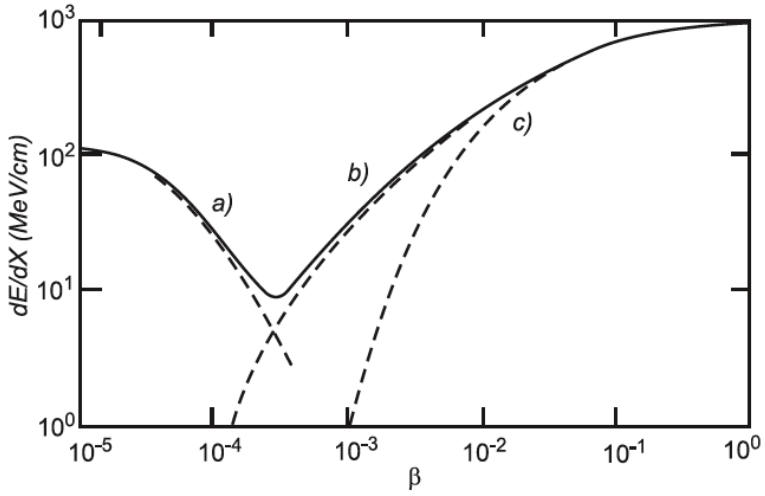

Figure 1: The energy losses in MeV/cm of a Magnetic Monopole with single magnetic charge, in liquid hydrogen, as a function of β. Curve a) corresponds to elastic monopole-hydrogen atom scattering; curve b) corresponds to interactions with level crossings; curve c) describes the ionization energy loss.

- *Energy W acquired in a magnetic field B.* $W = ng_D Bl = n \cdot 20.5\text{keV/G.cm}$. In a coherent galactic length ($l \sim 1$ kpc, $B \approx 3\mu$G), the energy gained by a magnetic monopole with $g = g_D$ is $W \approx 1.8 \times 10^{11}$ GeV. Classical poles and IMMs in the cosmic ray flux may be accelerated to relativistic velocities. GUT poles should have low velocities, $10^{-4} < \beta < 10^{-1}$.

- *Bending in a solenoidal field* . Detectors at colliders usually employ a solenoidal field because monopoles accelerate along field lines monopoles will curve in the non-bend plane of the solenoidal field (conventionally the r-z plane) and will not curve in the bend plane (conventionally the r-ϕ plane) of the magnetic field.

- *Trapping.* Magnetic Monopoles may be trapped in ferromagnetic materials by an image force, which could reach values of ~ 10 eV/$\mathring{A}$.

- *Bound systems.* The interaction of the magnetic charge of the magnetic monopole with a nuclear magnetic dipole could lead to the formation of a M-nucleus bound system. A monopole-proton bound state may be produced via radiative capture. Monopole-nucleus bound states may exist for nuclei with large gyromagnetic ratios.

- *Energy losses of fast poles.* A fast magnetic monopole with magnetic charge g_D and velocity $v = \beta$ c behaves like an electric charge $(ze)^{eq} = g_D/\beta$, the energy losses of fast monopoles are thus very large. Also, the energy loss of a moving magnetic monopole falls with β, in contradistinction to an electrically charged particle.

- *Energy losses of slow poles ($10^{-4} < \beta < 10^{-2}$)* . May be due to ionization or excitation of atoms and molecules of the medium ("electronic" energy loss) or to recoiling atoms or nuclei ("atomic" or "nuclear" energy loss). Electronic energy loss predominates for $\beta > 10^3$.

- *Energy losses at very low velocities* . MMs with $v < 10^{-4}$c cannot excite atoms; they can only lose energy in elastic collisions with atoms or with nuclei. The energy is released to the medium in the form of elastic vibrations and/or infrared radiation [25]. Figure 1 shows the energy loss in liquid hydrogen of a $g = g_D$ MM vs β [26].

- *Energy losses in superconductors.* If a pole passes through a superconducting ring, there will be a magnetic flux change of $\phi_B = 2\pi\hbar c/e$, yielding dE/dx ≈42 MeV/cm, independent of velocity.

- *Catalysis of nucleon decay.* The interaction of the GUT monopole core with a nucleon can lead to a reaction in which the nucleon decays (monopole catalysis of nucleon decay), i. e. $M + p \rightarrow M + e^+ + \pi^0$. The cross section for this process is of the order of magnitude of the core size, $\sigma \sim 10^{-56}$ cm^2, practically negligible. But the catalysis process could proceed via the Rubakov-Callan mechanism with a cross section of the order of the strong interaction cross section [27]. Obviously, GUT monopoles are far to heavy to be created by terrestrial accelerators.

- *Mass.* As we have seen above magnetic monopoles that are potentially detectable at a collider can have a range of masses. Thus, in the MoEDAL search we will treat mass is as a free parameter.

Previous Accelerator Searches for the Magnetic Monopole The first accelerator based search for magnetic monopoles took place at Lawrence Berkeley Laboratory [28] and used emulsions as the sensitive medium. Since then there have been ∼ 31 accelerator searches for magnetic monopoles using a variety of detectors. Monopole search have been performed at practically all accelerator facilities with the required energy to perform a useful search. Thus, monopole searches have been performed at each new energy frontier. It is interesting to note that of the ∼ 31 searches performed to date almost half (14) have utilized NTDs. Existing direct and indirect search limits are summarized in Figure 2 and in Figure:11.

Magnetic Monopole Pair Production Cross-section at the LHC Due to the high coupling constant of the magnetic monopole perturbative calculations of the magnetic monopole cross section cannot be made. Instead a Drell-Yan mechanism [29] is assumed for the cross section calculation. Figure 3 shows a Feynman diagram of the Drell-Yan mechanism for dimuons and monopole-antimonopole production. These two diagrams shows annihilation of the quark-antiquark via the intermediate virtual photon and later photon decay into the two leptons (left) and monopole-antimonopole pair (right).

This simple production mechanism allows qualitative cross section estimates in the absence a reasonable field formulation of monopole production. The Drell-Yan cross section depends on the strong interaction between the initial pair of quarks. In the high energy limit, the quarks are treated like free charged particles and their interaction is purely electromagnetic. This is a good approximation for reasonably high energies ($E \gg \mathrm{m}_q$), where E is the total energy of the incident particles in the centre-of-mass system. The cross-section $\sigma(qq \rightarrow l^+l^-)$ is related to $\sigma(e^+e^- \rightarrow \mu^+\mu^-)$, which is given by: $\sigma(e^+e^- \rightarrow \mu^+\mu^-) = 4\pi\alpha^2/3E^2_{cm}$, (for $E \gg m_\mu$. The electron charge e is replaced by the quark charge $Q|e|$ and all possible colour orientations of the quark are averaged,

$$\sigma(qq \rightarrow l^+l^-) = \frac{Q^2}{3} \times \frac{4\pi\alpha^2}{3E^2_{cm}} \tag{3}$$

The complete cross-section takes into account the quark structure of the hadrons.

We can use this formulation to attempt to calculate the production cross-section for magnetic monopoles once the proper coupling of the magnetic charge to the electromagnetic field is incorporated. This is derived by combining the Dirac quantization condition with the definition of the coupling constant $\alpha_{mm} = \alpha(ng_D/e)$ ($\alpha \sim e^2$), which gives the cross-section:

$$\sigma(qq \rightarrow m\bar{m} = (\frac{ng_D}{e})^2 \times \sigma(qq \rightarrow l^+l^-) \tag{4}$$

Accele-Rator	Reaction	Beam Energy Gev	√s GeV	Mass limit GeV	Cross Section cm^2	MM Charge	TECN	Year
LBL	pA	6.2	3.76	<1	1.e-40	1	EMUL	1959
CERN	pA	28.0	7.6	<3	1.e-35	<4	CNTR	1961
AGS	pA	30.0	7.86	<3	2.e-40	<2	CNTR	1963
CERN	pA	28.0	7.6	<3	1.e-40	<2	EMUL	1963
IHEP	pA	70.0	11.9	<5	1.e-41		EMUL	1972
FNAL	pA	400	28.3	<13	5.e-42	<24	CNTR	1974
ISR	pp	60	60	<30	1.e-36	<3	PLAS	1975
FNAL	pA	400	28.3	<12	5.e-43	<10	INDU	1975
FNAL	pA	300	24.5		2.e-30		OSPK	1975
IHEP	pA	70	11.9	<5	1.e-40	<2	CNTR	1976
CERN	pp	56	56	<30	1.e-37	<3	PLAS	1978
CERN	pp	63	63	<20	1.e-37	<24	CNTR	1978
SLAC	e+e-	29	29	<30	4.e-38	<3	PLAS	1982
CERN	pp	52	52	<20	8.e-36		CNTR	1982
CERN	e+e-	34	34	10	4.e-38	<6	PLAS	1983
CERN	pp	540	540		1.e-31	1,3	PLAS	1983
SLAC	e+e-	29	29		3.e-38	<3	PLAS	1984
FNAL	pap	1800	1800	<800	3.e-38	>=1	PLAS	1987
CLEO	e+e-	10.6	10.6	<4	9.e-37	<0.15	CLEO	1987
CERN	e+e-	50-52	50-52	<24	8.e-37	1	PLAS	1988
DESY	e+e-	35	35	<17	1.e-38	<1	CNTR	1988
KEK	e+e-	50-61	50-61	<29	1.e-37	1	PLAS	1989
FNAL	pp	1800	1800	<850	2.e-34	>=0.5	PLAS	1990
CERN	e+e-	88-94	88-94	<45	3.e-37	1	PLAS	1992
CERN	e+e-	88-94	88-94				PLAS	1993
CERN	PbA	160A	17.9	<8.1	1.9e-33	>=2	PLAS	1997
AGS	AuAu	11A	4.87	<3.3	0.65e-33	>=2	PLAS	1997
FNAL	pap	1800	1800	260-420	7.8e-36	2-6	INDU	2000
FNAL	pap	1800	1800	265-410	0.2e-36	1-6	INDU	2004
HERA	e+p	300	300		0.5e-37	1-6	INDU	2005
FNAL	pap	1800	1800	369	0.2e-36	>=1	CNTR	2006

Figure 2: Compilation of the accelerator based experiments derived from Particle Data Group [30]. Experiments that utilized NTDs are high-lighted.

Thus, to get the monopole-pair cross-section the Drell-Yan cross-sections are scaled by a factor $(ng_D/e)^2$.

For pp collisions there exists data on the differential cross-section for production of massive virtual photons, which exhibits scaling and falls of exponentially with $x \equiv 2M_m/\sqrt{s}$, [31] where $\sqrt{s}$ is the available centre-of-mass energy and M_m is the magnetic monopole mass [3]. To this end we have predicted monopole-pair cross-sections at LHC energies by the formula:

$$\frac{d\sigma}{dmdy}|_{y=0} = \frac{44 \times 10^{-30}}{s^{\frac{3}{2}}} \times e^{\frac{-25.3m}{\sqrt{s}}} cm^2/(GeV/c^2) \tag{5}$$

To obtain the cross-section for monopole pair production with mass $M = (s/2)^{1/2}$ we integrate the cross-section above $m = 2M_m$. Assuming no phase space suppression:

$$\sigma_M = (68.5)^2 \times \frac{1.74}{s} \times e^{\frac{-25.3m}{\sqrt{s}}} \times 10^{-30} \tag{6}$$

Running for one year (10^7 s) at a luminosity of 5×10^{32} cm^{-2}s^{-1} the search sensitivity, when convoluted with the MoEDAL acceptance and detection efficiency, is shown in Figure 11.

The cross-section given above is intended to be a rough point of reference cross-section for the production of magnetic monopoles via the electromagnetic interaction. This estimate is conservative since higher order diagrams with more than one virtual photon in the intermediate state will also contribute. Production via gluon-gluon fusion may be more likely

[3]For pp collisions this cross-section is about an order of magnitude smaller than for $p\bar{p}$ collisions at the same centre-of-mass energy [32]

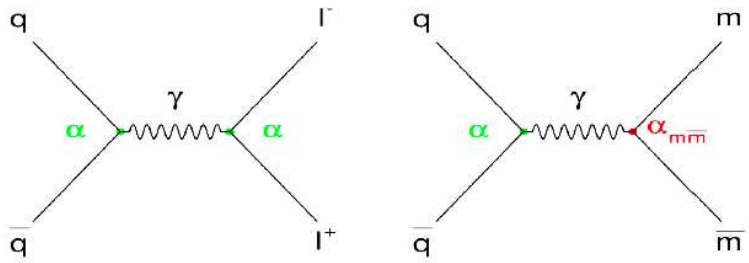

Figure 3: Drell-Yan process for dimuon production (left) and monopole-pair production (right).

still [33]. The variation of the predicted Drell-Yan cross-section with magnetic monopole mass is shown in Figure 4. We find excellent agreement with the Drell-Yan curve for the mass interval 200-600 GeV/c^2 published by the authors of the CDF experiment [34], as is shown by the orange curve which fits the black predicted curve well.

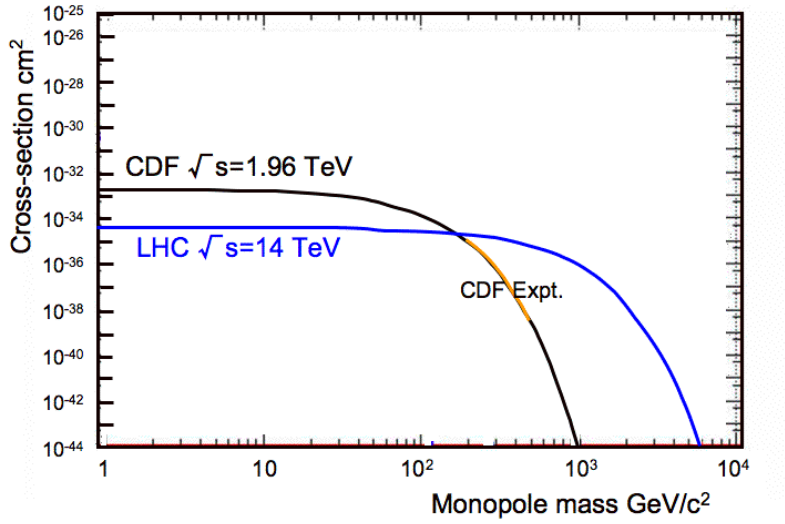

Figure 4: The Drell-Yan cross-section versus magnetic monopole mass for the Tevatron and LHC Energies.

1.1.2 SMPs with Single Electrical Charge

Among the most interesting and comprehensively studied possibilities for observable new physics is supersymmetry (SUSY) for comprehensive reviews see, e.g. [35]. At the most general level we have the minimal supersymmetric Standard Model (MSSM) that incorporates "soft" SUSY-breaking interactions which are consistent with gauge and Poincaré invariance, and solve the hierarchy problem. The general MSSM allows for a number of sparticle SMP candidates. In models with neutralino dark matter, the NLSP can be long-lived if its decay phase space is small or zero, mimicking the case of the neutron in the SM. In the MSSM the *stop*, the *stau*, the *chargino*, and the *gluino* can be SMPs.

When gravity is included, as in supergravity models, the gravitino can be the LSP, depending on its mass. If the gravitino is light, the NLSP will then often be long-lived due to

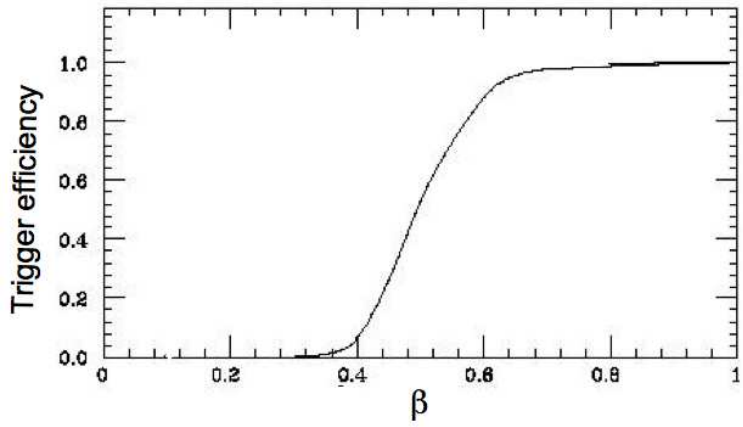

Figure 5: Estimate of the (muon) trigger efficiency (normalized to the efficiency of an ultra-relativistic muon) as a function of the values of an SMP particle escaping the central calorimeter.

the smallness of the gravitational coupling. For supergravity models with a long-lived *stau* NLSP see [36]. In models with gauge mediation such as GMSB [37], the gravitino is very light (< 1 keV) and hence the LSP for any relevant choice of parameters. A long-lived *stau* is not the only SMP possibility in GMSB. If the mixing and consequently the mass splitting in the *stau* sector is not too large (small $\tan\beta \lesssim 8$ [38]), then the *selectron* and the *smu* may be nearly mass-degenerate (co-NLSP) with the *stau* and hence can simultaneously be SMPs. There is also a very large space of possible non-minimal models, cf. [39]. Of particular interest here are SUSY GUT extensions of GMSB in which the coloured messengers are naturally much heavier than their weak counterparts, resulting in a gluino NLSP/LSP [40], depending on the gravitino mass.

Meta-stable coloured sparticles can arise in the so-called split SUSY scenario [41], in which all the scalars (except the ordinary Higgs) have very large masses, while the gaugino and higgsino masses remain at or around the weak scale. This naturally suppresses both proton decay and CP and flavour violation, although the hierarchy problem is not addressed (except anthropically), Since gluinos can only decay via squarks (independently of whether R-parity is conserved or not), the gluino lifetime can be very large in this scenario, like the muon in the Standard Model. in thiscase gluinos are the long lived particle and they show up in hadronized states called"R-Hadrons" [42].

Anomaly mediated SUSY-breaking (AMSB) [43] is a variant of supergravity, where the explicit SUSY-breaking terms are at least heavily suppressed, leaving a scaling (conformal) anomaly in the supergravity Lagrangian as the sole source of supersymmetry breaking. In a part of the parameter space, the *neutralino* is the LSP, and hence the chargino can be long-lived. In other regions the *stau* can be the LSP. For an LHC phenomenology study, see [44]. In gaugino-mediated SUSY-breaking (gMSB) [45], the MSSM is embedded in a 5-dimensional compactified braneworld setup. The only non-vanishing soft SUSY breaking terms at the compactification scale, M_c, are the gaugino masses. In the original models, $M_c = M_{GUT}$, which gives a *stau* LSP. The *smuon* and *selectron* are typically slightly heavier, due to the smaller mixing in the first two generations, but they can also be SMP candidates.

In models of Universal Extra Dimensions (UED) all the fields of the SM, including both matter and forces, are allowed to propagate in some number of extra dimensions, usually taken to be one or two. In the simplest models, all the KK modes of the light SM particles

(the photon, gluon, and first generation fermions) may be sufficiently long-lived to also be SMP candidates. Finally, we note that a GMSB-like phenomenology with a stable KK graviton and a meta-stable next-to-lightest KK particle, e.g. has also been discussed [46] More exotic possibilities for supersymmetric SMP candidates also exist, in particular in models where the MSSM gauge groups and particle content are extended to include more superfields. A recent example is a variant of the so-called Fat Higgs model, based on the MSSM with an extra confining SU(3) symmetry, the Fat Higgs with a Fat Top [47]. In this model, quasi-stable exotic chiral superfields (i.e. a complex scalar and a fermion) appear, which are charged under a global symmetry, which makes them approximately stable. The strongly interacting ones are probably outside the range of colliders, but there is a weak-scale electrically charged multiplet whose members have SMP properties [47].

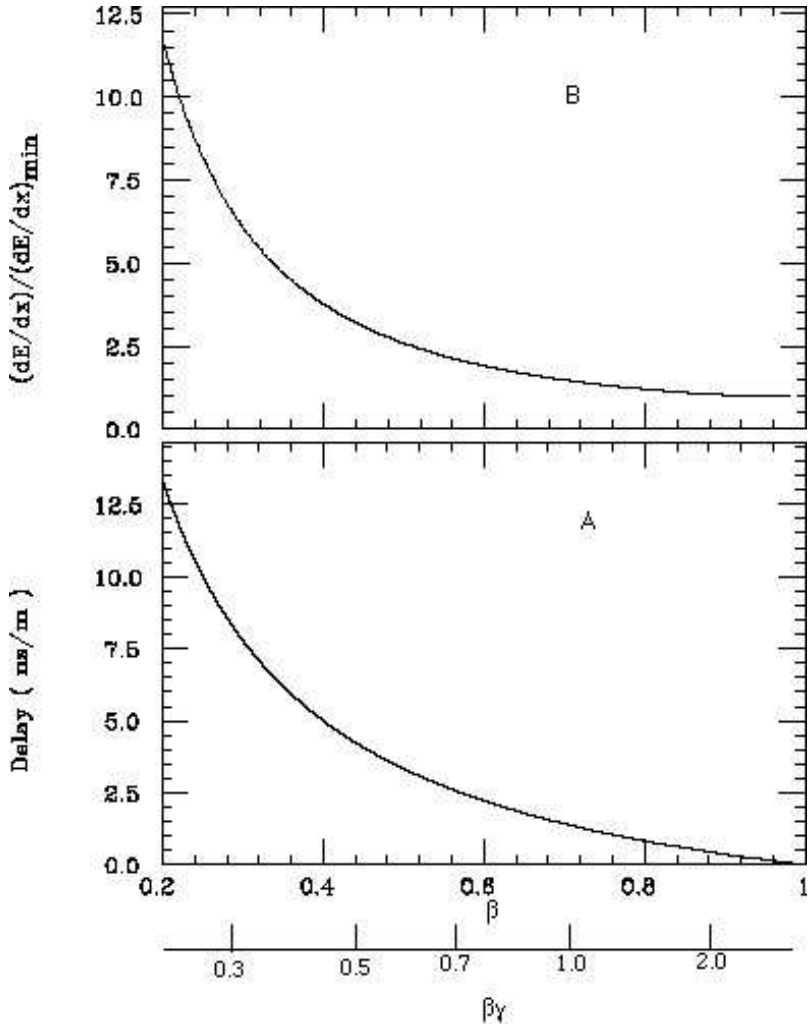

Figure 6: A) Delay per meter of a particle as a function of β; B) Energy loss rate normalized to the value at the minimum as a function of β. The scale in $\beta\gamma = \beta/\sqrt{(1-\beta^2)}$ s also shown.

In warped extra dimensions with GUT parity [48][49], the combination of extra dimensions and an effective TeV scale supersymmetric grand unification results in KK towers not only of the SM gauge and Higgs fields, but also of their SUSY-GUT partners, including XY bosons and coloured Higgs multiplets. A parity can be chosen such that the MSSM particles are even and their GUT partners odd, hence the lightest GUT-odd particle (LGP) is stable or long-lived. In the earliest model [48], the LGP is typically a light isospin-up (-down) colour triplet XY gaugino, with electric charge -1/3 (-4/3), but in the more recent models [49] a wider range of possibilities are open. In a more recent five dimensional model [50]

of dynamical SUSY-breaking (DSB), TeV scale exotic scalars with the quantum numbers of GUT XY bosons appear, so-called xyons. If a condition similar to R-parity holds in the DSB sector, these states are also long-lived. Their precise quantum numbers depend on the details of the DSB in general they are both coloured and charged. In the simplest SU(5) case they lie in a colour triplet isospin doublet with electric charges Q = $\pm 1/3, \pm 4/3$.

Finally, there also exist a few more general ideas for possible (quasi-)stable BSM particles, including long-lived leptoquarks (see, e.g. [51]) and additional (generations of) fermions [52]. The latter can either be straightforward additions to the SM generations, e.g. a 4th generation with 4th flavour approximately conserved [53] , or they can have a non-SM like structure. Mirror fermions (see, e.g. [54]) are extra fermions whose right-chiral members lie in SU(2) doublets while the left-handed ones are singlets, i.e. opposite to the SM. A vector-like generation is comprised of an extra SM generation together with its mirror, as e.g. in N = 2 supersymmetric models [55]. Another example of a SMP is given by heavy quarks belonging to higher representations of SU(3_C) [56]. A color sextet of quarks Q has been proposed in order to explain the dynamical breaking of the electroweak symmetry [57]. The quark sextet, taking the role of a condensate, forms a doublet of weak SU(2)L (U D). The lightest state of these quarks may be stable or it may decay into normal quark and long-lived leptons after being hadronized in an exotic colorless hadron.

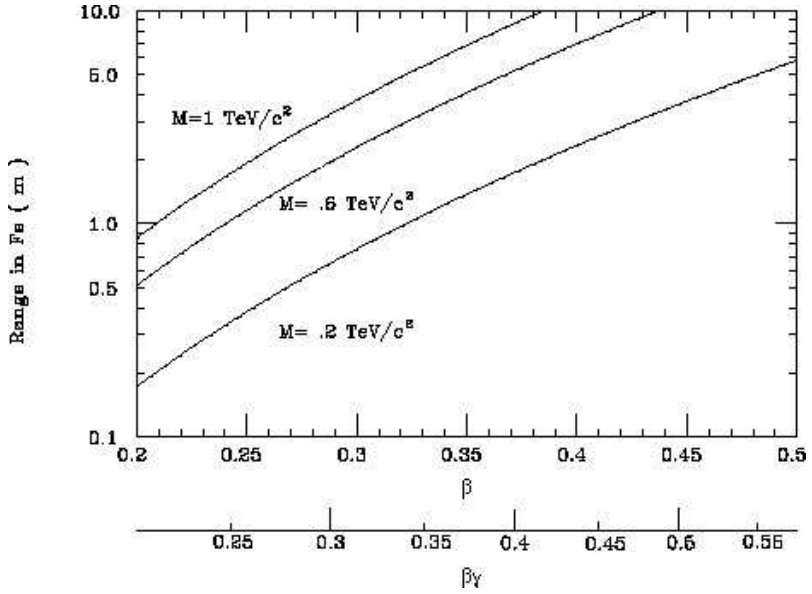

Figure 7: The range of a SMP in iron as a function of three different mass values. Note that the ATLAS central calorimeter corresponds to about 2m of iron The scale in $\beta\gamma$ is also shown.

Generic SMPs which possess electric charge and penetrate through the ATLAS or CMS detector will leave a clear signature of a high-p_T, slow, muon-like track. The background is expected to be highly suppressed by use of the time of flight technique [58]. Thus, penetrating SMPs with appropriate production cross sections would, in principle, be observed. However, as mentioned above, for an SMP at the LHC to be detected or triggered in a certain detector system and be associated to the correct bunch crossing, it should arrive at most 25 ns after the default arrival time of a particle traveling at the speed of light. Later arrival would imply triggering or detection within a subsequent crossing time window. This would complicate detection.

For SMPs which stop in the calorimeter and do not traverse the muon system, searches could rely on observing an excess of high-p_T tracks in the inner detectors. In conjunction with this, observables such as a charged particle leaving a signature of anomalous ionization in the

tracking chambers together with a characteristic energy deposition profile in the calorimeters could also be used. However, highly ionizing SMPs can be absorbed before they penetrate ATLAS or CMS. Also, as described earlier the precision with which ionisation energy loss can be measured in the general purpose LHC detectors is not clear.

An example of a study of the possible detection of SMPs at the LHC is given in Ref. [59]. It assumes a proposed ATLAS high luminosity trigger ($\sim 10^{34}\mathrm{cm}^{-2}\mathrm{s}^{-1}$) and high p_T ($\geq$ 20 GeV/c) muons in which all the three stations of the ATLAS RPC are in coincidence. Figure 5 shows the trigger efficiency they obtained. The efficiency drops rapidly from 50% at a $\beta = 0.5$ to zero at $\beta \sim 0.35$. In Figure 6(a) the the delay (ns/m) of the SMP particle with respect to an ultra-relativistic particle as a function of β and $\beta\gamma$ is reported. As the outermost muon chambers extend to radius of $\sim$ 10m in ATLAS, we can see that the SMP does not reach them during a single beam crossing period of 25ns. In Figure 6(b) the corresponding energy loss rate normalized to its minimum value is shown. As can be seen an SMP would be detectable with nuclear track detectors with a Z/β threshold of 5 at a $\beta \sim 0.4$. The rapid increase of the energy loss with decreasing values means that the SMP particle may stop inside the hadronic calorimeter.

In Figure 7 the range of an SMP particle in iron is given as a function of β, for a mass of 0.2, 0.6 and 1 TeV/c^2. Considering that the inner ATLAS calorimeter system corresponds to about 2 m of iron, we see that only SMP particles with masses M $\geq$ 1 TeV/c^2 could escape the calorimeter when $\beta \leq 0.25$. An SMP particle stopped inside the calorimeter is typically lost because the kinetic energy deposited into the calorimeter is, in almost every case, below the threshold of the hadron calorimeter trigger.

The MoEDAL experiment would be able to complement the above search strategies by allowing searches for electrically charged SMPs with Z/$\beta > 5$, with a maximum around 200e $\rightarrow$ 300e. The upper limit on the SMP Z/β to which ATLAS and CMS will be sensitive is still unclear. However, it is likely to be substantially below the reach of MoEDAL.

1.1.3 SMPs with Multiple Electrical Charge

A number of models for physics beyond the Standard Model hypothesize the existence of multiply charged SMPs. Candidates include, for example, the doubly charged Higgs boson of Left-Right Symmetric Models [60] and its corresponding SUSY particle, the doubly charged Higgsino [61]. Another example of a multiply charge particle is the Bilepton which appears in models where SU(2)L gauge group is extended to SU(3) [62] and also in models with extended Higgs sectors that contain doubly charged Higgs bosons [63]. Grand unified theories, technicolor and composite models predict the existence of bileptons as well as other exotic particles [64]. A comprehensive review of bilepton phenomenonology has been presented in [65] including low and high energy bounds on their couplings.

The prospect of microscopic black hole production at the LHC has been discussed within the framework of models with large extra dimensions [66]. More recently, the prospect that such black holes could yield stable remnants, rather than evaporating completely via Hawking Radiation, has been discussed [67]. In the scenarios discussed, the black hole remnant can acquire a multiple electrical charge. The multiple charge of these multiply charged SMPs, combined with their potentially low β make them good candidates for detection by the NTD array forming the MoEDAL detector.

Black hole remnants Models with large extra dimensions (LXDs) are motivated by string theory [68] and provide us with an effective description of physics beyond the standard model (SM) in which observables can be computed and predictions can be made. Arkani-Hamed, Dimopoulos and Dvali [66] proposed a solution to the hierarchy problem by the

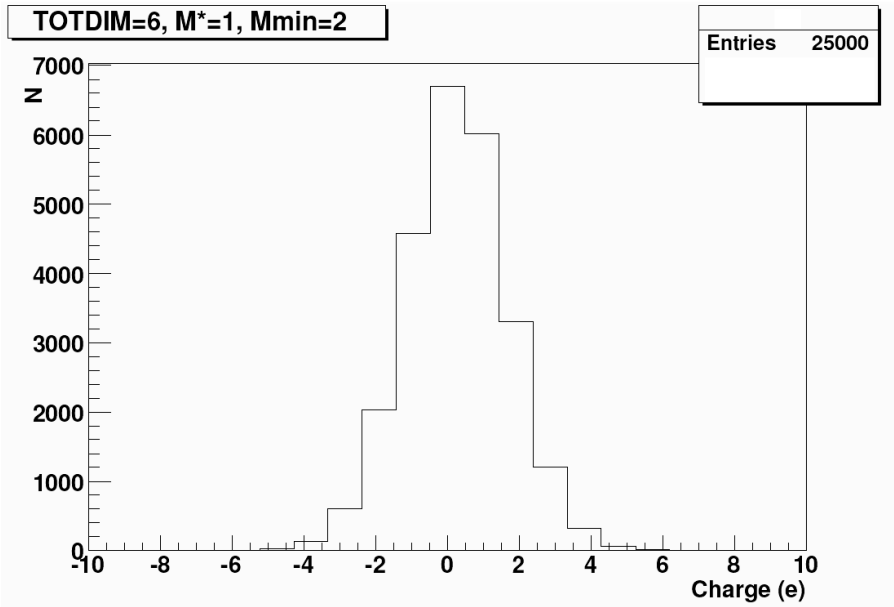

Figure 8: Charge distribution of black hole remnant charges in p-p interactions at $\sqrt{s} = 14$ TeV calculated with the PYTHIA event generator and the CHARYBDIS program

introduction of d additional compactified space-like dimensions in which only the gravitons can propagate. The SM particles are bound to our 4-dimensional sub-manifold, often called our 3-brane. The volume of the extra dimensions suppresses the fundamental scale and thus, can explain the huge value of the observed Planck mass $m_p \sim 10^{16}$ TeV. The radius R of these extra dimensions, for $M_f \approx$ TeV, can be estimated with Eq.(3) and typically lies in the range from 10^{-1} mm to 10^3 fm for d from 2 to 7, or the inverse radius $1/R$ lies in energy range eV to MeV, respectively.

To compute the production details, the cross-section of the black holes can be approximated by the classical geometric cross-section: $\sigma(BH) \approx \pi R_H^2$, where R_H is the horizon radius of the black hole. This expression contains only the fundamental Planck scale as coupling constant. This cross section is a subject of ongoing research [69] but close investigations justify the use of the classical limit at least up to energies of $\sim 10 M_f$ [70]. It has further been shown that the naively expected classical result remains valid also in string theory [71].

An exciting possibility at the LHC is the production of TeV mass black holes made possible by the existence of Large Extra Dimensions (LEDs) that lower the Planck scale to values accessible at the LHC. However, the final phases of black hole evaporation are still unknown and there is a well theoretically well motivated possibility that a black hole remnant would remain after the decay of the microscopic black hole. The final fate of these evaporating black holes is closely connected to the information loss puzzle. When one tries to avoid the information loss problem two possibilities are left. The information is regained by some unknown mechanism or a stable black hole remnant is formed which keeps the information. Besides the fact that it is unclear in which way the information should escape the horizon [72] there are several other arguments for black hole remnants [73].

The black hole produced in a proton-proton collision can carry an electric charge. The evaporation spectrum contains all particles of the SM and so, a certain fraction of the final black hole remnants will also carry net electric charge. In the following, these charged black hole remnants will be denoted BH^+ and BH^-, and the neutral ones BH0, respectively. Since the $BH^{\pm}$s undergo an electromagnetic interaction, their cross section is enhanced and

they can be examined closely. This makes them extremely interesting candidates for the investigation of Planck scale physics.

Black holes are typically formed from the interaction of valence quarks as those carry the largest available momenta of the partonic system. So, the black holes formed in a proton-proton collision will have an average charge of ∼4/3. The black holes decay with an average multiplicity of ≈ 10-25 into Standard Model particles, most of which will be charged. The details of the multiplicity depend on the number of extra dimensions [67] After the black holes have evaporated off enough energy to be stable at the remnant mass, some have accumulated a net electric charge. According to purely statistical considerations, the probability for being left with highly charged black hole remnants drops fast with deviation from the average. The largest fraction of the black holes should have charges ± 1 or zero, a smaller but non-negligible fraction would be multiply charged.

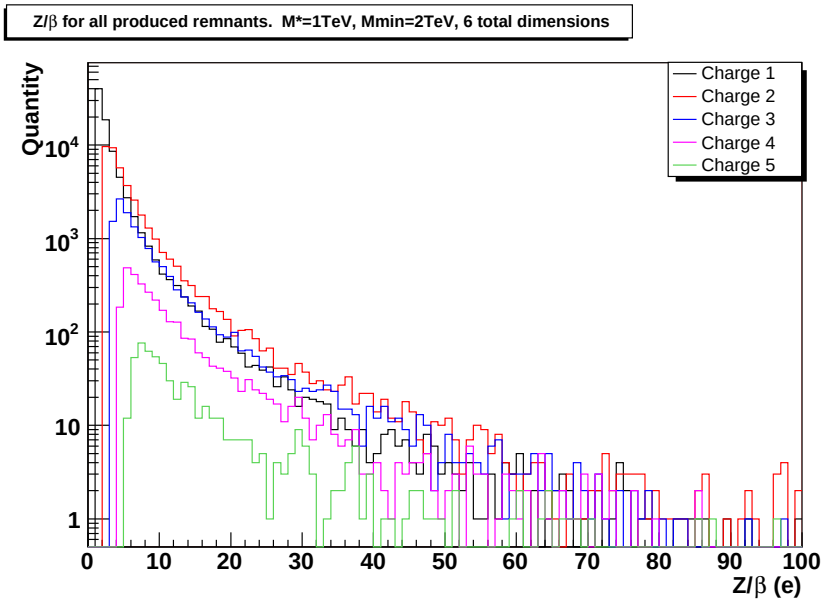

Figure 9: Z/β (β =v/c) distribution for black hole remnant charges in p-p interactions at $\sqrt{s} = 14$ TeV calculated with the PYTHIA event generator and the CHARYBDIS program.

We have estimated the fraction of charged black hole remnants with the PYTHIA event generator and the CHARYBDIS program [74] with the final decay of the black hole and the charge minimization. Figure 1 shows the results for a simulation of proton-proton collisions at the LHC with an estimated center of mass energy of s = 14 TeV. We further assumed as an applicable model, described in Ref. [67], that the effective temperature of the black hole drops towards zero for a finite remnant mass M_R. This mass of the remnant is a few time M_f and a parameter of the model. Even though the temperature-mass relation is not clear from the present status of theoretical examinations, such a drop of the temperature can be implemented into the simulation. It is interesting to note that the details of the modified temperature as well as the value of M_R do not noticeably affect the here investigated charge distribution as it results from the very general statistical distribution of the charge of the emitted particles.

Therefore, independent of the underlying quantum gravitational assumption leading to the remnant formation, we find that about 27.5% of the remnants carry zero electric charge, whereas we have 17.7% of BH^- and 23.5% of $BH^{+\cdot}$ The remaining 31.3% of remnants are multiply charged. The distribution of the remnants charge, generated using CHARYBDIS program, is shown in Figure 8. The black hole remnants considered here are heavy, with masses of a TeV or more. Thus, a more telling measure of their ionizing power is Z/β,

where Z is their electric charge and β is their velocity as a fraction of the speed of light. A standard minimum ionizing particle produced in LHC interaction would have a Z/β of one. The distribution of Z/β for black hole remnants of various charge, is shown in Figure 9.

Doubly-Charged Higgs One major puzzle of the Standard Model is the fact that weak interaction couplings are strictly left-handed. In order to remedy this apparent arbitrariness of nature, one must extend the gauge group of the Standard Model to include a right-handed sector. The simplest realization is a Left-Right Symmetric Model (LRSM) [60] that postulates a right-handed version of the weak interaction, whose gauge symmetry is spontaneously broken at high mass scale, leading to the parity violating SM. This model is supported by recent data on neutrino oscillations [75] and explains small neutrino masses [76]. The model generally requires a Higgs triplet containing a doubly charged Higgs boson.

Single production of a doubly charged Higgs boson at the LHC is possible via vector boson fusion, or via the fusion of a singly-charged Higgs boson with either a W or another singly charged Higgs boson. The amplitudes of the $W_L W_L$ and $W_R W_R$ vector boson fusion processes are proportional to $v_{L,R}$, the vacuum expectation values of the neutral members of the scalar triplets of the LRSM . For the case of Δ_R^{++} production, the vector fusion process dominates. For the production WW $\rightarrow \Delta_L^{++}$, the suppression due to the small value of the v_L is somewhat compensated by the fact that the incoming quarks radiate a lower mass vector gauge boson.

Pair production of the doubly charged Higgs is also possible via a Drell-Yan process, with γ, Z or Z_R exchanged in the s-channel, but at a high kinematic price since substantial energy is required to produce two heavy particles. In the case of Δ_L^{++}, double production may nevertheless be the only possibility if v_L is very small or vanishing.

The decay of a doubly charged Higgs can proceed by several channels. Dilepton decay provides a clean signature, kinematically enhanced, but the branching ratios depend on the unknown Yukawa couplings. Present bounds [77] on the diagonal couplings $h_{ee,\mu\mu,\tau\tau}$ to charged leptons are consistent with values O(1) if the mass scale of the triplet is large. For the Δ_L^{++}, this may be the dominant mode if v_L is very small. One would then have the golden signature $q\bar{q} \rightarrow \gamma^*/Z^*/Z'^* \rightarrow \Delta_L^{++}\Delta_L^{--} \rightarrow 4l$.

For very small Yukawa couplings ($H_{ll} \lesssim 10^{-8}$) the doubly charged Higgs boson could be quasi-stable. In this case very slow pseudo-stable Higgs could be detected in the MoEDAL NTDs. For example with CR39, one could detect doubly charged Higgs particles with a Z/β >5(15), where $\beta \lesssim 0.4(0.13)$. If such slow heavy particles are produced then one could have difficulty measuring them in ATLAS and CMS as their journey through the detector to the muon system would span more than one beam crossing.

1.2 Signal and backgrounds

There are a few kinds backgrounds capable of producing highly ionizing signals. An important background source to such studies is positively charged nuclei. These typically arise as spallation products from secondary interactions of particles produced in the primary interaction. Such interactions take place with nuclei in the material of the detector and the material surrounding and including the beampipe. Another background arises from interactions of the colliding beams with residual gas atoms in the beam pipe can also produce highly ionizing spallation products. However, the great majority of background events have low momentum [78].

The above sources of background are severely reduced in NTD arrays. First, the two track resolution of NTDs is extremely good, of the order of 10μms. Also, the threshold of CR39,

the most sensitive, of the NTDs employed by MoEDAL - corresponding to a Z/β as low of 5 - in conjunction with the requirement of aligned etch pits in a several NTD sheets, is enough to severely reduce the background from the above sources. In addition, Makrofol/Lexan have a factor of 100 smaller sensitivity to spallation background than CR39.

In the case of the magnetic monopole the energy loss falls with β, unlike a conventionally charged particle. The signature of a monopole in a MoEDAL NTD stack would consist of a chain of collinear etch-pit pairs in 9 successive sheets, with roughly constant, actually slowly decreasing, etch pit radius indicating the passage of a particle with ionization rate gradually decreasing as it (gradually) slows in the plastic stack. An electrically charged particle that could constitute a background would be near the end of the range and would be distinguished by a chain of etch pits increasing in size as the particle slowed. Our accuracy of better than $\sim 50\mu$m in alignment of adjacent sheets is more than sufficient to rule out strings of accidental coincidences of unrelated holes. Also, the detector stack positions will be surveyed in and it will be possible to point back a track - formed from collinear etch pits - back to the intersection point with an accuracy of 1 cm. Providing another source of background reduction. In practice, no candidate monopole track - that forms a well collimated colinear track that traverses all of the plastic sheets in the stack with the correct ionization signature - has been observed in any collider search using NTDs. This means that no background track that satisfies the search criteria has been observed.

A powerful feature of etchable track detectors is that their response depends only on the dose within $\sim 10^{-6}$ cm of a particle's trajectory and is independent of dose rate. They can collect tracks for the duration of a run, the only limitation being due to degradation of the molecular structure of the detector by the accumulated radiation damage. At a hadronic collider the most severe limitation is the accumulation of short-range tracks of highly ionizing recoil nuclei produced in hadronic interactions with carbon, oxygen, and heavier nuclei in the detectors. The mean length is ~ 10 μm, with an exponential tail extending, with low probability, to about the thickness of one plastic sheet. Calibrations performed in previous experiments [79] have shown that for CR39 the number of etch pits formed per hadron is $\sim 10^{-4}$ and the maximum tolerable number of detected etch pits per cm^2 is $\sim 10^8$. This corresponds to a dose limit of 2Mrad. At this limit the problem is not false signals but rather that the plastic is so damaged that it will not survive the etching process. For MAKROFOL/Lexan the number of etch pits formed per hadron is $\sim 4 \times 10^{-6}$ and the maximum tolerable number of detected etch pits per cm^2 is $\times 10^8$ [79] - corresponding to a dose limit of 200 Mrad. The radiation levels in the VELO cavern in the vicinity of the MoEDAL detector are discussed in Section 2.5, below.

These levels indicate that the yearly replacement rate for CR39 NTDs should be perfectly adequate to ensure that the damage to the plastic by spallation products to be well within acceptable limits. However, we plan to assess the radiation damage to the MoEDAL array with an initial deployment of ~ 1 m^2 of NTDs. In addition, we will continually monitor the radiation environment in the VELO cavern. Extrapolations show that background tracks, that satisfy the selection criteria for monopole candidates described above, are not expected to be observed by MoEDAL.

1.2.1 Physics Impact

The main motivation of the MoEDAL experiment is to search for the magnetic monopole or dyon. In order to illustrate physics impact of MoEDAL we briefly consider the detection limits for single and multiply charged magnetic monopoles in the MoEDAL experiment. Also, to indicate the physics range of MoEDAL, we consider the case of the charged black hole remnant. A study of the physics impact of the complete physics program, is underway [80]

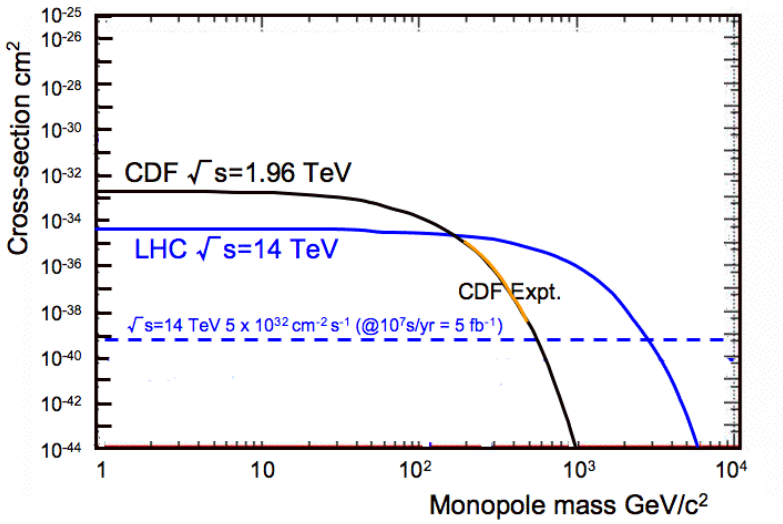

Figure 10: Drell-Yan cross-section curves for the LHC and the corresponding corresponding cross-section curves that would lead to the observation of one event in the MoEDAL detector after 5fb^{-1} and 10 fb^{-1} of luminosity.

Discovery limits for the magnetic monopole With normal LHC operation the maximum luminosity expected in LHCb and MoEDAL would be around 2 fb^{-1}/yr (2 x 10^{32} cm^{-2} s^{-1} for a year of 10^7 s). We plot in Figure 10 the Drell-Yan cross-section for magnetic monopole pair production at the LHC and for the Tevatron. The sensitivity of the MoEDAL experiment is given by plotting the cross-section for which there would be one event expected in the MoEDAL experiment. The MoEDAL sensitivity to magnetic monopole production for 5 fb^{-1} and 10 fb^{-1} is shown.

The last direct search for monopoles was undertaken at the Tevatron [34]. In this case members of the CDF collaboration searched for pair-produced Dirac magnetic monopoles in 35.7 pb^{-1} of proton-antiproton collisions at $\sqrt{s} = 1.96$ TeV. They found no monopole candidates allowing them to place a 95% confidence-level cross-section limit < 0.2 pb for a monopole with mass between 200 and 700 GeV/c^2. Assuming a Drell-Yan pair production mechanism, they set a mass limit $M_{mon.} > 360$ GeV/c^2. We can see from Figure 11 that the MoEDAL experiment should be able to push the search to much lower cross-sections and higher masses.

The overall acceptance for magnetic monopoles has been calculated assuming: production of monopole-pairs is isotropic in the centre-of-mass frame; and, that a magnetic monopole will be detected if its $Z/\beta >15$ when its crosses all 9 layers of plastic. Thus, the overall acceptance is a convolution of the geometric acceptance of the detector and the detection efficiency for Magnetic Monopoles. The geometric acceptance for the maximum possible deployment of plastic is 40%. The geometrical acceptance of the detector with the 1m diameter cut out in the detector acceptance, in the shielding wall deployed detectors around the beampipe region, is 32%. As can be seen from Figure 12 we still have acceptance for magnetic monopole charges higher as $3g_D$.

Implications for Cosmic Monopole Production It is interesting to ask how this new accelerator limit compares with the present limit on the flux of cosmic monopoles in the same mass range thermally produced in the early Universe. Starting with an assumed

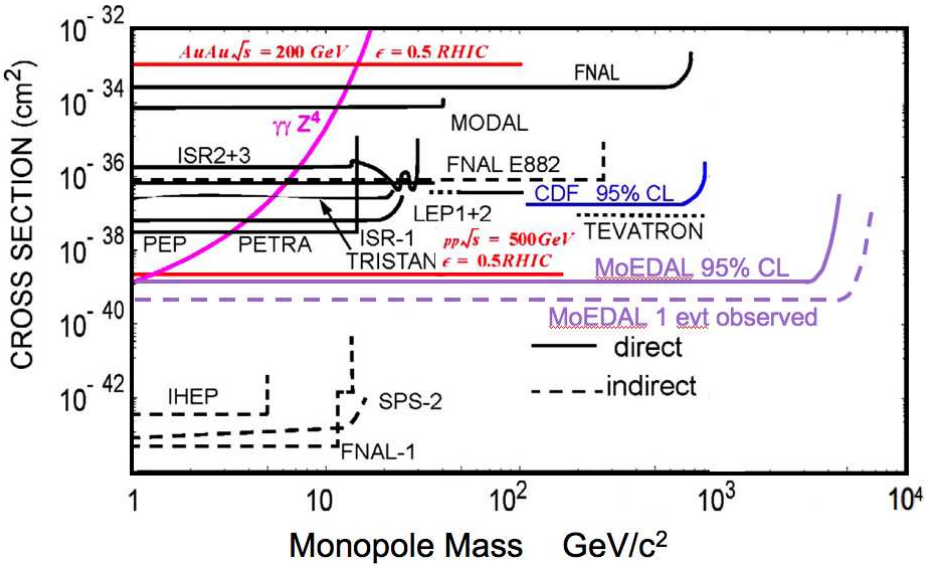

Figure 11: The plot shows: a) the 95% CL contour that would be obtained by MoEDAL with an efficiency x acceptance of 30% with an integrated luminosity of 10^{39} cm^{-2}s^{-1} and, b) the cross-section required to see one monopole event in MoEDAL as a function of monopole mass.

monopole- antimonopole annihilation cross section, an expanding universe, and detailed balance, Turner [81] estimated a lower bound on the present flux of thermally produced monopoles of mass M_m to be:

$$F_m = (10^{12} cm^{-2} sr^{-1} s^{-1}) \left(\frac{M_m}{T_1}\right)^3 e^{\frac{2M_m}{T_1}} \tag{7}$$

where T_1 is the temperature of the Universe when production commences. Usually T_1 is taken to be $\sim 10^{14}$ GeV. For a monopole mass of a few hundred GeV, the above estimate leads to a flux $F_m = 10^{-23} cm^2 sr^{-1} s^{-I}$, which is about a factor of 10^8 below the best limits to date [82]. Our search at the LHC collider places far stronger constraints on the existence of monopoles with mass of order hundreds of GeV than will be possible in the foreseeable future by searching for thermally produced cosmic monopoles.

Discovery limits for Black Hole remnants According to the scheme presented above microscopic black hole remnants with a $Z/\beta > 15$ will be detected by MoEDAL. In this case the remnants have a mass of 1 Tev and the number of extra dimensions is allowed to vary between 2 and 4 and the number of remnants detected per year varies between $\sim 10^3$ and $\sim 10^5$ for a luminosity of 10^{32} cm^{-2} s^{-1} This is assuming 10^7 s per year and an overall geometrical acceptance of $\sim 40\%$.

1.3 Physics and Detector Simulation

In this subsection we briefly discuss issues relating to the MoEDAL physics and detector simulation.

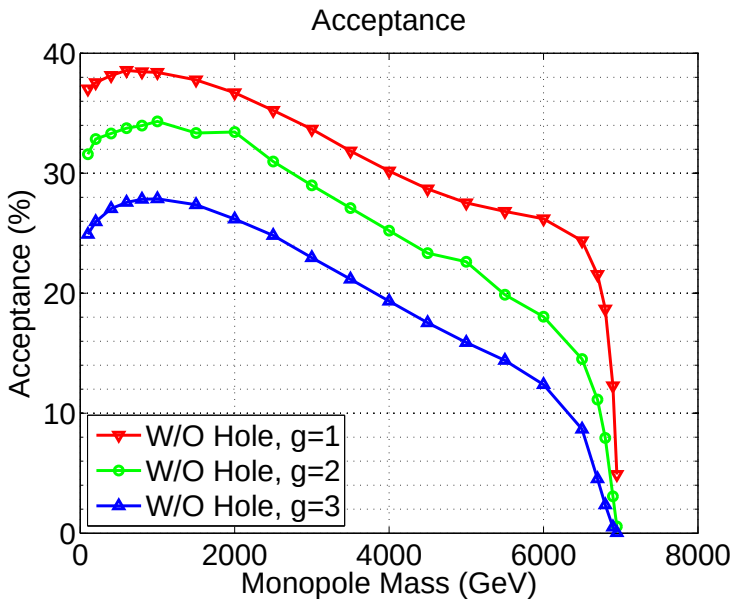

Figure 12: Acceptance × efficiency curves for MoEDAL for magnetic charges, g=1,2 and 3

1.3.1 Magnetic Monopole Simulation

The simulation of the passage of a magnetic monopole through LHCb and MoEDAL presented the greatest challenge since GEANT3/4 did not, at least until relatively recently, include tracking and energy loss code for magnetically charge particles. We have implemented an extension to GEANT4 that includes code to allow us to track a magnetic monopole. We based this work on an extension to the GEANT3 framework for monopole tracking that was provided by members of the CDF collaboration [83].

As can be seen from Figure 13 there is good agreement between the GEANT3 and GEANT4 version of the monopole tracking code and the result using the standard Bethe Bloch formula [84] for protons and for relativistic magnetic monopoles $\beta \gtrsim 1$, where the dE/dx for magnetic monopoles can be calculated by replacing ze by $ng_D\beta$ in the standard Bethe Bloch formula shown below:

$$-\frac{dE}{dx} = z^2 \frac{KZ}{A}\frac{1}{\beta^2}\left[\frac{1}{2}ln\left(\frac{2m_e\beta^2\gamma^2}{I^2}\right) - \beta^2\right] \tag{8}$$

where $K/A = 4\pi N_A r_e^2 m_e c^2/A$ =0.307 MeV/cm^2/g and I is the mean excitation energy of the scattering material, roughly $Z\times$10 eV. For $3\times10^{-4} \lesssim \beta' \lesssim 0.1$, the energy loss can be modeled by the equation:

$$\frac{dE}{dx} = K\beta \tag{9}$$

where, for example, $K = 33\text{n}^2$ GeV/cm for plastic and 124n^2 GeV/cm for iron.

Electromagnetic Duality implies a generalized Lorentz force law for particles carrying arbitrary electric charge e and magnetic charge g: $\overrightarrow{F} = e(\overrightarrow{E} + \overrightarrow{\beta} \times \overrightarrow{B}) + g(\overrightarrow{B} - \overrightarrow{\beta} \times \overrightarrow{E})$. Setting e and $\overrightarrow{E}$ to zero provides the differential equation describing the motion of a Dirac monopole in the magnetic field. This equation can be solved analytically for the case of a uniform field. The most distinctive features of magnetic monopole kinematics are that the trajectory does not curve in the plane perpendicular to the magnetic field, and the field does work on the monopole. A simulation of the trajectories of a monopole-pair, using a monopole mass of 100 GeV/c^2, produced at the LHCb intersection point is shown in Figure 14. In this simulation the monopole hit the MoEDAL detector wall and the antimonopole entered the acceptance of LHCb and hit the face of the LHCb dipole magnet.

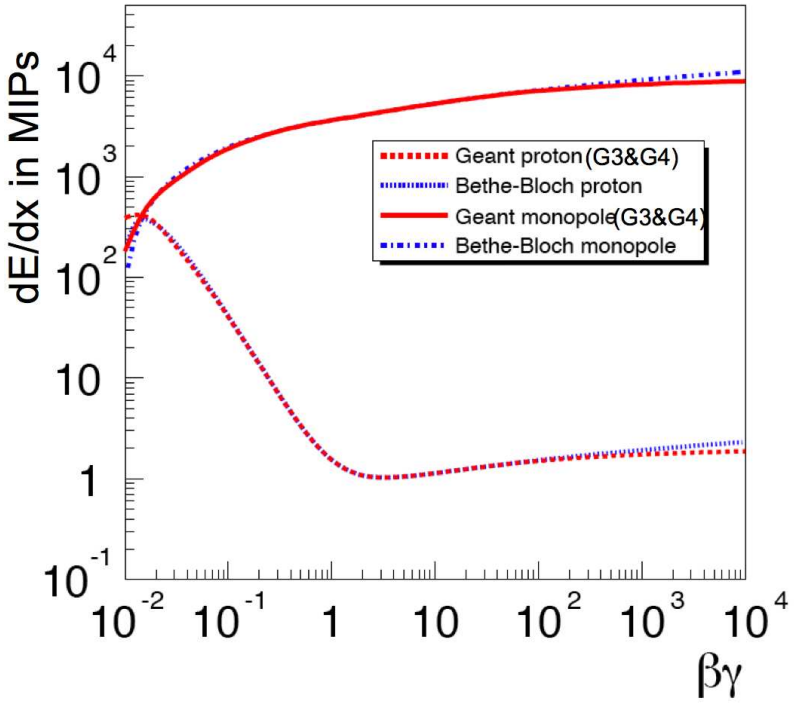

Figure 13: A comparison of the BetheBloch formula with GEANT 3 and 4 simulation for the energy loss of monopoles and protons in air.

1.3.2 Simulation of Microscopic Black Hole Remnant Production

For detailed studies of the experimental signatures of microscopic black hole production, PYTHIA 6.2 [85] was been coupled to CHARYBDIS [74] to create an event generator allowing for the simulation of black hole events and data reconstruction from the decay products. The modifications to the black hole evaporation arising from the presence of a remnant mass has been parameterized [86]. The modified spectral density is included in the numerical simulation for black hole events.

1.3.3 Detector Simulation

The MoEDAL simulation program is based on an extension Simulation to the LHCb simulation program GAUSS [87], which is in turn based on the Gaudi framework and on the LHCbSys classes . The Gauss simulation of the LHCb detectors allow understanding of its experimental conditions and its performance. It integrates two independent phases: a *Generator Phase* consisting of the generation of the p-p collisions and the decay of the particles produced; and, a *Simulation Phase* consisting in the tracking of the particles in the detector and simulating the physics processes occuring in the experimental setup. Gauss is interfaced to various specialized packages available in the Physics community for the Generator phase (e.g. EvtGen for b-decays) and makes use of the Geant4 toolkit for the Simulation phase. The version used for the simulations in this TDR is Gauss v33r2. The Geometry Version employed is *head* – 20080603. Figure 15 shows details of the material distribution in the LHCb VELO region as a function of radius from the IP, θ and ϕ.

Using the detector simulation described above the maximum practically achievable acceptance of the MoEDAL detector was determined to be 40%. Combining the detector simulation with the GEANT-4 model for monopole energy loss and trajectory curves of acceptance

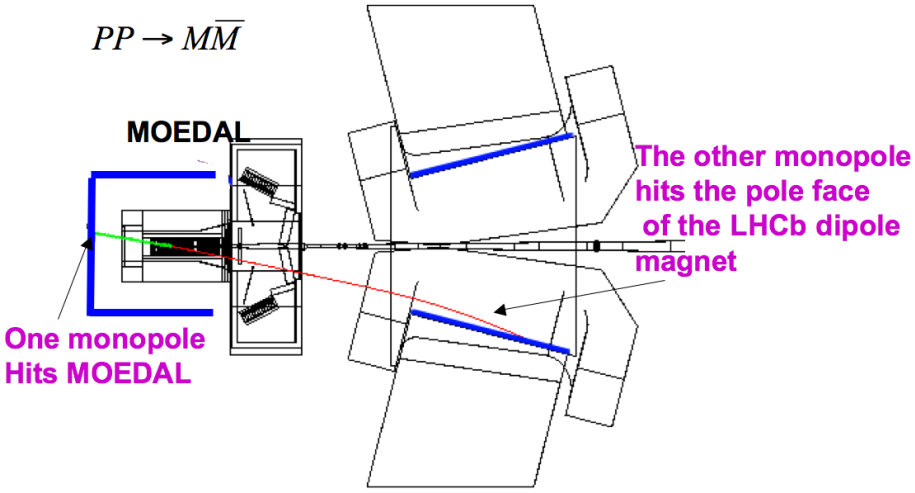

Figure 14: A GEANT4 based simulation of a $pp \rightarrow Monopole - Antimonopole$ production with monopole mass 100 GeV/c^2. The graphical output of the simnulation shows the monopole hitting the MoEDAL detector and the antimonopole entering the acceptance of the LHCb detectors, being accelerated along the field lines of the LHCb dipole magnet until it hits the pole face of the magnetic.

$\times$ efficiency were determined for magnetic charges, g=1,2 and 3. These curves are given in Figure 12.

1.4 Experimental Overview

The MoEDAL detector is comprised of an array of plastic Nuclear Track Detectors (NTDs) deployed around the (Point-8) intersection region of the LHCb detector, in the VELO (VErtex LOcator) cavern as shown in Figure 16. The array consists of NTD stacks, nine layers deep, in Aluminium housings attached to the walls and ceiling of the VELO cavern. The maximum possible surface area available for detectors is around 25 m^2, although the final deployed area could be somewhat less due to the developing requirements of the infrastructure of the LHCb detector. A 3-D schematic showing the maximum practicable deployment of plastic NTDs in the VELO cavern is given in Figure 17. A more detailed description of the MoEDAL detectors and the track-etch detector technology, can be found in Section 2. A full description of the etching and calibration procedures for MoEDAL track etch detectors is given in Section 3.

1.4.1 Track-Etch Detectors

When a charged particle crosses a plastic nuclear track detector it produces damages at the level of polymeric bounds in a small cylindrical region around its trajectory forming the so-called latent track as shown in Figure 18. The damage produced is dependent on the energy released inside the cylindrical region i.e. the Restricted Energy Loss (REL) which is a function of the charge Z and β = v/c (c the velocity of light in vacuum) of the incident highly ionizing particle (ion). When the velocity of the incident ion is $< 1\ 10^{-2}$ c the restricted energy loss is equal to the total energy loss of the particle in the medium; otherwise, only a fraction of the electronic energy loss leading to the formation of δ-rays with energies lower than a cut-off energy T_{cut} cut is efficient for the track formation. The REL can be computed from the Bethe-Block formula restricted to energy transfers T $<T_{cut}$

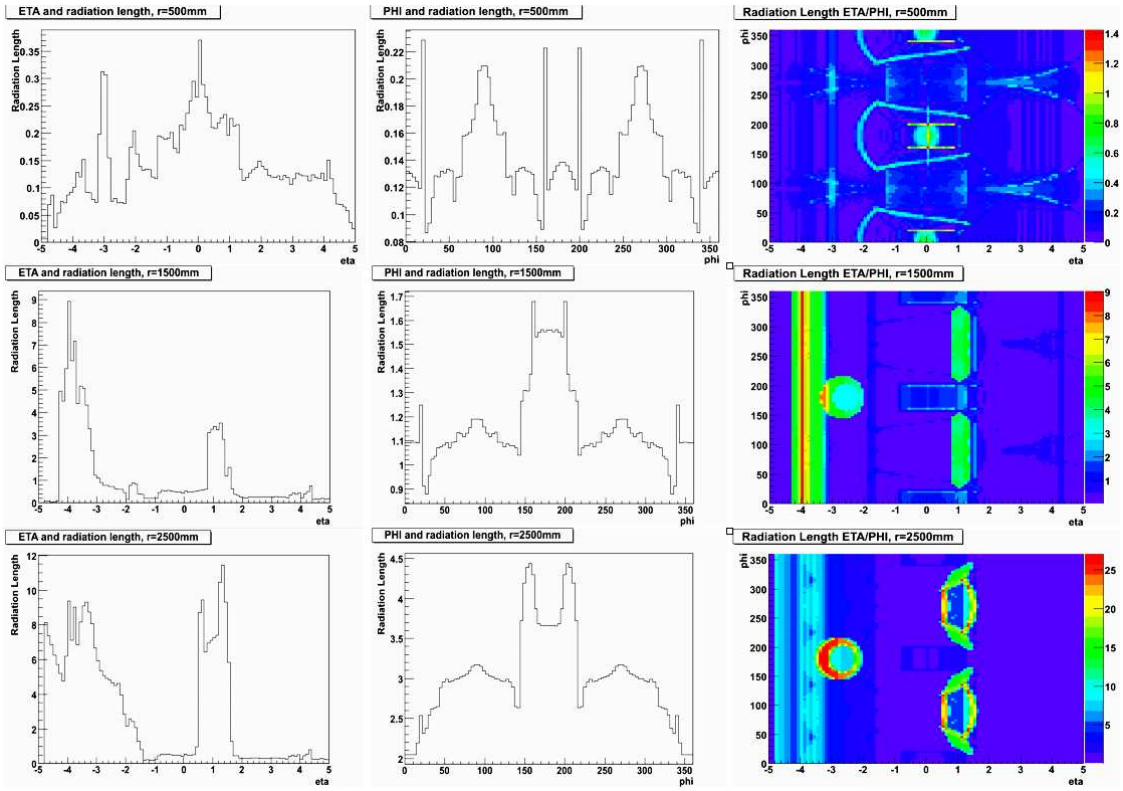

Figure 15: The depiction of the material budget in the LHCb intersection region up to radius of 0.5m, 1.5m and 2.5m, as measured from the LHCb IP.

with T_{cut} ($< T_{max}$) a constant characteristic of the medium and taking into account density and shell (charge screening) corrections. Figure 42 shows a sketch of the evolution of the etch-pit cones versus the etching time for a normally incident relativistic particle.

The subsequent etching of the solid nuclear detectors leads to the formation of etch-pit cones, as can be seen in Figure 42. These conical pits are usually of micrometer dimensions and can be observed with an optical microscope. Their size and shape yield information about charge, energy and direction of motion of the incident ion.

The latent track of a highly ionizing particle, such as a that of a magnetic monopole, is manifested by etching, where v_B is the bulk rate and v_T is the faster etch rate along the track. The damage zone is revealed as a cone shaped etch-pit, when the surface of the plastic detector is etched in a controlled manner using an etchant such as hot sodium hydroxide (NaOH) solution. In general the cone base has an elliptical form (circular if the impinging ion has a normal incidence angle). The response of the detector is given by the etching rate ratio $p = v_T/v_B$. From the measurements of the minor and major axes of the base of etch-pit cones it is possible to determine both p and the angle of incidence θ with respect to the detector surface:

$$p = \sqrt{1 + \frac{4A^2}{(1-B^2)^2}} \tag{10}$$

$$\theta = sin^{-1}\left(\frac{1}{p}\frac{1+B^2)}{1-B^2}\right) \tag{11}$$

where: $A = a/2v_B t_{etch}$ and $B = b/2v_B t_{etch}$, a/b are the major/ minor axes of the tracks and t_{etch} is the etching time. The bulk etching velocity can be determined from the measurement of the detector thickness at different times.

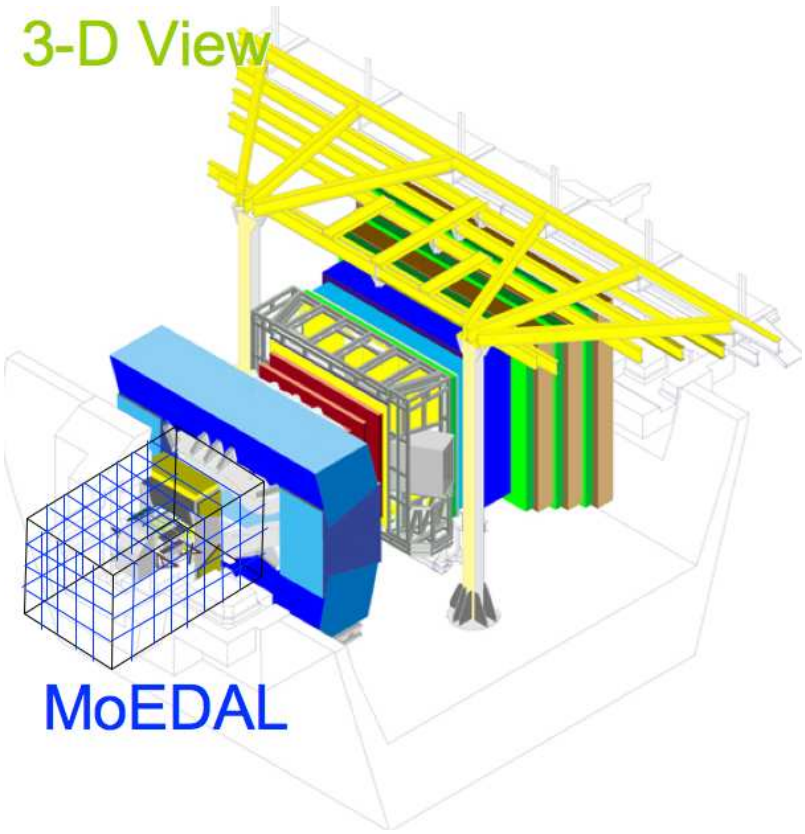

Figure 16: A 3-D schematic depiction of the deployment of the MoEDAL detector around the LHCb VELO region at Point 8. The area in which the MoEDAL detector is deployed is indicated by the red grid lines.

By exposing the detector to relativistic heavy ions of known energy and electric charge it is possible to obtain the calibration data expressed as the reduced etching rate $(p-1)$ versus REL. So, the charge of an incoming particle can be determined by the measured p of the corresponding tracks. Only particles releasing a REL above a threshold and incident within a definite angle (which depends on the particle energy loss) will be detected. Specific processing and etching conditions affect the detector threshold REL_{min}, or (Z/β)min that is the minimum charge and speed a particle must have to produce an etchable latent track.

Materials commonly used as solid state track etch detectors are polymers and polycarbonates such as polyallyl diglycol carbonate (PADC) also known as CR 39 with the chemical formula ($C_{12}H_{18}O_7n$) or Makrofol (Lexan) with the formula ($C_{16}H_{14}O_3n$). Details of the chemical structure and physical properties of these plastic NTDs are given in Appendix B.

The basic detector unit of the MoEDAL experiment is a stack of nine sheets of plastic NTDs, consisting of 3 sheets of CR39 (each $\sim$ 0.5 mm thick), 3 sheets of MAKROFOL (each $\sim$0.5mm thick) with Lexan (each $\sim$0.2mm thick) forming the first, middle and ends sheets of the stack. A depiction of a basic MoEDAL NTD stack is given in Figure 20. The damage zone is revealed as a cone shaped etch-pit, when the plastic detector is etched in a controlled manner using an etchant such as hot sodium hydroxide (NaOH) solution. The base area and depth of the etch-pit cones are an increasing function of the Z/β of the particle, where Z is a particle charge and β its velocity.

A more detailed description of the detector including a description of the NTD: analysis infrastructure; etching & scanning; and, calibration - is given in Section 2.

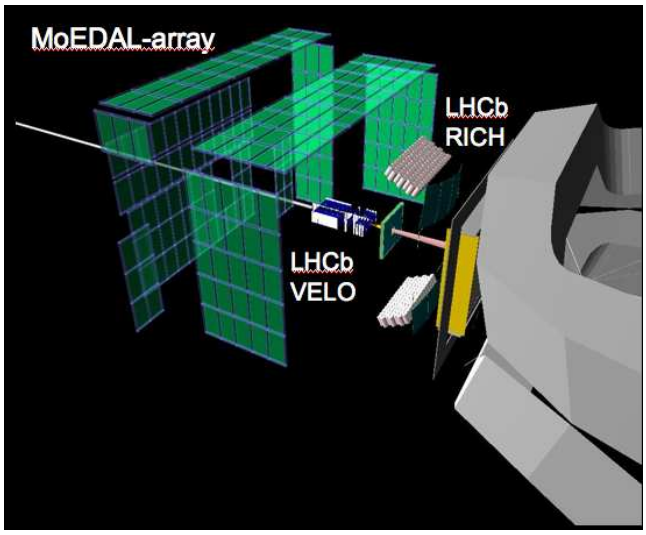

Figure 17: The picture shows the MoEDAL array occupying all the practicably available space in the VELO cavern. The surface area, covered by the MoEDAL detector is approximately 30 m^2.

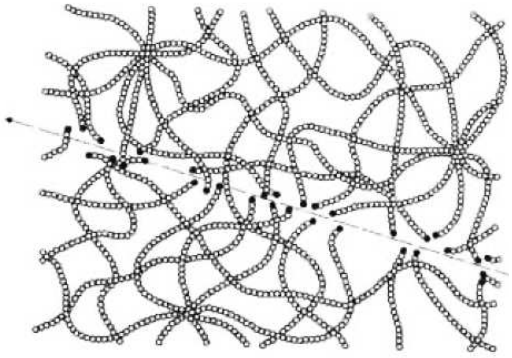

Figure 18: The breaking of the polymeric bonds by a crossing charged particle.

1.4.2 Data taking and analysis

The exposed MoEDAL NTD plastic will be shipped to INFN Bologna for analysis with a small sample being sent to the University of Cincinnati for check processing. As the first step in the analysis process the etching process will, for one sheet of the CR39 stack, be continued for a sufficient length of time for holes resulting from a highly ionizing track to be formed in the sheet. Any holes so formed can be detected using a low magnification optical system, as employed in the SLIM experiment [88]. The position of the hole in the front CR39 layer can then be used to define corresponding regions of interest in accompanying sheets in the detector stack, that can be etched with greater care.

After etching, the MoEDAL NTDs will be scanned using manually controlled and/or computer controlled optical scanners which, with special dowel-pin marker holes, allow the determination of hole position with accuracy better than ~ 50 μm in the multilayered NTDs stack used in the experiments. The response of track etch detectors versus REL can only be established by a calibration performed using ions of different charges and energies, where the calibration depends on the etching conditions. The measured base areas of the etch-pit cones (tracks) increase with increasing ion charges. The trajectory of each highly ionizing particle is reconstructed by tracking the etch cones successively through the stack.

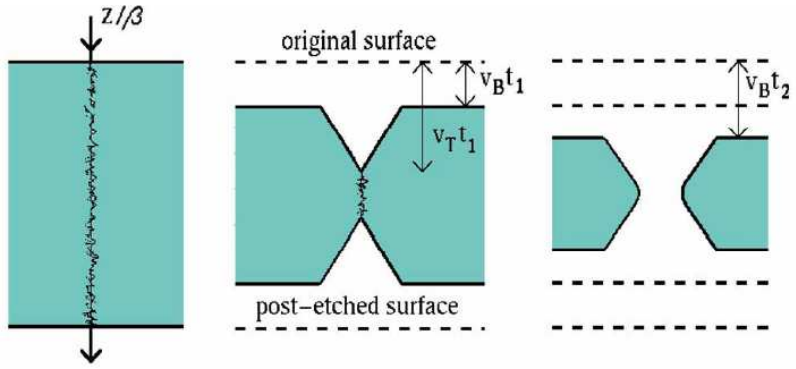

Figure 19: (a) the latent track for a nucleus with charge Z and velocity β = v/c; (b) two etch pit cones are formed on both sides of the foil; (c) a prolonged etching can make the two cones connect and form a hole.

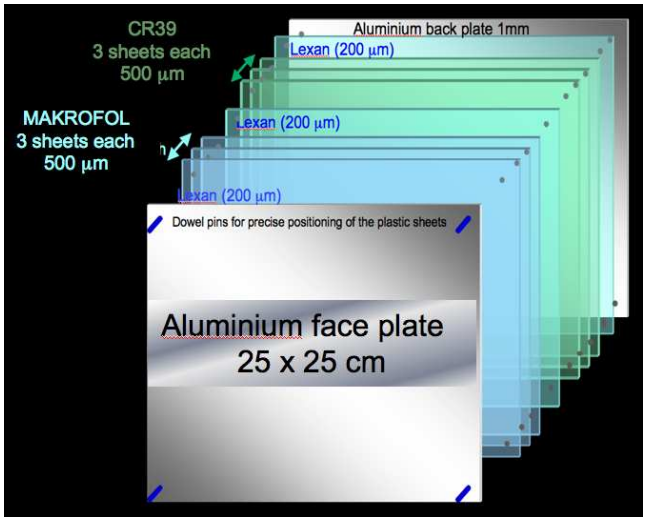

Figure 20: The basic MoEDAL detector stack consisting of 3 sheets of CR39 and three sheets of MAKROFOL with Lexan sheets at the beginning and end of the stack and separating the CR39 and MAKROFOL stacks. The size of each sheet is 25 cm × 25 cm. The stack is enclosed in an 1mm thick aluminium housing. The total thickness of the stack is 3.6 mm.

This multiple measurement can be exploited to achieve an adequate charge resolution to separate individual fragments from the incident ion beam.

A typical calibration set-up at an ion beam accelerator includes a fragmentation target and nuclear track detector foils in front of and behind a target. After exposure the detector sheets are etched in standard conditions. The calibration of the plastic will take place at the CERN North Area using a heavy ion test beam. If this option is not available another heavy ion test beam facility [89] will be utilized. If possible a number of individual sheets will be "tagged" by exposing a corner of the detector sheets at a heavy-ion beam facility prior to exposure at Point 8. The analysis of the exposed plastic requires that a number of sheets of plastic will need to be etched under differing etching conditions. Also, the positions of individual plastic sheets within a stack will need to be tracked, as well as the position of the stack within the MoEDAL detector array.

1.4.3 Proposed run scenario

It is envisaged that roughly 1 m^2 of NTDs will be deployed prior to the start of the LHC run in the fall of 2009, or at the earliest date that is compatible with the principle of non-interference with LHCb commissioning or operations. The analysis of this plastic will help us determine the parameters for the full run, for example the rate at which the plastic is changed. We envisage that the plastic will be changed at least once a year for the life of the experiment. Care will be taken to see that this deployment does not interfere in any way with existing or planned LHCb infrastructure or operations. The complete installation of the MoEDAL detector is planned for the winter of 2010/11, after the run at the lower LHC centre-of-mass energy of 10 TeV, or at the earliest date that is compatible with the principle of non-interference with LHCb commissioning or operations. It is assumed that the main run will be at a E_{CM} of 14 GeV. We request that the MoEDAL be exposed to collisions corresponding to an integrated luminosity of $\sim$ 6 fb^{-1} (3 years at the nominal LHCb luminosity).

2 The MoEDAL Detector

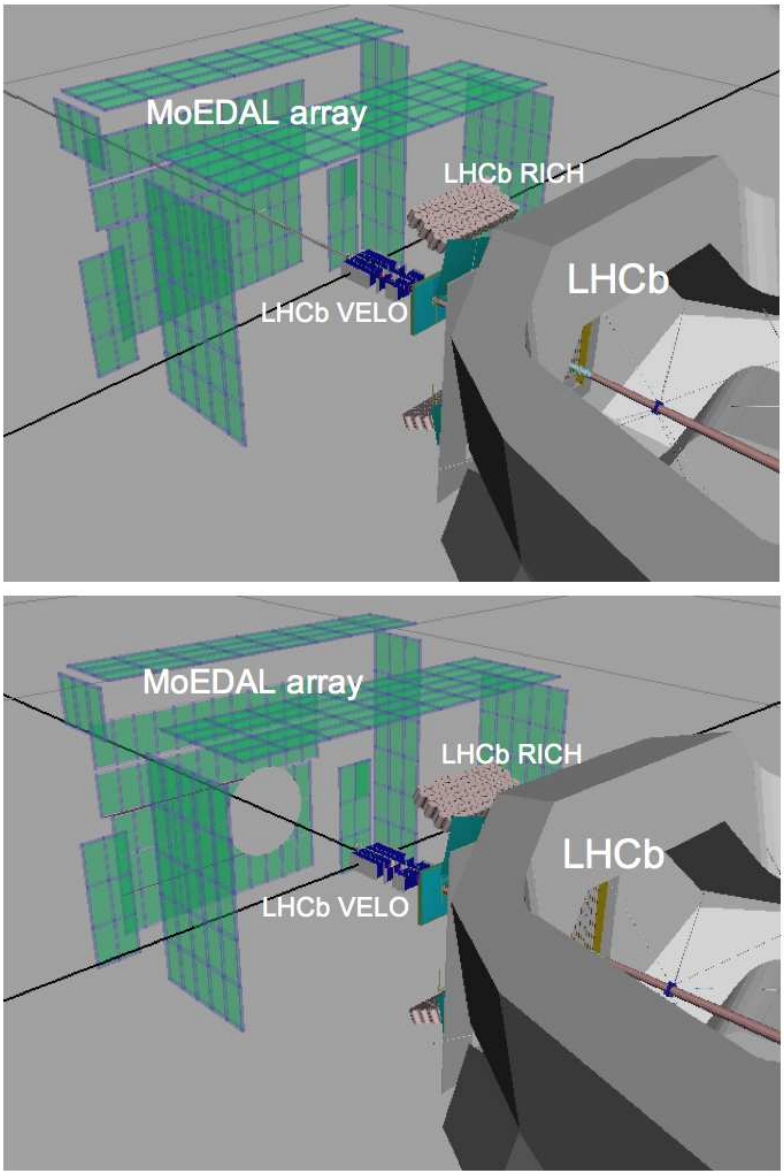

Figure 21: A GEANT4 generated depiction of the MoEDAL array and its deployment in the VELO cavern of LHCb. The upper figure shows the maximum practicable MoEDAL NTD deployment. The lower figure shows a 1m diameter cut-out region around the beam-pipe where the beam induced radiation field is the highest. The NTDs in this area may require special analysis if they cannot be changed out at least once a year.

The MoEDAL detector is comprised of an array of plastic Nuclear Track Detectors (NTDs) deployed around the (Point-8) intersection region of the LHCb detector, in the VELO (VErtex LOcator) cavern. The array consists of NTD stacks, nine layers deep, in Aluminium housings attached to the walls and ceiling of the VELO cavern. The maximum possible surface area available for detectors is around 25 m^2, although the final deployed area could be somewhat less due to the developing requirements of the LHCb detector. A depiction of the (maximal) MoEDAL array is given in Figure 21. Note that in the lower figure there is a 1m diameter cut out regions shown. This is where the beam induced radiation field is the highest. The NTDs in this area may require special analysis if they cannot be changed out at least once a year

The plastic NTDs employed by MoEDAL, consisting on 9 layers of CR39 (3), Makrofol (3) and Lexan (3), record the passage of heavily ionizing particles which leaves an invisible damage zone along its trajectory in the plastic. We envisage that he stacks will be exposed for a normal LHC operating year and then replaced by fresh NTD stacks.

For highly ionizing particles such as fast magnetic monopoles the Restricted Energy Loss (REL) of the incident particle will be constant along the trajectory of the monopole through the detector sheets. Thus, etch pit cones will be collinear and equally sized, throughout the NTD stack. This energy loss signature is easily distinguished from background of low energy particles which are slowed down and even absorbed inside the detector. In this case the etch-pit size changes (increases) along the trajectory as it loses energy.

The analysis procedure of the exposed stacks is as follows. The first CR 39 layer (with respect to IP8) of each detector stack is etched in "strong" etching conditions described in Section 3. After etching, the MoEDAL NTDs will be scanned using manually controlled and/or computer controlled optical scanners which, with special dowel-pin marker holes, allow the determination of hole position with accuracy better than $\sim$50 μm in the multi-layered NTDs stack used in the experiments. The scanning will be performed by different operators who are searching for a possible correspondence of etch-pits on the two opposite surfaces of the sheet (i.e. biconical tracks with front and back sides cone areas equal within experimental uncertainties), see for example Figure 22.

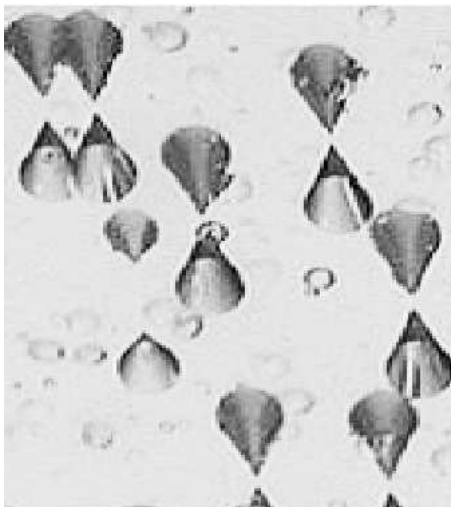

Figure 22: Biconocal etchpits in CR39.

In some cases the etching process, for one sheet of the CR39 stack, will be continued for a sufficient length of time for holes resulting from a highly ionizing track to be formed in the sheet, as sketched in Figure 42. Any holes so formed can be detected using a low magnification scan [88], or alternatively, the ammonia technique [90] where the plastic sheet is placed on top of sensitive blueprint paper and the two are sealed around the edge with tape. This package is then exposed to ammonia vapour. Each hole in the plastic is then revealed by a blue spot. The spotted blueprint paper can then be used as a map to define corresponding regions in accompanying sheets in the detector stack, that can be etched with greater care. This greatly facilitates the scanning of large areas of plastic NTDs.

If back-to-back etch pits are found in the first sheet, the position and incident angle of the candidate event are recorded. Then, the last CR39 layer is etched in soft etching conditions and accurately scanned with a high magnification optical microscope in a small region around the candidate expected position. To accept an event, a four fold coincidence between the first and the last detector layers is required (2 pairs of back-to-back etch pits).

The middle CR39 layer is scanned in soft etching conditions if back-to-back etch pits are found that align with etch pits in on or the other CR39 sheet, the middle CR39 layer will etched and be subjected to a detailed analysis. The Makrofol/lexan foils will be etched and analyzed to obtain more information if the tracks found in CR 39 are of interest i.e. are candidate signal tracks.

to separate individual fragments from the calibration beam.

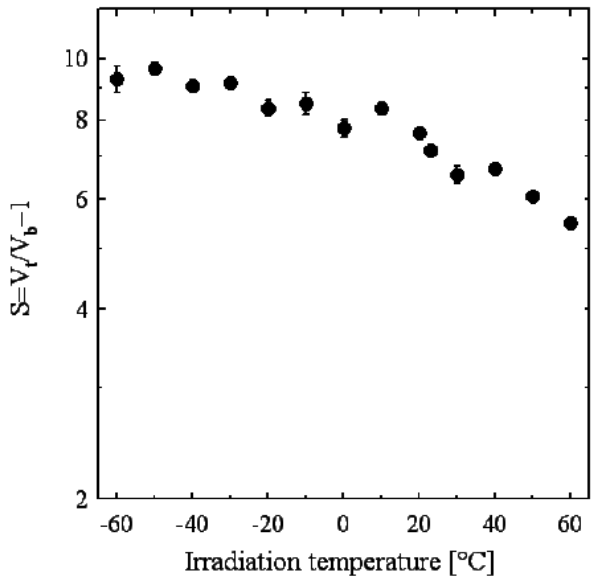

Figure 23: A plot of S (= V_T/V_B - 1) against irradiation temperature.

2.1 Track Etch Detector Properties

Many works were dedicated to the investigation of nuclear track detectors properties, in particular to the study of the effects of aging, fading, temperature changes, gamma and proton/alpha irradiation. It was found that polymeric track etch detectors such as CR 39, Makrofol or Lexan are highly stable against aging and fading effects for exposure times as long as 10 years [91] and are almost stable against temperature changes in the range between -20^{o}C and +30^{o}C. as shown in Figure 23 [92].

However, it has been shown that large gamma irradiation can affect the properties and stability of track-etch detectors of different types. A high radiation dose is known to produce structural alterations in the cross-linking or degradations in plastic polymers converting them into more etchable materials (enhancing the etch rate). For example, it was shown that the bulk-etch velocity, V_B, in CR 39 track etch detectors decreases with increasing irradiation doses while the track-etch velocity V_T increases [93], thus enhancing the sensitivity. This begins to be significant at large doses, $\sim$ 50 krad, depending on the polymer characteristics and the etching conditions, see for example the references [94] and [95]. The increase of the bulk velocity V_B for gamma radiation doses >1Mrad indicates the complete degradation of the polymer.

In the case of Lexan polycarbonates Singh and Parsher [96] found that both track and bulk velocities increase with the gamma radiation dose with a sensitivity decreasing slowly. They concluded that the gamma irradiation of Lexan begins to be effective above 103 krad.

In Table 2 are given the sensitivity and response of three types of track etch detectors

Table 1: default

Quantity	CR-39	MAKROFOL/Rodyne/lexan
Etchant	6.25N NaOH	6.25N NaOH
Dose limit (Mrad)	2	200
Etch pits/hadron (calibration)	10^{-4}	2×10^{-6}
Limiting density of etch pits (cm^{-2})	$\sim 10^8$	$\sim 10^8$

Table 2: The sensitivity of detectors to background radiation.

to background radiation and to monopoles. The detectors were deployed at the Fermilab Proton-Antiproton Collider [79]. The radiation resistance dose limit obtained for CR 39 detectors with a threshold $Z/\beta = 20$, was about 2 Mrad, whereas in the case of Rodyne (equivalent to Lexan), with a threshold $Z/\beta = 65$, it is 100 times larger i.e. 200 Mrad.

Thermal properties of track-etch detectors were also found to be affected by irradiation, but this effect is not really significant in Makrofol (Lexan). It may be important in CR 39 for high irradiation dose (100 Mrad) [97]. Results from proton irradiation experiments are more or less the same. The estimated radiation dose level at MoEDAL is expected to be sufficiently low to allow the use of CR 39 and Makrofol(lexan) for a long period without significant damage.

The NTD CR 39 has the lowest threshold ($Z/\beta = 5$). This property also renders it sensitive to background radiation. In order to improve the signal to noise ratio one can increase the threshold Co-polymerizing CR39 and an additive resin such as Dioctyl Phtalate DOP [98] or Diallyl Phtalate DAP [92] and/or choosing a strong etching procedure as defined in [99]. CR 39 can also be combined with other track etch detectors with larger thresholds (Lexan, Makrofol) as was done for the MACRO [100] and SLIM [101] experiments.

The desirable properties of plastic NTDs for the detection of highly ionizing particles at accelerators are summarized as follows:

- *Sensitivity to magnetic monopoles* - monopoles with n=1 will be detectable in CR-39 provided that $\beta \gtrsim 0.01$. Highly ionizing particles with Z/β as low as 5 - can be detected by CR39, depending on the etching conditions.
- *Insensitivity to MIPs* - CR-39, Lexan and UG-5 are totally insensitive to normally ionizing particles. For example with an integrated luminosity of $\int$Ldt = 10^{40} cm^{-2} and a rapidity interval of Δy= 2, there will be $\sim 10^{16}$ MIPs passing through the detector.
- *Solid angle coverage* - it is relatively easy to cover the full solid angle with stacks of NTDs.
- *Trigger* - as NTDs are always sensitive to monopoles and yet insensitive to normal hadronic events, no trigger is necessary with these devices. This is useful in the search for very heavy stable particles whose time of flight to, say, the muon counters of an LHC experiment could exceed the trigger time allocated for each beam crossing.
- *Monopole Properties* - the measurement of the detailed shape of the conical etch pit produced on each side of the plastic sheet gives information on the particle trajectory as well as the equivalent Z/β. In a multi-sheet stack detector, the position and direction information from individual pits can be combined to give a very precise trajectory and the Z/β values can be used to determine the change in ionization energy loss as the particle looses energy passing through the detector. Showing that

the candidate track comes from the interaction region and has consistent dE/dx values will be important checks.

- *Radiation Resistance* - the radiation resistance of track-etch detectors is examined in reference [102]. CR-39 is the most sensitive being able to stand a dose of around 2 MRads, Lexan/Makrofol can withstand around 200 MRads and UG-5 around a GigaRad. Thus NTDs are relatively radiation hard. Moreover, as the material is inexpensive, compared to usual electronic detector technology, it can be replaced when necessary.

- *Cost* - both the cost of the mechanical structure required to hold the plastic NTD stacks and the plastic NTD themselves cost very little when compared to the electronic detectors designed to do the same job with the same coverage.

2.2 Detector Unit Design

The basic detector unit of the MoEDAL experiment is a stack of nine sheets of plastic NTDs, consisting of 3 sheets of CR39 (each $\sim$ 0.5 mm thick), 3 sheets of MAKROFOL (each $\sim$0.5mm thick) with Lexan (each $\sim$0.2mm thick) forming the first, middle and end sheets of the stack. A depiction of a basic MoEDAL NTD stack is given in Figure 20.

The basic MoEDAL detector units are deployed in aluminium housings that hold 6 basic MoEDAL NTD stacks. The aluminium housing is 1.00 mm thick aluminium. The size of the housing is approximately 50 cm $\times$ 75 cm with a depth of approximately 2 cm. The weight of the housing when full of detectors is around 8 Kg. A photograph of two test housings in a test deployment is shown in Figure 24. Commercially pure aluminium alloy (1100) is utilized throughout the MoEDAL detector in order to reduce activation.

Figure 24: A test deployment of two MoEDAL aluminium housings each sin 50 cm x 75 cm in area. The outer thickness of the housing is roughly 2 cm. Each housing will hold 6 basic MoEDAL NTD stacks and weight $\sim$ 8 Kgs when fully loaded with detectors.

An important aspect of the MoEDAL detector stacks is the ability to situate a plastic NTD sheet with respect to the other sheets in the stack in order to accurately track the passage of a highly ionizing particle through the stack. This is done by the precision drilling of holes through diagonally opposite corners of the stack and placing a dowel pin through the holes in order to accurately maintain the relationship between the sheets. In addition each sheet is labeled so that its position can be reconstructed with respect to the other sheets in the stack during the etching process. This method of alignment, that has been utilized in

other NTD detector systems, will enable a per sheet registration accuracy for the track of a highly ionizing particle to be made with an accuracy of better than 50 μm.

2.3 Detector mounting system

The detector mounting system is comprised of a set of aluminium rails onto which the aluminium detector housings can be screwed. The mounting rails are cut to length and have cross-section 2.5 cm x 1.9 cm (deep). They are predrilled with two sets of holes: attachment holes that enable the rail to be attached to the concrete, in this case we have a hole for very metre of rail; and, a second set of holes, drilled every 10 cm that are used for attaching the detector housing to the frame, using M4 screws through each corner of the housing. The rails are mounted using " Hilti" 3/8" inserts with 1/4" (diam.) screws. Each mounting point is rated to take a load of 200 Kg.

This mounting system is optimized to reduce:

- Mounting operations such as concrete drilling;
- The time it takes to mount and dismount the MoEDAL detector stacks
- The "footprint" of the MoEDAL detector array in the VELO cavern.

The mounting specifications for a pair of aluminium rails are given in Figure 25. A cross-section view of the mounting of the detector housing on the aluminium rails is shown in Figure 26. A depiction of the attachment of a MoEDAL detector housing to the support rails structure lining the VELO cavern, is given in Figure 27.

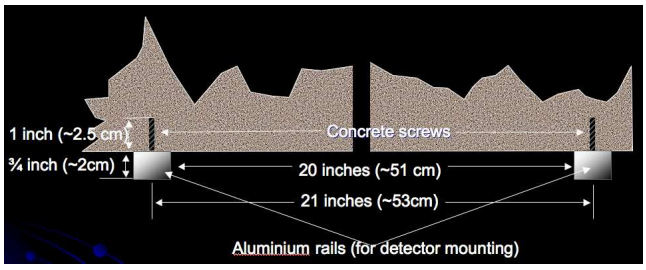

Figure 25: The mounting specifications for a pair of rails onto which the MoEDAL detector housings will be attached.

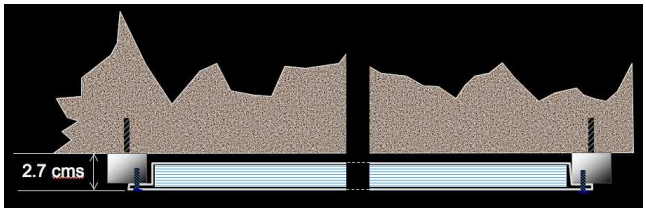

Figure 26: A diagram showing a cross-section of the mounting of a MoEDAL detector housing on the support rails.

After the detectors have been mounted in their various housings their position is fixed with respect to the rigid wall mounted MoEDAL framework. The position of the framework on each surface of the VELO cavern is recorded by survey marks attached to at least two detector housing attached to that framework. The accuracy of the registration of a highly

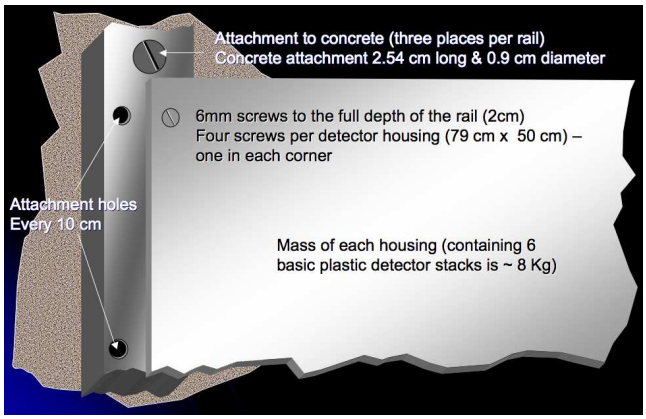

Figure 27: A depiction of the attachment of the MoEDAL detector housing to the support rails.

ionizing track in a stack combined with the accuracy with which we can place the track in the space, allows us point this track from its position near to the VELO wall, or ceiling, back to the LHCb IP with an accuracy of ~ 1 cm.

2.4 Detector installation

The installation of the MoEDAL detector array will take place in two phases. The first phase involves the deployment of a small fraction (10%-20%) of the total possible surface area of the final (second phase) detector. We expect that the first phase of the installation will take place in 2009/10. The second phase of the MoEDAL installation involves the deployment of the full detector. In both cases we expect that the installation would take place according to the following conditions:

- The LHCb collaboration has established a stable running condition in the VELO region;
- The installation will not disrupt the functioning of the VELO detector or its related infrastructure;
- The available surface area of the VELO cavern, walls and ceiling has been defined by the LHCb collaboration.

It is envisaged that the Phase1 installation will take ~ 1 working day, whereas the installation of the full detector will take around 4 working days. First, the rail mounting described directly above, will be attached to the wall. The detector assemblies that are 2.5 cm deep, measure 50×75 cm and weigh about 8 kg when full of detectors, will be attached to the rails by M4 screws. These assemblies look like flat shallow aluminium boxes.

During the installation it will be necessary to drill the concrete wall and ceiling of the VELO cavern. We will use a "dustless" drilling system, incorporating a vacuum cleaner system, to drill the holes necessary for the mounting of the rail system. In order to test the installation procedures a test installation was performed in 2007, a photograph of which is given in Figure 24.

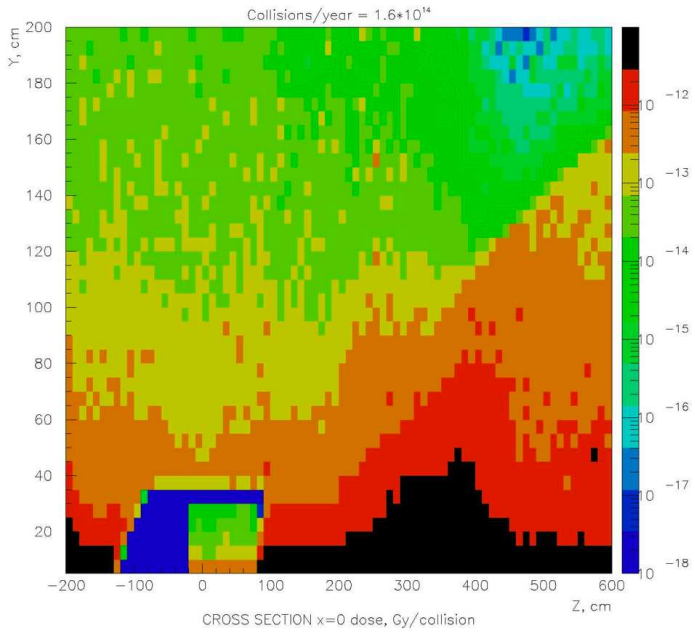

Figure 28: Map of the dose per year at nominal luminosity in the LHCb-VELO region at x=0.

2.5 MoEDAL Radiation Environment

Radiation background in the whole LHCb experiment was simulated by FLUKA package [103]. Primary events were generated with DPMJET-II program [104]. The data shown in the present paper are based on 2000 primary events. As a result of simulation the distributions of neutron, electron/positron and charged hadrons fluences were produced, as well as the maps of dose.

In the simulations the following energy thresholds were used for the transport of different particles: 1MeV for electrons and positrons, 0.1 MeV for photons, 10^{-11} MeV for neutrons, 50 MeV for anti-neutrons and 0.1 MeV for other particles. All results of the simulations are given in units normalized per one p-p collision. In order to calculate a corresponding value per second one have to multiply the results by the factor that depends on the luminosity. For the nominal LHCb average luminosity of 2×10^{32} cm^{-2} s^{-1} this factor is 1.6×10^7 collisions per second or 1.6×10^{14} collisions per LHC-year (10^7 seconds). The results of these simulations are reported in detail elsewhere [105].

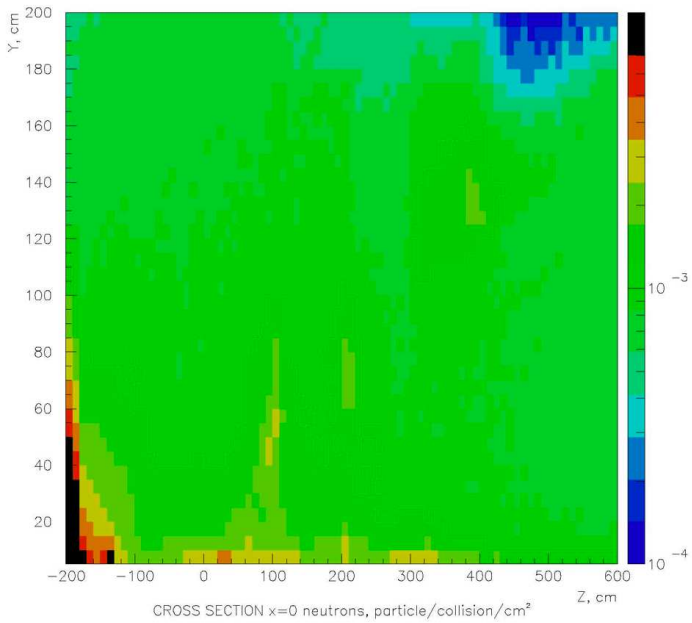

Figure 29: Map of the neutrons per square cm per year per interaction at nominal luminosity in the LHCb-VELO region at x=0.

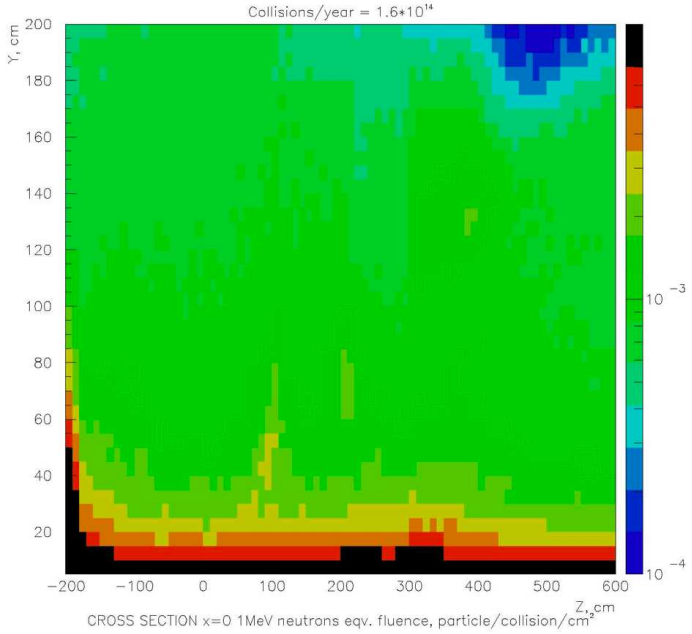

Figure 30: Map the 1 MeV neutron equivalent fluence in the x=0 VELO region.

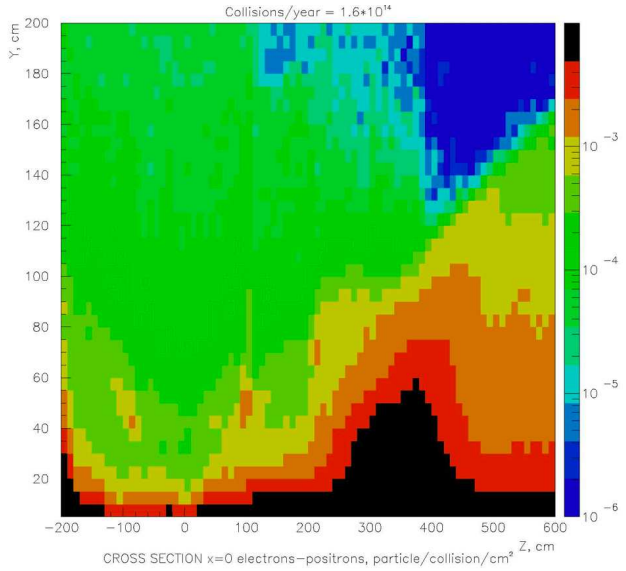

Figure 31: Map of the electrons/positrons per square cm per year per interaction at nominal luminosity in the LHCb-VELO region at x=0.

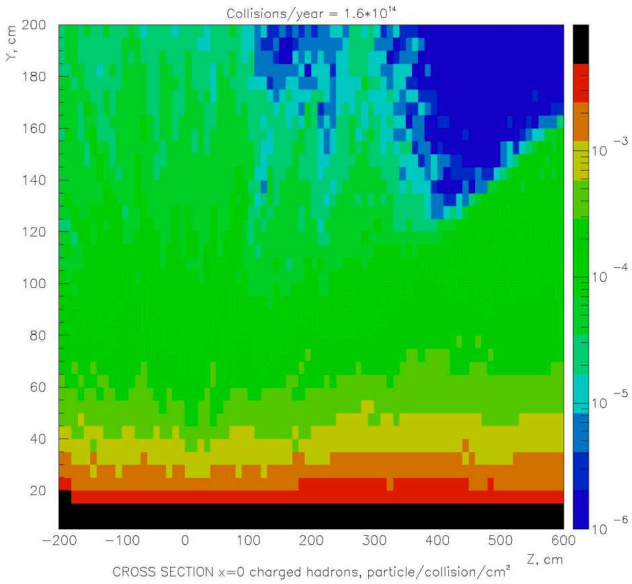

Figure 32: Map of the charged hadrons per year per square cm per interaction at nominal luminosity in the LHCb-VELO region at x=0.

An overview of the radiation background in the VELO region of LHCb [105] is shown in Figure 28 to Figure 31, where the dose map, Figure 28, and the fluences of: neutrons, Figure 29; 1 MeV n-equivalents, Figure 30; electrons and positrons, Figure 31; and, charged hadrons, Figure 32 are presented for the cross-section at x = 0. Figure 33 is included in order to facilitate the situation of the various fluence maps with respect to the main detector

The maximum value of the dose level is in the region close to the beam axis. In the tunnel around VELO the dose maximum is around 2×10^{-11} Rads/collision (37kRad/10 LHC years) at the surface of the VELO tank, dropping to 5×10^{-12}/ Rads/collision (8 kRads/10 LHC-years) at a distance of 1 m from the VELO tanks, roughly where the closest elements of the MoEDAL detector are situated.

The 1 MeV n-equivalent fluence inside the VELO tank is dominated by primary charged

hadrons. The value for the inner edge of the LHCb-VELO silicon sensors is as high as 1.5 n/cm^2/collision (2.4×10^{15} n/cm^2/10 LHC-years), while in the tunnel near the VELO tank in the vicinity of the closest elements of the MoEDAL detector the value of the 1 MeV n-equivalent fluence is approximately 10^{-3} n/cm^2/collision ($\sim 2 \times 10^{12}$ n/cm^2/10 LHC-years.

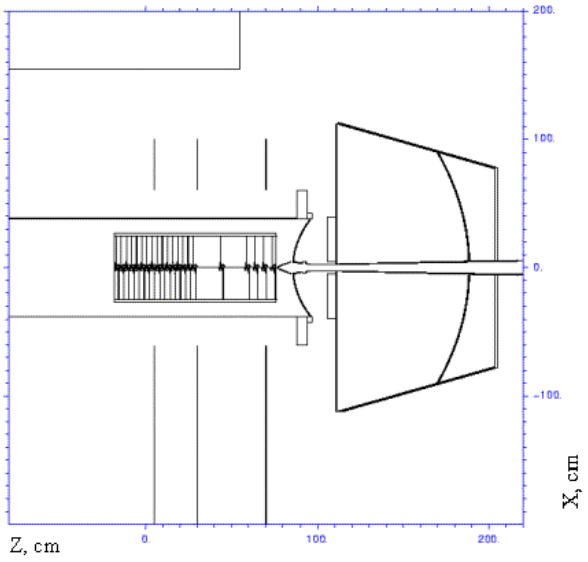

Figure 33: Map of x=0 LHCb-VELO region.

2.5.1 Activation and Intervention

The activation of MoEDAL and its environs by the radiation flux in the VELO cavern is an important consideration. Since, this would affect the handling of MoEDAL detector elements, which we envisage will be changed once a year if operating considerations require and permit. The rules that apply to interventions in the LHCb UX85B experimental hall [106] must comply with the CERN Radiation Protection Rules as compiled in the CERN Radiation Safety Manual (Code F) [107]. CERN Radiation Protection is based on the three-fold principle of "Justification, Optimization and Limitation" of potential human exposure due to the use and operation of equipment emitting ionizing radiation [108].

Any activity involving exposure to radiation has to be justified, i.e. should produce enough benefit to offset the detriment radiation may cause; practices leading to an effective dose less than 100 μSv per year to individual workers do not need to be explicitly justified.

The principle of optimization is to keep the magnitude of individual doses and the number of people exposed "As Low As Reasonably Achievable" (ALARA) below the appropriate limits, taking into account the economical factors. Practices leading to an effective dose not reaching 100 μSv/year per person professionally exposed is automatically considered optimized.

In the Safety Manual Dose Limits for workers at CERN are set. These limits must never be exceeded and are respectively 1 mSv over a consecutive 12-months period for non occupationally exposed workers and 20 mSv for occupationally exposed workers. In addition two categories of occupationally exposed workers are differentiated: category B for which a lower limit is set (6 mSv/12-consecutive-months) and category A (20 mSv/12-consecutive-months) [109][110].

Action Levels are also defined in order to minimize the individual dose and to stay well below the Dose Limits: these are measured values for which a specific action or decision is taken. The aim is to keep the dose received by any occupationally exposed worker below 6 mSv/12-consecutive months, irrespective of his/her classification category. Two action levels are worth mentioning: exposure to more than 6 mSv/year must be justified by a review of the department and SC-RP and authorized by the departmend head, the Swiss authorities need to be notified and a detailed justification has to be provided if an individual receives more than 2 mSv during a one-month period.

All interventions in a controlled area have to be planned and a Dossier for Intervention in a Radiological Environment (Document d'intervention en Milieu Radiologique, DIMR) established. Different level of optimization for an intervention need to be followed depending on threshold values for dose rates, individual and collective dose and the contamination risks for a given intervention or group of repetitive actions [111][112].

The highest level of optimization (Level III), involving the scrutinity by the ALARA committe [113] of alternative options for the work involved are respectively 2 mSv/h for dose rate, 1 mSv per intervention for individual dose and 10 mSv per intervention for collective dose.

Estimated or calculated individual and collective doses getting close to the thresholds must raise awareness and imply further optimization of work procedures. In fact any intervention in Limited Stay and High Radiation Area is subject to time limitation; this is also the case for interventions by Category B workers in Simple Controlled Area.

To give a first indication about the constraints on access during beam stops or long shutdowns we calculated the maximum working time when 1 mSv per person and per intervention are reached for different locations in the UX85B cavern for different cooling times assuming no decay shape but taking the constant dose rate value of the starting time of the intervention. This allows to identify critical interventions for which careful optimization has to be perfomed for the interventions [112]. The values are listed in Table 3 for the VELO region [106].

Table 3: default

Location	Irradiation period	1 h	1d	10 d	100 d
VELO (1 mSv)	1st month	415	835	-	-
	1st year	400	835	1665	-
	3 years	185	385	465	-
	10 years	80	125	190	385
VELO (100 μSv)	1st month	42	83	-	-
	1st year	40	83	167	526
	3 years	19	38	47	106
	10 years	8	12.5	19	38

Table 4: Maximum occupancy time after which a 1 mSv (100 μSv) accumulated dose is reached. All occupancy values are in hours. Occupancy is not shown if the corresponding shutdown is shorter than the indicated cooling time or if the calculated occupancy time is longer than the remaining length of the shutdown

The maximum working time to stay below 100 μSv per person has also been evaluated, since that is the individual dose threshold between the Level I and Level II category of optimization for interventions. The results are shown in Table 3. The values in the table are underestimated for the longer occupancy times as a flat dose rate has been assumed.

They show that the remanent dose rates in the LHCb-VELO experimental area are rather moderate and some long interventions are possible even after short cooling times. Access to the area around the VELO after the first month of operation would not give more than 100 μSv individual dose even if done almost for the whole 4 days of technical stop (42 working hours). That would also be the case of an 8 hours access after 1 hour beam stop and the equivalent of 10 years of irradiation.

From the discussion below, we see that the activation of the MoEDAL detector elements does not present a handling problem. Especially, as it takes a team of two only 10 hours to fully remove all MoEDAL detectors. By far the biggest source of dose rate arises from the VELO detector. To quantify the various uncertainties in the estimates below due to composition uncertainties, simulation errors, etc., we aim to measure the activation of a MoEDAL detector element after the first "test" run and use this as a benchmark for comparison with simulation.

In order to facilitate this measurement we aim to also place a small representative test detector and holder next to an actual MoEDAL detector in the"hottest" region of the VELO Cavern. This sample will be easily removable and should not require any dismantling of the actual detector. This test detector can be used to perform a Gamma spectroscopy measurement, allowing us to place an upper estimate of the activation of the MoEDAL detector.

Following an ALARA approach, the removal of the MoEDAL detector would be performed as late as possible in a shutdown. Unless there is a good reason not to do so. This policy is aimed at minimizing the remnant radioactivity in the detector elements and also the VELO cavern, resulting in:

- A Minimization of any dose received by the MoEDAL personnel responsible for removing and shipping the activated MoEDAL detector material to Bologna;
- The facilitation of the shipping of the activated MoEDAL material to Bologna;
- The facilitation of the acceptance and analysis of the detector material in Bologna.

Remanent Dose rate in the UX85B Cavern with the Detector in its Closed Position

The map of the ambient dose rate in LHCb experienced in the upstream end of LHCb is shown in Figure 34. The, simulation shows that the level of activation at the concrete walls of the VELO-cavern is a few μSv/h *after 10 years of irradiation with the latest years at a luminosity of* $5 \times 10^{32}\ cm^{-2}s^{-1}$. However, next to the VELO detector itself the dose rate is somewhat higher, around 10 μSv/hr. As a reference we remind the reader that the CERN area classification in terms of ambient dose is $< 3\mu$Sv/h for a Supervised area (15 μSv/h in low occupancy area) and < 10 μSv/h for a Simple Controlled area (50 μSv/h low occupancy) [109][110]. In areas where these limits are exceeded (e.g. Limited stay < 2 mSv/h) more stringent procedures for work optimization are applied.

Activation of the MoEDAL Detector

We will *measure* the activation of MoEDAL elements after one year of exposure. Using this measurement as a basis we aim to estimate the levels of activation that we will likely encounter at each major intervention, required to replace MoEDAL detector elements through the lifetime of the experiment. Here, we estimate roughly the level of activation of the MoEDAL detector elements in the MoEDAL cavern to ascertain if the dose rate we are likely to encounter at each planned intervention is likely to present a problem. Of course future estimates based on measurement will allow us to make more accurate assessments in the

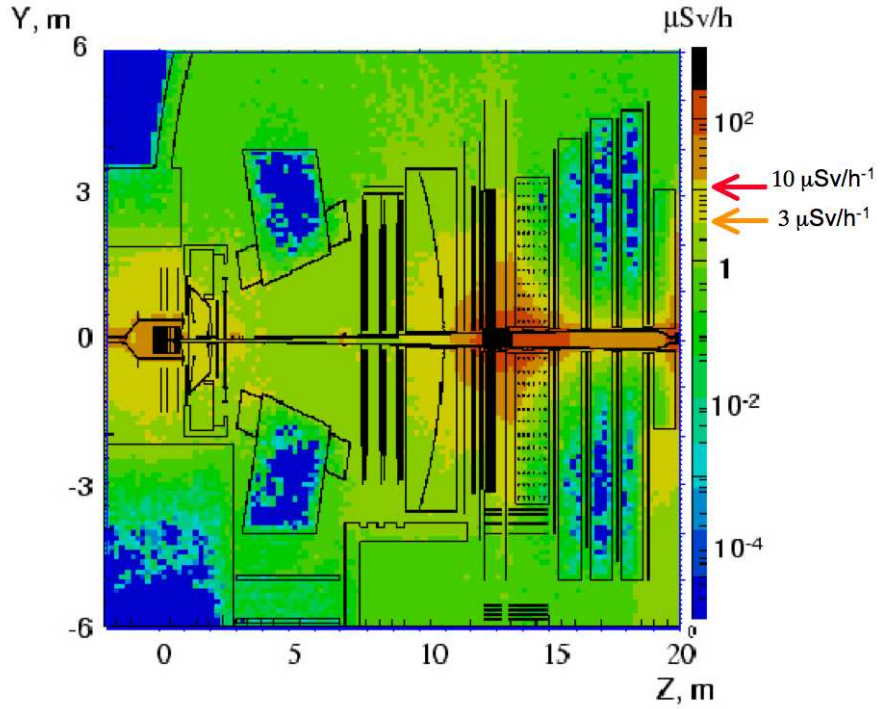

Figure 34: Map of the remanent does rate for the x=0 plane (average for -5cm $<$ x $<$ 5 cm) at the upstream end of the LHCb detector, including the VELO region, after seeing collisions corresponding to 10 years irradiation with the latest years at a luminosity of 5 $\times$ 10^{32} cm^{-2}s^{-1}, after 1 hour of cooling.

future. We note that all MoEDAL elements are more than 2m from the LHCb intersection point and more than 1 metre away from the outer envelope of the VELO detector.

Samples of different materials, typically used for LHC machine and shielding components (concrete, marble, carbon composites, boron nitride, aluminium, titanium, iron, stainless steel and copper), were irradiated at the CERF-facility [114]. At this facility, a mixed hadron beam (about one-third of it made up of protons and two-thirds consisting of pions, at 120 Gev/c) was used with a 50-cm-long copper target to create a stray radiation field around the target that is typical for loss points at high-energy accelerators. The samples, with approximately equal masses, were irradiated, with exposure times ranging from a few hours to several days and total number of accumulated beam particles ranging from 1.6 $\times$ 10^{11} to 1.5 $\times$ 10^{12}. The beam profile as well as the number of particles in each beam spill (cycle length of 16.8 s) was recorded for later use in post processing the FLUKA results.

Following the irradiation of each sample, remanent dose rates were measured with two different instruments, a portable Microspec spectrometer (Bubble Technology Industries Inc., HWY. 17, Chalk River, Ontario, Canada K0J 1J0.) as well as a Thermo-Eberline dosimeter [4] of type FHZ 672, at various cooling times and distances to the surface of the samples. The physical centres of the detectors, which are needed for an absolute comparison with the simulation, were determined with standard calibration sources in the CERN calibration laboratory to be 2.4 and 7.3 cm for the Microspec and Eberline.

For dose rate measurements, the irradiated sample was placed on a holder to allow for distances of 12.4, 22.4 and 32.4 cm between the surface of the sample In addition, the samples were directly placed in contact with the detectors. All measurements were carried

[4]Thermo Electron ESM Eberline Instruments GmbH, Frauenauracherstrasse 96, D-91056 Erlangen, Germany.

out in a laboratory with a low-background radiation dose rate of 55 nSv/h.

The results for the simulated and measured values of remanent dose rate from the concrete sample are shown in Figure 35. Both instruments show systematically higher values (20%) than those obtained from the simulations. However, the cooling time dependence is very well reproduced. Up to 2 hours of cooling, ^{11}C is the dominant isotope whereas ^{24}Na dominates between 2 and 20 hours of cooling time.

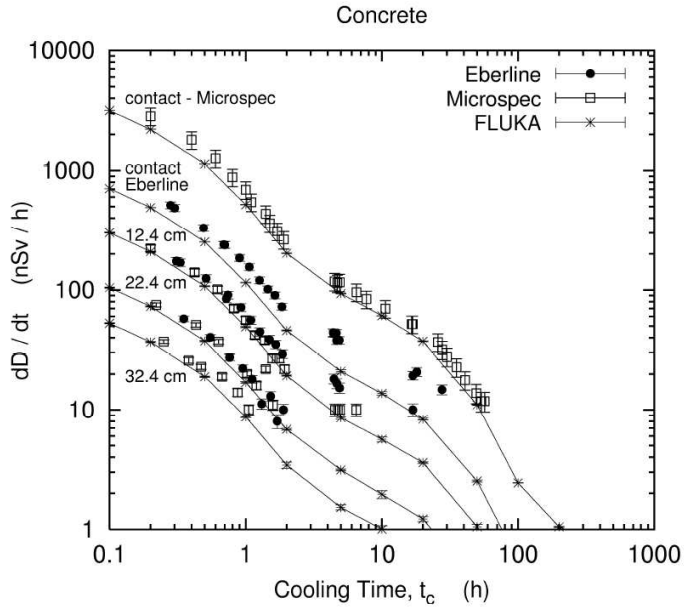

Figure 35: A plot of activity of irradiated concrete shieldings with time, after the radiation source has been removed.

Figure 36 shows the remanent dose rates as measured and simulated for one of the aluminium samples and for different distances. In general, a very good agreement is observed between the values simulated with FLUKA and measured with the Microspec instrument. On the other hand, the Eberline instrument measured systematically higher values. The cooling time dependence is very well reproduced, especially after 200 h when ^{22}Na becomes the only significant contributor to the remanent dose rates.

A comparison of Figure 35 with Figure 36 indicates, that all else being equal, concrete becomes more activated, by a factor of $\sim$2, than aluminium under irradiation - as measured several minutes after irradiation ceases. However, the concrete cools more quickly than the aluminium, taking only $\sim$2 hours to lose factor of 10 in activity. In the case of aluminium it took $\sim$50 hours to cool by a factor of 10. Obviously, these estimates depend on the constitution of the concrete and the purity of the aluminium. For example, the Aluminium used in these test is only 96.5% pure (by weight) and thus likely to become more activated, all else being equal, than the aluminium (1100) used in the MoEDAL detector which is commercially pure ($>$ 99%).

The MoEDAL detector elements consists of 0.5 mm thick, commercially pure ($>$ 99%) aluminium plates encasing 0.5 cm of polycarbonate plastic. As, the plastic is, compared to the aluminium and the concrete, devoid of heavy elements, we assume that the activation of the plastic is substantially less than that of the aluminium encasing it. We have seen from Figure 34 that after ten years of running, with that last years at a luminosity of 5 $\times$ 10^{32} cm^{-2}s^{-1} and after one hour of cooling, the activity in the region of the concrete - mostly due to the concrete - is $\sim 2\mu$Sv/h.

In reality the MoEDAL detector will only be deployed for the first few years of LHCb

running. Thus, during the lifetime of MoEDAL the activity generated in the concrete walls of the VELO cavern will be well below $\sim 2\mu$Sv/h. However, in order to arrive at a conservative estimate we will assume that this is the actual rate.

Considering the measurements discussed above and the relative cooling rates of the concrete and the aluminium we might expect that activity of the aluminium to be slightly higher at $\sim$5 μSv/h a few hours after irradiation ceases. Using the cooling rate observed above [114], this rate will have fallen by a factor of 10 to 500 nSv/h 50 hours after irradiation ceases.

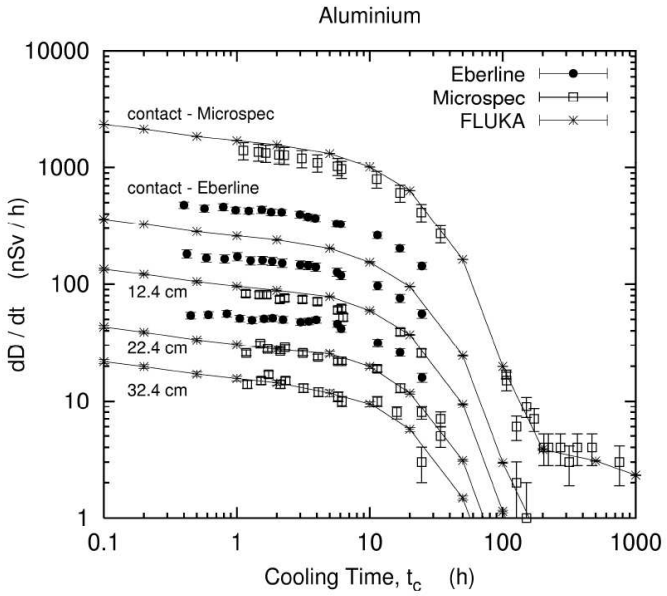

Figure 36: A plot of activity of irradiated aluminium samples with time, after the radiation source has been removed.

2.5.2 Radiation Tolerance of Nuclear track Etch Detectors

A powerful feature of etchable track detectors is that their response depends only on the dose within $\sim 10^{-6}$ cm of a particle's trajectory and is independent of dose rate. They can collect tracks for the duration of a run, the only limitation being due to degradation of the molecular structure of the detector by the accumulated radiation damage. At a hadronic collider the most severe limitation is the accumulation of short-range tracks of highly ionizing recoil nuclei produced in hadronic interactions with carbon, oxygen, and heavier nuclei in the detectors. The mean length is $\sim$ 10 μm, with an exponential tail extending, with low probability, to about the thickness of one plastic sheet. Calibrations have shown [79] have shown that the limiting density of tracks of short-range spallation recoils at one surface is $\sim 10^8 \mathrm{cm}^{-2}$, corresponding to the does limit of 2 Mrad below which the track of a long-range highly ionizing particle can still be detected. In Makrofol/Rodyne/lexan the maximum tolerable density is $\sim 4 \times 10^6$, corresponding to a dose limit of 200 Mrad. Processing, response, and sensitivity of detectors to background radiation and to monopoles is shown in Table 2

2.5.3 Monitoring of Radiation Levels in the VELO/MoEDAL Cavern

The radiation environment will be monitored using standard dosimeters, where the dosimeters are placed in selected positions immediately adjacent to a MoEDAL detector. In

addition, after the initial run in 2009/10 we are envisaging a deployment of 6 Medipix [115] radiation detectors that give a realtime response to the radiation environment. The Medipix detectors are mounted on a board, that holds the frontend readout for the chip, that is connected to a DAQ PC located in the vicinity of, but not in, the VELO cavern. The cabling requirements are modest, a cable running to each detector carrying LV power to the detector plus a signal cable carrying the signal from each detector. The computer would be connected to the network in the LHCb cavern. This deployment would only be made if it: 1) does not interfere with the running of the LHCb experiment; and (2), requires, at most, only minimal upgrades to the infrastructure at Point 8.

A Medipix-2 detector module consists of a semiconductor detector bonded to the photon counting readout electronics Medipix-2. These modules were successfully used in spectroscopic radiation measurements. This position-sensitive device, bumpbonded to a readout chip, is composed of a pixellated 300 μm thick semiconductor detector with 256x256 pixels, each of size 55 mm x 55 mm. The detector is fully controlled by the Universal Serial Bus (USB), which is presently the most widespread PC interface. The Medipix2 offers the possibility to adjust the energy thresholds, thus creating an energy window, which allows a selection of the energy of the detected radiation. A network of 14 Medipix detectors are deployed in various regions of the the ATLAS experiment in order to map the neutron radiation field.

We envisage the deployment of 5 Medipix2 detectors each equipped with two neutron converters: PE foil for conversion of fast neutrons; and, LiF layer for conversion of thermal neutrons. All 5 devices are controlled remotely by the Pixelman software. The Medipix detectors would be deployed adjacent to MoEDAL detectors in various positions in the cavern. The radiation environment at the deployment sites is low enough to ensure the survival of the Medpix chip plus its in situ frontend electronics, for the lifetime of the experiment.

2.6 Interface/integration/interference Issues With LHCb and With the LHC machine

.

The MoEDAL experiment shares an intersection region with the LHCb experiment which is the main experiment at Point 8 on the LHC ring. Although, the MoEDAL experiment is completely passive - requiring no power, gas, or readout structures - there are still a number of interface, integration and possible interference issues that have to be dealt with. These issues are discussed below.

2.6.1 LHCb Experimental Area - Brief Description and Environmental Constraints

The LHCb Detector [116] is installed in the UX85 cavern (ex-DELPHI at LEP), 100 m underground at the LHC pit 8. The layout of the LHCb experimental area is schematically shown in Figure 37.

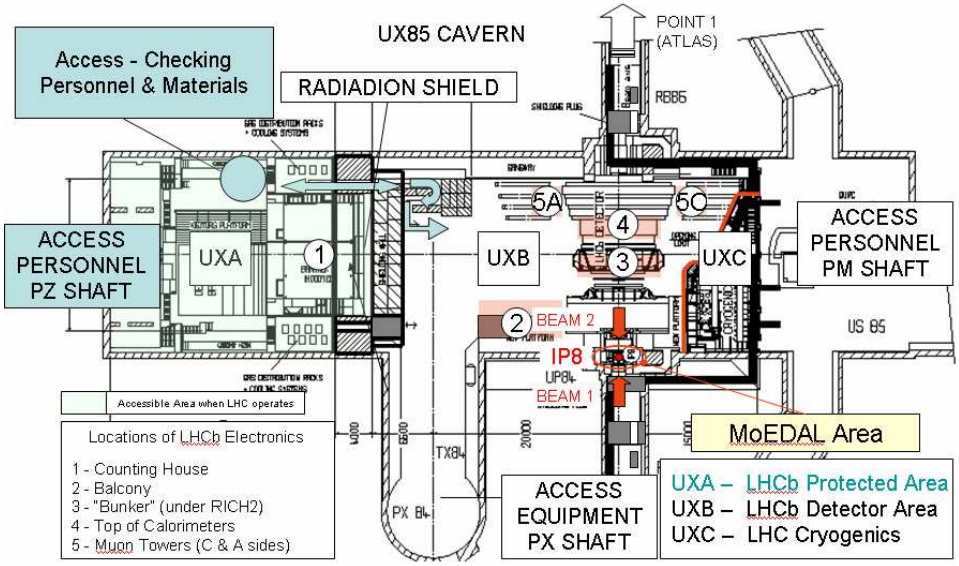

Figure 37: Layout of the LHCb Experimental Area (UX85 Cavern).

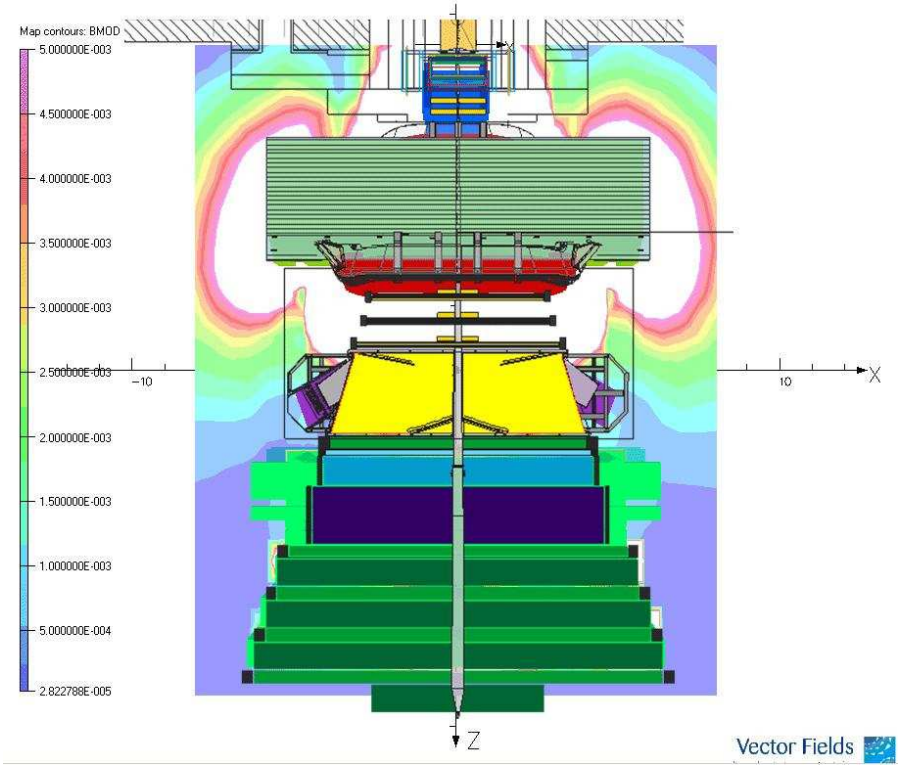

Figure 38: Magnetic field map in the LHC beam plan.

The detector area (UXB) is separated from the protected area (UXA) by a large radiation shielding wall [117][118] of 3200 tons of concrete. The UXA area is essentially dedicated to the non-radiation tolerant electronics, such as the DAQ interface electronics and the PC farm of about 2000 computing nodes in its final configuration. The UXA area is always accessible when the LHC operates. The region where the LHCb Vertex Locator (VELO) is located, is called the RB84 area. MoEDAL will be installed around the VELO on the walls of this RB84 alcove. By a LHCb convention, the observer placed at the LHC beam looking at the direction of the beam 2, on his right side, the side facing to the cryogenics area (UXC) is called C side. The side towards the UXA area is called A side.

The two major environmental constraints at the detector side (UXB area) are magnetic field and radiation. The temperature and humidity in the UX85 cavern (both UXA & UXB areas) are rather stable parameters, 20 $\pm$ 1.5 ^{o}C, 45 % respectively.

Magnetic Field The magnetic field generated by the large dipole magnet (3.6 Tm, 4.5 MVA, 6.8 kA, 1800 t) was simulated using TOSCA code [119]. The top view of the magnetic field map around the LHCb detector in the plan of the LHC beams is shown in Figure 38. In the Vertex Locator (VELO) region at the level of the walls of the RB84 alcove, the magnetic field remains below 5 mT.

Radiation Levels Radiation simulations using FLUKA code were performed [120] [121] for the large shielding wall. The ambient-dose-equivalent studies were essentially achieved for two cases: a) an accident scenario which consists of the full beam-loss, one proton beam at 7 TeV/c at the worst location of the LHCb Spectrometer and b) normal operation.. The minimum shielding requirements for the concrete wall were specified to 3 m thick for the lower part and 2 m thick for the upper part of the wall protecting the counting house. The worst locations (7.2 mSv in the case of the beam-loss scenario) are just behind the chicanes dedicated to the cabling and services at the level of the second floor of the counting house.

A radiation map in the vertical plan at the centre of the cavern is shown in Figure 39. The average value at the front part of the counting house is about 4 mSv. For the normal operation the average value is about 5.6 $\times 10^{-2} \mu$Sv only. In fact, for the modular construction using an assembly of CERN standard concrete blocks (2400 x 1600 x 800 mm^3; 7.5 t), the thickness of the concrete wall is about 3.2 m up to 4 m for the lower part and 2.4 m for the upper part providing the radiation protection expected.

Detailed radiation studies around the LHCb detector (UXB) were also performed [122] in order to estimate the total dose reached after 10 years of the LHC operation. The calculated total doses (1 MeV neutron equivalent, high energy hadrons $>$ 20 MeV; and for 10 years, assuming average L = 2 $\times$ 10^{32} cm^{-2}s^{-1}, $\sigma_{inel.+diff.}$ = 80 mbarn, 1.6 x 10^7 interactions s^{-1}, 10^7 seconds) reach in average of about 4 - 5 $\times$ 10^2 Gy on the walls of the RB84 area (VELO area).

2.6.2 Interference Issues with LHCb Experiment

MoEDAL Collaboration will adopt and endorse the following constraints:

- No access to the MoEDAL area (RB84) when the LHC operates.
- No access when no LHC beams but LHCb dipole magnet is on (e.g. tests)
- No access before getting the green light from the Radioprotection Experts during short technical stops or shut-downs of the machine.

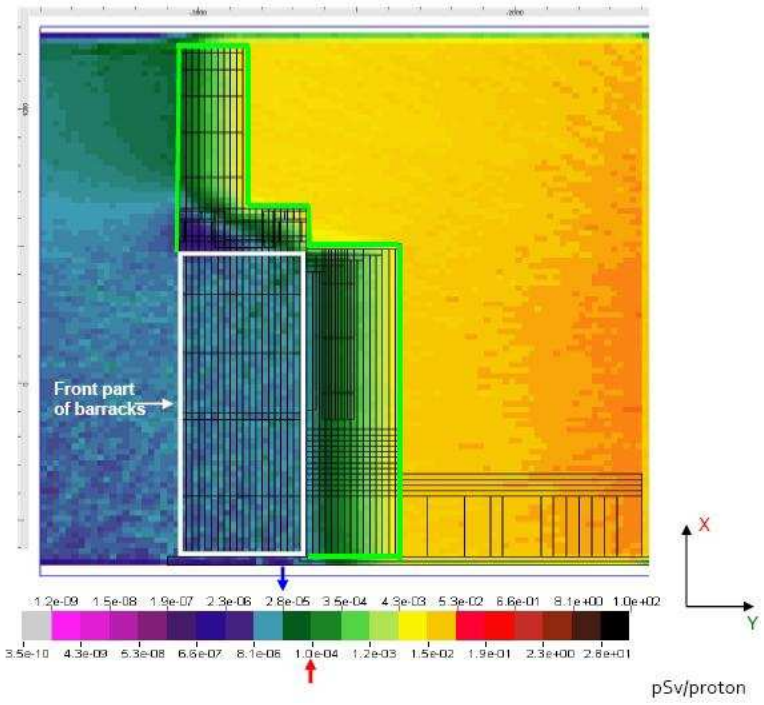

Figure 39: Ambient-dose-equivalent map showing the counting house area protected against radiation in the case of the beam-loss scenario (one beam at 7 TeV/c). Limits (4.7 x 10^{14} protons) : blue arrow = 20 mSv; red arrow = 50 mSv).

- Access (when authorized) to the MoEDAL region via the LHCb Personal Access Device (PAD) and Material Access Device (MAD) located at the PZ shaft (surface and underground). No access via the machine side (PM85) is needed.

- All the activities of installation will be prepared in advance (list of tasks) and scheduled in agreement with the LHCb operation and maintenance activities in particular with the VELO activities. The co-activities are not recommended due to the tight working space in that region.

2.6.3 Integration at the VELO area (RB84)

The MoEDAL passive sensors will be installed around the VELO equipment [123] on the walls of the RB84 alcove. The VELO region is shown in Figure 40.

The VELO region is easily accessible using the existing staircases on the A and C sides. To pass from A side to C side, one passes under the RICH2 so-called the “bunker”. The supports will be directly fixed on the walls. The vertical walls both sides of the VELO are free, no inferences with existing equipment are expected. However, the walls in front of the VELO and the ceiling are already supporting devices such as the Beam Conditions Monitor (BCM) device [124] and lift means for the VELO detector modules. The pictures shown in Figure 41, illustrate that region. For the installation on the front wall and at the ceiling special supports will be specified in order to avoid mechanical interferences with the existing items. In addition, all the materials used for supporting the plastic sheets will be non-ferromagnetic materials. The installation of MoEDAL sensors will be achieved with all the precautions required in order to avoid dust for instance when the drilling holes will be performed in the concrete walls.

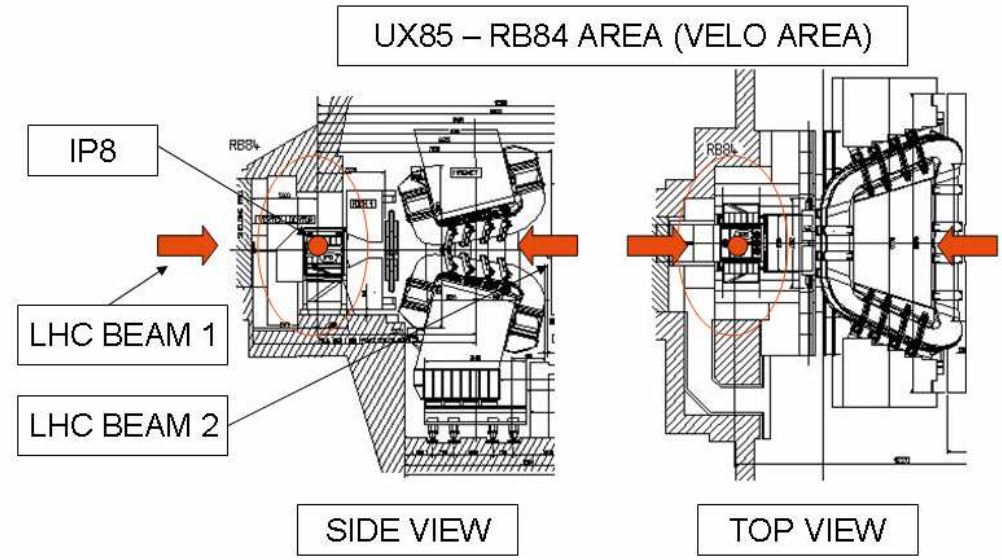

Figure 40: Layout of the LHCb detector at the VELO region (RB84 area) Side view and Top view.

2.6.4 Interference Issues with LHC Machine

No major interferences with the LHC machine are expected. No access via the machine side is needed in particular via the cryogenic area located in the UX85 cavern (UXC) or the LHC tunnel (RB84 side). The plastic sheets will be installed on the LHCb VELO side only. In front of the VELO vessel, a piece of the stainless steel beam-pipe roughly 1 m long passing across the first concrete shielding plug is not mechanically protected. During the installation of MoEDAL sensors, special precautions are needed in that region around the beam-pipe. Behind the RICH1 detector, the beryllium beam-pipe is also without any mechanical protection. The beam-pipe is supported with wires inside the magnet. That region is fragile. No access in the magnet is authorized. Special attention is required for moving objects especially long items such as rails in that region.

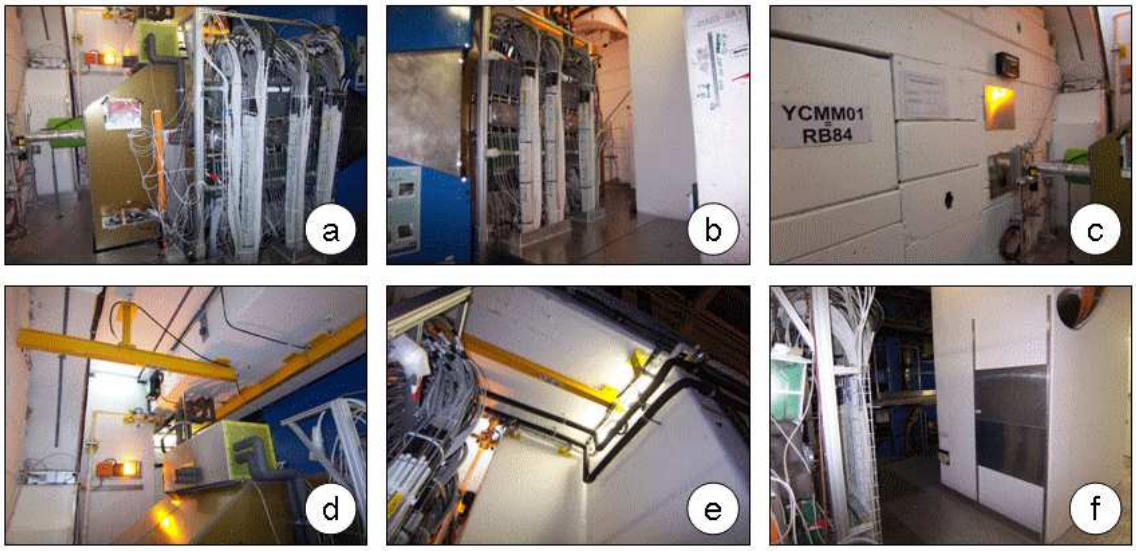

Figure 41: Pictures (September 2008) illustrating the RB84 area; a) VELO equipment (C side); b) VELO equipment (A side) ; c) Concrete Shielding Plug in front of the VELO; d) Lifting means dedicated to the VELO at the ceiling (C side); e) Rail and Cooling pipelines at the ceiling (A side); f) Probe MoEDAL support inside RB84 alcove (C side).

3 Plastic Etching, calibration and Signal Extraction

3.1 Etching of plastic track etch detectors

Two procedures, based on experience with the SLIM experiment [88], have been defined for the chemical etching of CR 39 detectors: the strong and soft etching conditions:

- The strong etching conditions for CR 39 are 8N KOH+1.5% ethyl alcohol at 75C for 30 h. It is applied to quickly remove a large amount of material allowing a better surface quality and larger post-etched cones making them easier to detect during visual scanning;
- The soft etching conditions for CR 39 are 6N NaOH+1% ethyl alcohol at 70C for 40 h. It allows etching to proceed in several etching steps in order to study the formation of the post-etched cones giving reliable measurements of the deposited energy and the direction of the incident particle. The addition of ethyl alcohol in the etchant increases the detection threshold, but it improves the etched surface quality and reduces the number of surface defects and background tracks.

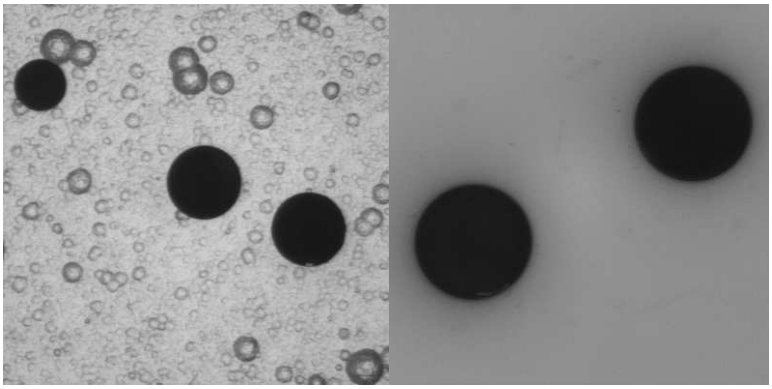

Figure 42: A GeV Pb82+ ions tracks in CR 39. Left: etched in 6N NaOH at 70C for 30h. Right: etched in 6N KOH + 10% ethyl alcohol at 70C for 3h. Both under 20X magnification.

In Figure 42 we see the differences of background and etch-pit cone dimensions in CR 39 detectors etched in standard, 6N NaOH solution at 70C for 30h, and strong, 6N KOH + 10% ethyl alcohol for 3h, conditions after exposition to a 158 A GeV Pb82+ ion beam. The chemical etching is performed in the Nuclear Track Etch Detector Laboratory of INFN, in Bologna. Stainless steel tanks are used: two large tanks (V2 and V4) of 40×55×40 cm^3 dimensions, a medium tank (V3) 40×40×26 cm^3 and two small tanks 22 × 34 ×16.5 cm^3 (TBK1 and TBK2) having different types of stirring and heating systems and of temperature control as shown in Figure 43. The stability of the etching temperature throughout the solution is maintained to within 0.01%. The detector foils are placed in the stainless steel detector holders (Figure 44) in the etching solution inside the tanks. There are three other tanks which are used for the presoaking and washing of the detectors.

The threshold for CR39 is $Z/\beta \sim 14$ in strong etching corresponding to a minimum REL_{min} $\sim$ 200 MeV g^{-1} cm^2. In soft etching conditions the threshold is at $Z/\beta \sim 7$ which corresponds to REL_{min} 50 MeV g^{-1} cm^2. In the case where CR 39 is polymerized with 0.1% DOP additive the thresholds are raised to $Z/\beta \sim 21$ (RELmin $\sim$ 460 MeV g^{-1} cm^2) for strong etching and to $Z/\beta \sim 13$ (RELmin $\sim$ 170 MeV g^{-1} cm^2) for soft etching.The etching conditions for Makrofol are 6N KOH + 20% ethyl alcohol at 50C for 10 h, and the corresponding threshold is $Z/\beta \sim$50, RELmin $\sim$ 2.5 GeV g^{-1} cm^2.

Figure 43: A view of the Bologna chemical etching Laboratory. (a) The V2 and V4 tanks are used for strong and soft etchings, the V3 tank for calibration purposes and the V1 tanks for the washing of the detectors after etching. (b) The TKB1 and TKB2 tanks, of smaller size, are used for the etching of a few detectors for calibration, TKB tank for pre-soaking, and TKB3 for their washing.

3.2 Calibration

The response of track etch detectors versus REL can only be established by a calibration, that can be performed using ions of different charges and energies. As mentioned previously the calibration is dependent on the etching conditions. The calibration procedure will be the same as that employed for the SLIM experiment [88]. A typical calibration set-up at an ion beam accelerator includes a fragmentation target and nuclear track detector foils in front of and behind a target, as shown in Figure 45.

The ion beam passes through some detector foils, interacts in the target (typically 10 mm thick Cu or Al plates) and then traverses downstream detector foils which record the survived fraction of original projectiles, as well as their fragments. The projectile fragments carry the same β and approximately the same direction of the incident ion; the Z of each resolved peak is identified via the base area spectrum.

After exposure the detector sheets were etched in the standard manner. The measured

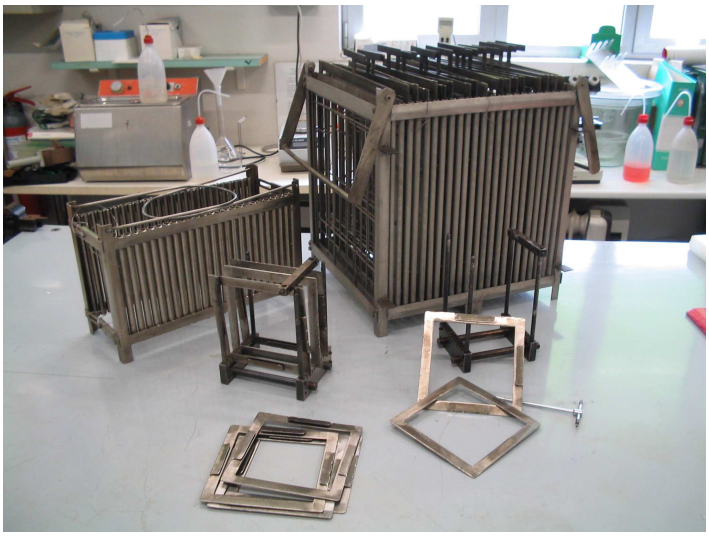

Figure 44: Stainless steel racks used for holding the CR 39 and Makrofol foils during etching. (a) Rack used for the etching of 25×25 cm^2 plastic detectors in the V2 and V4 tanks. (b) in the V3 tank for calibration and (c) in the TKB1 and TKB2 tanks..

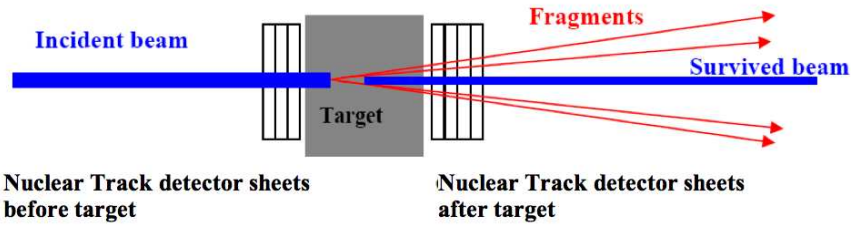

Figure 45: A Sketch of the calibration layout at an ion beam accelerator.

base areas of the etch-pit cones (tracks) increase with increasing ion charges. Thus nuclear fragments may be detected as a change in the base area of the tracks. The trajectory of each detected nucleus is reconstructed by tracking the etch cones successively through the stack. This multiple measurement can be exploited to achieve a charge resolution adequate to separate individual fragments. If area measurements of a nucleus on a single foil are distributed with a mean μ_1 and a variance σ_1^2, the average μ_n of n successive measurements is distributed with variance $\sigma_n^2 = \sigma_1^2/$ n , assuming all sheets have variance σ_1^2.

The results of the measurements of the track areas on two sheets (4 faces) of CR 39 (4 independent measurements) exposed to a 158A GeV $^{207}Pb^{82}+$ beam at the CERN-SPS are shown in Figure 46. Each peak in the graph corresponds to a different charge of nuclear fragment as indicated for some of the peaks. The resolution worsens as the charged of the fragments become large. A good charge resolution is obtained up to a charge value of Z $\sim$ 60, but for Z $>$ 74 the nuclear fragment peaks mix with the lead beam peak.

For Z $>$ 74 the base area of etch-pit cones (or diameter) is no longer sensitive to the charge variation, but the etch-pit depth (height) is sensitive and increases with increasing charge. The accurate measurement of these depths allows a better charge resolution, as can be seen from Figure 47. The combination of both etch-pit area and length measurements gives the calibration data in the whole range of REL, from the detection threshold up to 5×10^3 MeV/cm^2/g as shown in Figure 48.

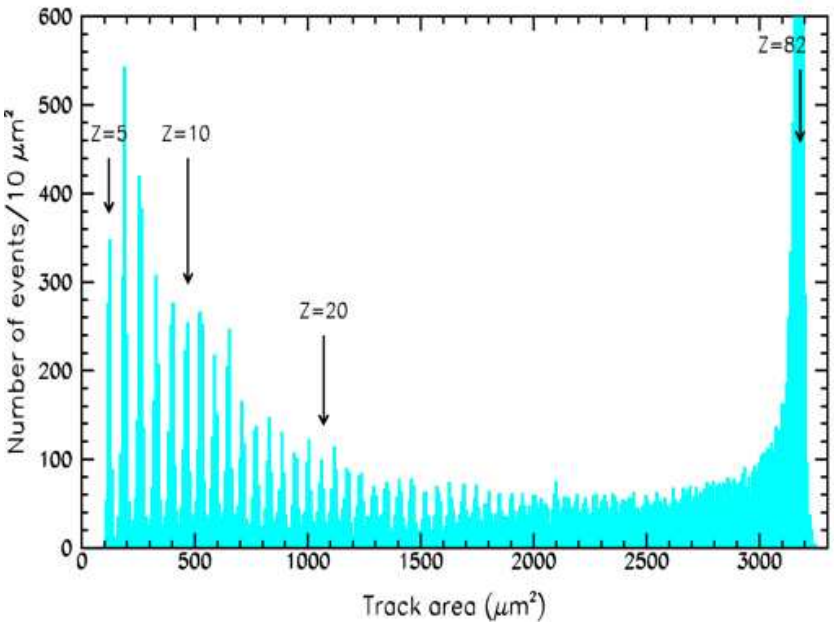

Figure 46: Etch-pit cone base areas of Pb ions and their fragments in CR 39.

3.3 Signal Extraction

After exposure, three reference holes of 2 mm diameter are drilled in each stack with a precision machine (the hole locations are defined to within 50 μm). This allows us to determine the position and follow the passage of a candidate through the stack. Each foil thickness is measured with a micrometre accuracy. The analysis starts by etching the first CR 39 sheet (defined with respect to the beam pipe) in strong conditions in order to reduce the thickness by $\sim$ 40%. After the strong etching, the CR 39 sheet will be scanned twice with a stereo microscope at low magnification, looking for any possible correspondence of etch pits on the two opposite surfaces. This procedure ensures an efficiency of $\sim$ 100% for finding a possible signal.

Further observation of an interesting correspondence can be made with an optical 2040X stereo microscope allowing us to classify it either as a defect or a candidate track. If a candidate track is found it is then examined under an optical microscope at larger magnification to measure the axes of the base etch-pits in the front and back sides of the foil.

A track is defined as a candidate if the computed p and incident angle θ on the front and back sides are equal to within 20%. For each candidate the azimuth angle ϕ and its position P referred to the fiducial marks are also determined. The uncertainties $\Delta\theta$, $\Delta\phi$ and ΔP define a coincidence area ($<$0.5 cm^2) around the candidate expected position in the other layers, as shown in Figure 49. The third CR 39 layer is etched in soft etching conditions, and an accurate scan under an optical microscope with high magnification (500X or 1000X) is performed in a square region around the candidate expected position, which includes the"coincidence" area. If a coincidence between the first and last CR 39 sheets is detected, the CR 39 middle layer is also analyzed.

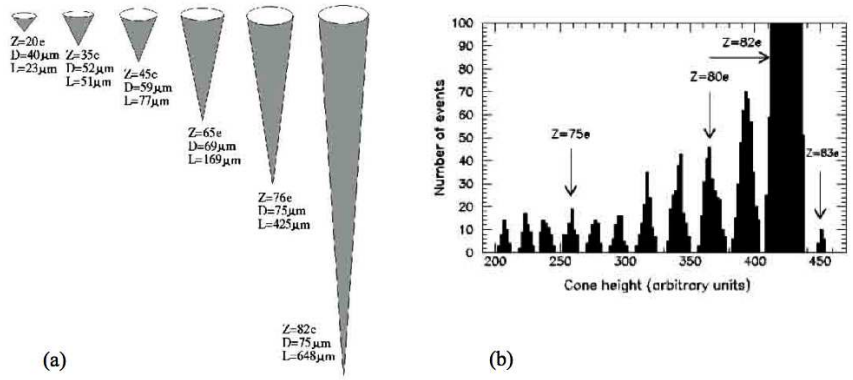

Figure 47: (a) For nuclear fragments with Z > 74, the track area measurements are not too sensitive to charge variations. In this case a better resolution is obtained by measuring the etch-pit cone depths. (b) Etch-pit cone depth (height) distributions of tracks from lead ions and its fragments.

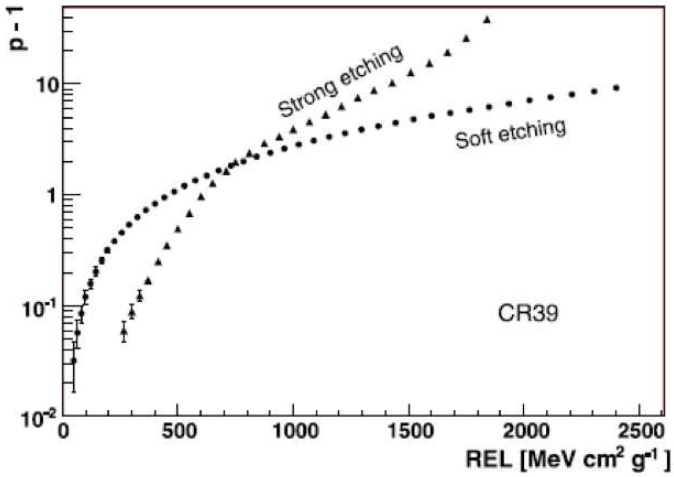

Figure 48: CR 39 calibration data p-1 versus REL of CR 39 track etch detectors in strong and soft etching conditions, see text.

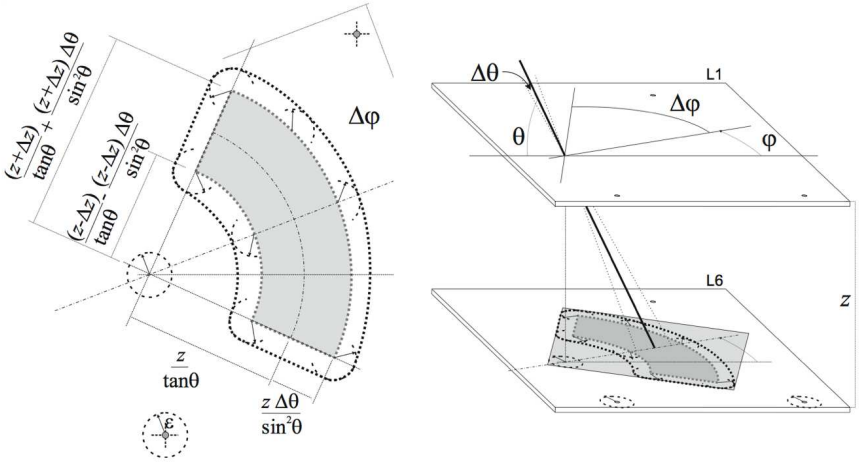

Figure 49: CR 39 calibration data p-1 versus REL of CR 39 track etch detectors in strong and soft etching conditions, see text.

4 Safety Issues and Irradiated Plastic Handling

The only safety concern flagged by the CERN TIS group was the use of flammable plastic NTDs in the underground "VELO region" of Point 8. This issue was the subject of a successful derogation request, discussed immediately below. Another concern related to the handling of the plastic NTDs after irradiation. The issue here is the requirement to remove the plastic from a designated radiation area, for processing at a remote site. The required procedures, developed in discussion with the CERN radiation safety group, are given in Subsection 4.2 below.

4.1 Plastic Flammability

The plastics used in the MoEDAL detector system are all polycarbonate, they are CR-39, MAKROFOL, and Lexan. The statement made about polycarbonate plastics in the CERN TIS (IS 41) document "*The Use of Plastics and other Non-Metallic Materials at CERN with respect to Fire Safety and Radiation Resistance*", is as follows:

"*2.4.2 Polycarbonates (PC)*

Even standard polycarbonates (e.g. Makrolon) are considered to be better than flame retardant acrylics. They are high smoke emitters and some fire retardant grades may give even greater smoke and fume emission if the polycarbonate stays in the fire area. Most grades do not drip and tend to melt away from a fire, thus exhibiting a kind of self-extinguishing behaviour limiting the spread of fire and reducing the smoke and fume emission. They may be used in some less critical areas where acrylics would not be allowed but any large scale use should be avoided."

A SC/GS-GC derogation request, No. 893563, for the use of non-metallic materials not conforming to safety instructions IS 41, was submitted to the CERN Safety Commission (SC) in 2008. In the request it was noted that that the plastic detectors will be completely encased in aluminum plates of thickness 1mm and that no plastic edges would be visible. The request was approved (EDMS no: 893563) by Maurizio Bona, head of CERN SC, and the document released by Jonathan Gulley (CERN SC)) on 2008-05-28.

4.2 Irradiated Plastic handling

In order to access the LHCb cavern through the Access Devices (PAD and MAD) MoEDAL people will attend all the standard LHC safety courses and follow LHCb access procedures. In addition to the general safety, LHC level 4 and LHCB-U (underground) are also mandatory. For removing the slightly radioactive components from the detector area (UXB), MoEDAL will apply the LHCb procedure and removed components will be deposited in the dedicated LHCb underground buffer area in order to be checked for radioactivity. The slighlty radioactive items will then be handled following all relevant procedures.

The LHCb procedure [125] to move IN/OUT materials to or from UXB area will be adopted where appropriate by the MoEDAL experiment. This procedure is summarized as follows.

1. All the materials which were in the UXB zone when the LHC beams have circulated should be checked by RP qualified personel (DG-SCR) and cannot be checked only by the owner of the materials. The role of the LHCB responsible being to arrange the test.

2. Tools/equipment brought in and used for the intervention:

- Verify you are bringing out all tools you have entered in the zone for the intervention.
- Check every tool with the PICOMUR (the counter at right, just after the MAD in UXA).
- If the dose rate is below 0.06 μSv/h, the tool can be taken away without further radiological check.
- If the dose rate exceeds 0.06 μSv/h, the tool must be put in the buffer zone under Delphi (UXA). Then you inform the LHCb RPE and CERN Radioprotection (DG-SCR) who will check again your materials.

3. Removing materials from UXB area :

   - Check every piece with the PICOMUR (the counter at right, just after the MAD in UXA). You will need to enter the value in the logbook;
   - The materials must be put in the buffer zone under Delphi (UXA). Then you inform the LHCb RPE and CERN Radio Protection who will come to re-check your materials;
   - Fill the logbook which is permanently on the desk beside the PAD (1 form/piece);
   - You will be informed when the measurements are achieved and about the radiological classification of materials.

4. Entering materials in UXB:

   - Fill the logbook available on site.

5. Filling logbook instructions:

   - If the equipment has already a bar code, it is enough to write down the label, your name, the destination, the date/hour fields;
   - Enter the dose rate which you have measured using the PICOMUR detector;
   - If the equipment have no bar code yet, all fields must be filled in;
   - Official LHCb documents with naming and label conventions [125] can be found in the same folder available on site;

A further level of handling required by MoEDAL as its basic detector elements, CR39, MAKROFOL and lexan are required to be removed from the radiation area and send to the INFN Bologna for etching and scanning. In this case the following additional procedures will be followed:

1. All the materials which were in the UXB zone when the LHC beams have circulated must be checked by RP qualified personel (DG-SCR) prior to shipping to Bologna and cannot be checked only by the owner of the materials;

2. All materials must be shipped according to the rules and regulation pertaining to the shipping if lightly irradiated materials

3. Accepting MoEDAL plastic at the Bologna site:

   - The plastic will be received and handled by the Chief radiation Officer of INFN Bologna or some suitable designated person. The plastic will not be released until it is deemed safe to handle by the Radiation safety Officer at INFN-Bologna;
   - Every piece of plastic will be checked for radiation the readings obtained will be entered in a logbook and an electronic log book that is kept at Bologna. The electronic log book should be accessible by his or her CERN counterpart;

- The materials must be put in a secure zone at Bologna prior to handling.
- The etchants and scanning devices used to process and analyze the MoEDAL plastic must be regularly checked (each month) by a Radiation Safety Officer at INFN-Bologna and the results recorded in the Bologna log book.

5 Project Planning

MoEDAL is a passive detector array that does not require gas, power or electronic readout. The placing of MoEDAL array elements on the walls and ceiling of the VELO cavern permits completely free access to the LHCb detectors and infrastructure in the VELO cavern. It is envisaged that roughly $10 \rightarrow 20\%$of the maximum possible surface area of plastic NTD detectors (~ 25 m^2 of VELO cavern area) will be deployed prior to the start of the LHC run in the summer of 2009. During this initial deployment the support framework for the complete detector will be installed on all available wall surfaces and on the ceiling. At this time care will be taken to see that this deployment does not interfere in any way with existing or planned LHCb infrastructure. The complete installation of the detector is planned for the winter of 2010. It is envisaged that the plastic will be changed once a year for the remaining life of the experiment.

The MoEDAL NTD plastic will need to be changed once a year and new plastic installed. The exposed plastic will need to be assessed by radiation safety officers at CERN and shipped to INFN Bologna for analysis according to the CERN regulation for the transport of a material from a radiation zone. This will require liaison between the CERN based experiment and the NTD analysis effort based at INFN Bologna. Strict accounting of all transactions involving the transportation and analysis of the NTD plastic that is transported from a radiation zone at CERN to Bologna will need to be kept. In addition, we envisage that a CERN based liaison with the LHCb collaboration should be maintained to ensure that any issue relating to the joint use of the VELO cavern by the LHCb and MoEDAL collaborations is quickly resolved.

The calibration of the plastic will take place at the CERN North Area using a heavy ion test beam. If this option is not available another heavy ion test beam facility [89] will be utilized. If possible a number of individual sheets will be "tagged" at the test beam facility prior to exposure. The calibration test beam program must continue throughout the life of the MoEDAL experiment. The analysis of the exposed plastic requires that a number of sheets of plastic will need to be etched under differing etching conditions. Also, the positions of individual plastic sheets within a stack will need to be tracked, as well as the position of the stack within the MoEDAL detector array.

Last, but not least, a number of physics topics will be covered by the MoEDAL collaboration requiring organization of: physics working group meetings; topic assignment; conference talk allocation; review of papers prior to publication, etc.

5.1 Organization

The organization of the MoEDAL collaboration is shown in Figure 50. the relatively small size of the collaboration, allows a "flatter" organization hierachy than usual. Thus, many decisions can be taken by the whole collaboration, together.

However, the project requirements described require a definite specification of responsibility shown in Figure 50 and described as itemized below.

- *The collaboration board* - has the responsibility to: oversee collaboration rules; allocate conference presentations; approve publications, along with the spokesman, deputy spokesman and convenors; and, the approve changes to the MoEDAL program (which in turn must be agreed to by the LHCb collaboration).

- *The spokesman and deputy spokesman* - the spokesman: plays a leadership role in the MoEDAL collaboration; is responsible with the run coordinator for any discussions

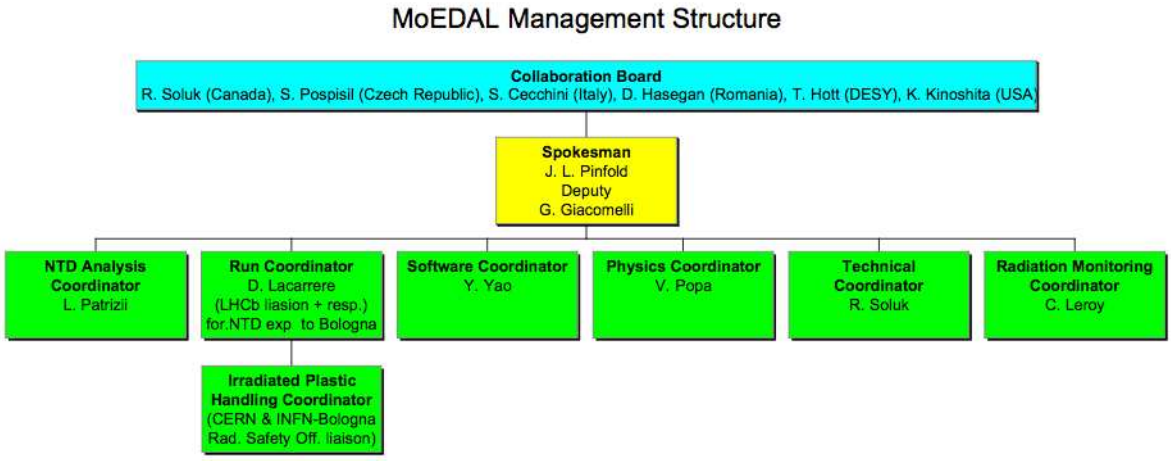

Figure 50: The organization of the MoEDAL Collaboration.

with the LHCC and the LHCb collaboration. The deputy spokesman can take over the responsibilities of the spokesman when required.

- *NTD analysis coordinator* - is responsible for all aspects of the analysis and calibration of the exposed plastic as well as the acquisition of new plastic.

- *Run coordinator* - is responsible, along with the spokesman, for liaison with the LHCb collaboration; the day to day running concerns of MoEDAL experiment; along, with the technical coordinator, The run coordinator together with the technical coordinator is responsible for the installation of new plastic and radiation checking and shipping of the exposed plastic to Bologna and the paperwork associated with this process.

- *Technical coordinator:* will oversee the preparation of the MoEDAL detector infrastructure for installation; lead the installation of this infrastructure and the MoEDAL detector stacks as well as the interchange of exposed MoEDAL NTDs for new NTD stacks; and, assist the run coordinator in the transfer of the exposed plastic to Bologna.

- *Radiation monitoring coordinator* - has the charge to: arrange for the monitoring of radiation levels in the vicinity of MoEDAL; liaise with his or her opposite number in the LHCb collaboration; and, liaise with the CERN radiation safety officer to establish the procedures for radiation checking of exposed plastic

- *Irradiated Plastic Handling Coordinator (Bologna)* - is accountable for: the reception of the irradiated plastic at the INFN Bologna site in liaison with the INFN-Bologna radiation safety officer; the tracking of the plastic through the analysis chain; and, in liaison with the Run Coordinator at CERN, the preparation and storage of paperwork required by CERN for the transportation of material from within a radiation area.

- *Physics Coordinator:* oversees the overall physics effort of the MoEDAL collaboration; facilitates the allocation of physics topics to students; sets up and chairs individual paper "blessing" committees; and, approves publications (along with the collaboration board, the spokesman & deputy spokesman, and the other convenors)

- *Software Coordinator* - is responsible for the simulation software and analysis tools and the required software setup at each site.

5.2 Responsibility for Construction and Installation, Plastic Analysis and Radiation Monitoring

The preparation of the framework, and aluminium housings is the responsibility of the Alberta group. The preparation of the plastic stacks is in the charge of the Bologna group. The installation of the MoEDAL detector infrastructure plus detectors and the interchange of new detectors for exposed detectors, will be performed by all groups - led by the Technical Coordinator. The analysis and calibration of the MoEDAL plastic NTDs is the job of the Bologna group. The Montreal group will be in charge of the preparation and deployment of all MoEDAL radiation monitoring devices.

5.3 Construction/Installation Schedule and Budget

The construction/installation schedule, taking into account the latest (February 2009) LHC schedule, is as follows:

- *May 2009* - measure and mark out VELO cavern walls for MoEDAL deployment
- *May-July 2009* - prepare the MoEDAL detector detector framework and housings at Alberta;
- *July 2009* - Drill holes for MoEDAL support framework
- *July 2009* - Ship framework to CERN and housings (for initial deployment) to Bologna;
- *June, July of 2009* - assemble 1m^2 of plastic stacks (total area of plastic is 9 times this area as there are 9 sheets of plastic per stack) mount them into the housings supplied and shift them to CERN for installation in the VELO cavern;
- *July/August of 2009* - instal MoEDAL framework and initial deployment of MoEDAL detectors in the VELO cavern at CERN;
- *Winter shutdown 2010* - dismount exposed plastic NTD detector stacks and ship to Bologna for analysis, also measure the activity induced in aluminium holders and mounting elements;
- *Winter shutdown 2011* - install any radiation monitors required, in the VELO cavern, this deployment will include the realtime MEDIPIX monitors, if there installation is approved by LHCb;
- *January, February of 2011, 11, 12* assemble a full complement ($\sim 25\text{m}^2$) of plastic stacks (total area of plastic is 9 times this area as there are 9 sheets of plastic per stack) mount them into the housing supplied and shift them to CERN for installation in the VELO cavern;
- *February/March of 2010,11,12* - instal full complement of MoEDAL detectors in the VELO cavern at CERN;
- *Winter 2010, 11, 12* - dismount exposed plastic NTD detector stacks and ship to Bologna for processing;
- *February/ March 20010, 11,12* - install or refresh any radiation monitors required in the VELO cavern.

In the above schedule it is assumed that the requested luminosity of 6 x 10^{39} cm^{-2} s^{-1} at 14 TeV centre-of-mass energy, is acquired in three years of LHC running at Point 8, starting in 2011.

The budget for this work, with manpower or travel costs, is as follows:

- Construction of the full MoEDAL detector mounting framework - 12K CHF;
- The CR39 plastic cost is 450 CHF/m^2 , the cost of MAKROFOL is 150 CHF/m^2 and the cost of LEXAN is 50 CHF/m^2;
  - The cost of the plastic NTD detectors for the initial deployment in 2009 is 2000 CHF;
  - The cost of a maximum possible area deployment of plastic in 2010,11 and 12 is 49K CHF per year.

5.4 Request for experimental conditions and other support

MoEDAL needs some technical support, in particular at pit 8. In order to prepare and optimize the installation of the supports for the plastic sheets, a mockup of the VELO (scale 1) area will be useful. A standard room of about 20 m^2 is also needed as small workshop dedicated to MoEDAL Team. For the installation around the VELO, a technical assistance will be required also such as installation of suitable scaffoldings in order to reach the upper parts of the walls and the ceiling ($\sim$3.5 m high) and installation of the protective devices. In addition, an office will be required for MoEDAL members - to be shared by MoEDAL members based at CERN and visiting CERN.

Appendices

A MoEDAL - A Heavy-Ion Running Scenario

This Technical Design Report is intended to describe Phase-1 MoEDAL *pp* running. However, the MoEDAL Collaboration is studying a heavy-ion running scenario, for a future request for beam time. Examples of two physics topics in this arena are briefly discussed below. Irrespective of the physics case, there are two important questions to answer before a case can be made for running MoEDAL in the LHCb VELO region with heavy–ions. First, is it possible to initiate heavy-ion collisions at point-8 and if so will the luminosity attainable be useful? Initial expert opinion concerned suggests that this might be possible, in principle. Although, this conclusion might change after the matter has been studied in more detail. Second, would the LHCb collaboration agree to allow heavy-ion running to be initiated at point-8 and if so under what conditions? If heavy-ion running at point 8 is achievable a number of searches for new physics become possible with MoEDAL.

A.1 Searching for Magnetic Monopoles with Heavy Ions

The seach for Monopole production in nucleus-nucleus (AA) collisions has been proposed [9][10] and performed [11]. In very-high-energy nucleus-nucleus collisions hadronic matter will become thermalized and will exist possibly even in a colour-nonconfining phase [12]. It has been shown [12] that the density of the quark-gluon plasma produced is such that it is energetically possible to produce exotic particles such as Dirac magnetic monopoles in enough quantity to be physically observable. The Drell-Yan magnetic monopole production mechanism is supplemented by the thermal production of magnetic monopoles in nucleus-nucleus collisions via the fireball model. This thermodynamic enhancement in fact rivals the Drell-Yan rate for small-mass muon pair production [9] and, while not rivaling it for magnetic-monopole pair production, makes a nonnegligible contribution to the overall production rate. We are also investigating a search for magnetic monopoles produced during heavy-ions collisions at the LHC that may be the subject of a future request. This interest is motivated by the expected Z^4 enhancement in $\gamma\gamma$ production [126] of magnetic monopoles. On the other hand, this benefit of this enhancement is countered by the rapid fall in the intensity of $\gamma\gamma$ interaction with the produced particle mass [127].

A.2 Detecting Strangelet Production

Strange quark matter (SQM; up, down and strange quarks in equal proportions, in the boundless limit) has been hypothesized to be the ground state of Quantum Chromodynamics [128]. SQM nuggets are supposed to be stable for all baryonic numbers in the mass range from heavy nuclei ($A \sim 300$) to strange stars ($A \sim 10^{57}$). While super-massive SQM aggregates could be found in cosmic rays as "nuclearites" [129], relatively low mass ones ("strangelets") could be find in high altitude cosmic ray experiments or in very high energy nuclear collisions at accelerators. At the LHC, in collisions of nuclei as heavy as Lead with a center of mass energy of about 5.5 ATeV, strangelets with TeV masses could be produced.

Strangelets should be characterized by an anomalously low charge to mass ratio (Z/A) compared to the nuclear values. There are different strangelet structure hypotheses assuming a "simple" multiquark bag, the charge to mass relation is [13]:

$$Z \approx 0.1 \cdot \left(\frac{m_s}{150MeV}\right) \cdot A \text{ for } A \ll 10^3 \tag{12}$$

$$Z \approx 8 \cdot \left(\frac{m_s}{150MeV}\right) \cdot A^{1/3} \text{ for } A \gg 10^3 \tag{13}$$

where m_s is the actual strange quark mass. In ref. [14] it is shown that an even more stable state of the nuclear matter could exist, due to the occurrence of a Cooper-like pairing between quarks of different color and flavor numbers, the so called Color Flavor Locked (CFL) strangelets. In this case, the charge to mass relation becomes:

$$Z \approx 0.3 \cdot \left(\frac{m_s}{150MeV}\right) \cdot A^{2/3} \text{ for } A \gg 10^3 \tag{14}$$

MoEDAL offers a unique opportunity to look for objects such as the strangelet at the LHC. The good charge resolution (actually, Z/β resolution) and low threshold of MoEDAL's CR39 plastic nuclear track detector favour such a search. Low charge nuclear fragments will be stopped by the beam pipe, the VELO detector and the infrastructure surrounding the intersection point. Strangelets, due to their larger mass could be detected as coincident etch-pits forming tracks in our NTD stacks.

In order to reach the MoEDAL detector stacks, strangelets produced in nuclear collisions in the LHCb interaction region have to escape from the beam pipe and cross the space to the cavern walls, thus their interaction with matter is important. Besides the ionization produced by their electric charge, different interaction mechanisms were postulated. The existing phenomenological models were developed mostly in connection with the strangelets propagation into the Earth atmosphere, but their basic ingredients could apply to the MoEDAL case too.

In the model proposed by Wilk et al. [15] it is assumed that strangelets fragment during their interaction with matter nuclei, losing mass after each interaction. But, the bulk of unaffected SQM continues its flight with essentially the same velocity (this is in the spirit of the classical spectator participant nuclear interaction models). A rather opposite approach is that of Banerjee et al. [16]. In that model, strangelets interact with the nuclei in their path by picking-up neutrons and protons at different rates, and thus increasing in mass and charge. Such mechanism could be dominant for strangelets with velocities lower than about 0.7c, as for higher speeds the excitation energy would exceed the binding energy and lead to strangelet fragmentation.

Strangelets have never been observed, but some hints concerning their properties could be found in some experimental results. The recent limit on the flux of strangelets in cosmic rays obtained by the SLIM Collaboration [88], combined with the theoretical expectations from strange stars collisions estimated rate in the Galaxy [14] disfavors models as [16], assuming mass and charge increase of strangelets in interaction with nuclei from the traversed matter. We might then expect that the fragmentation processes are dominant, limiting the charge and mass of strangelets possibly arriving to the MoEDAL detectors.

Some experimental indication on the internal structure of SQM could be found in older claims to observe strange dibaryons and in their interpretation. Although the existence of dibaryons (strange or not) was never definitely proven, they could be considered as the simplest multi-quark states, below the lower mass limit for strangelet stability. The reasonable description of the dibaryonic mass spectra observed in (pp), (np) [130] and (λp) systems [131], at few GeV at JINR Dubna, using a modified MIT bag model, based on the assumption of a structure made of a diquark[5] and the clusterization of the other four quarks, could suggest that the strangelet internal structure could me more close to that described in ref. [14].

[5] A bound but unconfined pair of quarks, at least from a phenomenological point of view equivalent to the modern Cooper-like pairing of quarks in some SQM models

Strangelets could be produced in nuclear-nuclear central collisions at LHC. Some of the smallest strangelets would probably continue their flight in the forward direction, arriving to the LHCb detectors, but in the case of very central collisions we might expect the production of large strangelets with masses in the TeV region, which would travel at lower velocities and possibly at larger angles, reaching the MoEDAL detectors.

A.3 Searching for Q-balls

Q-balls are nontopological solitons predicted by minimal supersymmetric generalizations of the Standard Model of particle physics. They are hypothesized supersymmetric coherent states of squarks, sleptons and Higgs fields, and may carry some conserved global baryonic charge Q. There are examples of Q-balls in both gravity mediated [132] and gauge mediated [133] SUSY-breaking models. For generic values of the parameters in these models, Q-balls must have rather large masses, much higher than the electroweak scale, in order to be stable [134] .Although they may be created at the end of inflation, it is less likely that they would appear at the LHC. However, if present, they could manifest themselves as very highly ionising particles that would be registered in the MoEDAL detector. Coupling the scalar field to fermions can make the Q-ball unstable, since decay into those fermions would be possible [135].

A.4 Search for Abnormal Nucleus Production

The possibility that stable or metastable abnormally dense nuclei might exist in nature or might be created in high energy heavy-ion collisions have been hypothesized by several authors [136], [137]. In a particular version of the theory, Lee and Wick [136] proposed a model in which an abnormal nucleus, would have a density several times that of a normal nucleus, a large volume binding energy ($\sim$ 130 A MeV), and a large atomic number , $Z \approx A/2 \gg 100$ To create abnormal nuclei they suggested compressing nuclear matter to a high density in a relativistic nucleus-nucleus collision.

Several attempts to find a trace abundance of abnormal nuclei in nature [138] and to produce them at the Lawrence Berkeley Laboratory Bevalac [139]. Since then, interest has shifted away from searches for abnormal nuclei in heavy-ion studies, due partly to the experimental evidence against the model and partly to theoretical criticism of the model [140]. In a recent calculation for finite normal and abnormal nuclei, Zhang and Li [141] claim that nuclei with $A \geq 86$ may have bound abnormal states and nuclei with $A \geq 165$ may have bound abnormal nuclei with binding energies larger than those of corresponding normal nuclei.

A Proposal for a High-Sensitivity Search for Ultradense Nuclear Matter in 160 A GeV Pb on Pb Collisions at the CERN SPS has already been made [142]. This search could be taken up by the MoEDAL experiment in the event that heavy-ion scenario is possible at the LHCb IP.

B Chemical and Physical Properties of the MoEDAL NTDs

B.1 The Polyallyl Diglycol Carbonate Polymer CR 39

The CR 39 [143] polymer is made by polymerization of diethyleneglycol bisallylcarbonate (ADC) in presence of diisopropyl peroxydicarbonate (IPP) catalyst. The presence of the allyl groups allows the polymer to form cross-links. Thus, it is a thermoset resin. Thermosetting polymer which form random three dimensional cross-linked structures are char-

acterized by being infusible and insoluble in all solvents. The monomer structure is shown in Figure 51. CR 39 is transparent in the visible part of the electromagnetic spectrum. Relevant parameters for CR39 are given in Table 5.

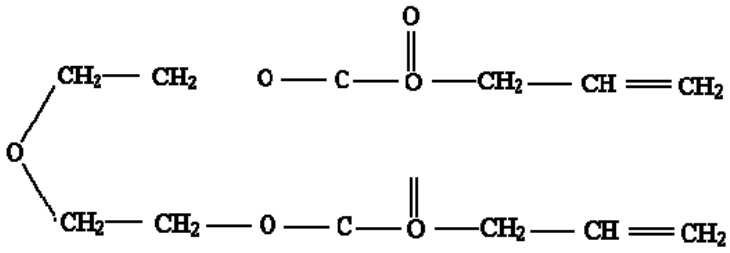

Figure 51: The CR39 monomer.

With a threshold as low as ($Z/\beta \sim 5$) and unique characteristics (high sensitivity, resolution and optical properties) CR 39 is the most convenient track etch detector for the search for ionizing particles, and in particular heavy ionizing particles such as magnetic monopoles, In particular, for one unit Dirac charge ($g = g_D$) CR39 is sensitive to monopoles with $\beta > 10^{-3}$. For magnetic monopoles with $g \geq 2g_D$ [144] [145] CR39 is sensitive over the β-range of $4 \times 10^{-5} < \beta < 1$. The Makrofol(lexan) polycarbonate has a threshold at $Z/\beta \sim 50$; thus they are sensitive only to relativistic and/or multiply charged magnetic monopoles.

Property	Value
Density at 20^oC, g/cm^3	1.31
Refractive index (n)	1.50
Light transmission %	89-92
Meling point at 266 P, ^oC	166
Flash point - Seta closed cup, ^oC	173
Flash point - Cleveland open cup, ^oC	186
Recommended continuous use max. temp., ^oC	100
Recommended 1-hour use max. temp., ^oC	150
Self ignition temp., ^oC	382
Burning rate cm/minute	0.35
Flammability - ASTM D635 1.3 - 2.9 mm thickness, inches/minute	¡1

Table 5: Physical properties of CR39 polymers

B.2 Lexan/Makrofol

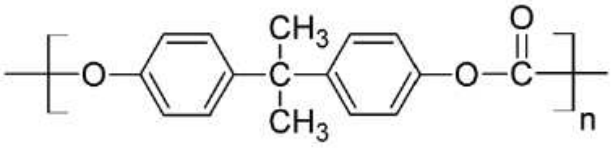

Figure 52: The Lexan monomer.

Lexan and Makrofol are highly durable polycarbonate resin thermoplastics obtained from the polymerization of Bisphenol A (BPA) with carbonyl chloride. The chemical structure is given in Figure 52

The relevant physical properties of lexan are given in Table 6. Such polycarbonates have high light transmission and a high surface uniformity. They are similar to acrylic glass (Plexiglas/Lucite/Perspex) but are far more durable. Due to the large threshold ($Z/\beta \sim 50$) Lexan and Makrofol are mostly used for the search for fast and highly ionizing charged particles.

Property	Value
Density at 20^{o}C, g/cm^3	1.22
Refractive index (n)	1.59
Light transmission %	85-90
Melting point at 266 P, ^{o}C	155
Flash point, ^{o}C	440
Recommended continuous use max. temp., ^{o}C	115
Recommended 1-hour use max. temp., ^{o}C	135
Self ignition temp., ^{o}C	605
Burning rate cm/minute	0.35
Flammability - ASTM D635 1.3 - 2.9 mm thickness, inches/minute	< 1
Flammability -UL	V0-V2

Table 6: Physical properties of lexan polycarbonate

References

[1] A.C. Kraan, J.B. Hansen and P. Nevski, (2005), hep-ex/0511014.

[2] R. Hauser, Eur. Phys. J. C34, s173 (2004).

[3] P. Zalewski, CMS Conference Note, CMS-CR-1999-019.

[4] P.A.M. Dirac, Proc. R. Soc. London, Set. A, 133, 60 (1931); P.A.M. Dirac, Phys. Tev., 24, 817 (1948).

[5] G. Giacomelli and M. Sioli (Astroparticle Physics), Lectures at the 2002 Int. School of Physics, Constantine, Algeria, hep-ex/0211035; G. Giacomelli and L. Patrizii, hep-ex/011209; G.R. Kalbfleisch, Phys. Rev. Lett. 85, 5292 (2000); hep-ex/0005005 ; K. A. Milton et al., hep-ex/0009003; B. Abbott et al., hep-ex/9803023, Phys. Rev. Lett. 81, 524 (1998); G. Giacomelli, Riv. Nuovo Cimento 7 N.12, 1 (1984); M. Acciarri et al., Phys. Lett. B345, 609 (1995); L. Gamberg *et al.*, hep-ph/9906526;

[6] J. Schwinger, Science, Volume 165, Issue 3895, 757 (1969).

[7] B. Koch, Marcus Bleicher, Sabine Hossenfelder, JHEP 0510, 053, (2005); H. Stoecker, Int. J. Mod. Phys. D16, 185 (2007); S. Hossenfelder, B. Koch, M. Bleicher, e-Print: hep-ph/0507140, (2005).

[8] G. B. Gelmini and M. Roncadelli, Phys. Let B99, 411 (1981); R. N. Mohaptra and J. D. Vergados, Phys. Rev. Lett. 47, 1713 (1981); V. barger, H. Baer, W. Y. Keung and R. J. N. Philips, Phys. Rev. D26, 218 (1982); H. F. Gunion, H. E. Haber, G. L. Kane and S. Dawson, "The Higgs Hunters Guide", (Addison Wesley 1990); J. A. Grifols, A. Mendez and G. A. Schuler, Mod. Phys. Lett. A4, 1485 (1989).

[9] L. E. Roberts, Il Nuovo Cimento Vol. 92, N.3, 247 (1986)

[10] Y. D. He and P. B. Price, CERN/SPSLC 95-14 (1995);

[11] Y. D. He, Phys. Rev. Lett. 79, No.17, 3134 (1997)

[12] R. Anishetty, P. Koehler and L. McLerran, Phys. Rev. D 22, 2793 (1980).

[13] H. Heiselberg, Phys. Rev. D 48 (1993) 1418.

[14] J. Madsen, Phys. Rev. Lett 81 (1998) 53.

[15] G. Wilk et al., J. Phys. G 22 (1996) L105.

[16] S. Banerjee et al., Phys. Rev. Lett. 85 (2000) 1384.

[17] S. Coleman, Nucl. Phys. B262, 263 (1985); erratum: B269, 744 (1986); A. Kusenko and M. Shaposhnikov, Phys. Lett. B418, 46 (1998); D. A. Demir, arXiv:hep-ph/9810453v2, (1998).

[18] P. A . M. Dirac, Proc. R. Soc. London 133 (1931) 60; Phys. Rev. 74 (1948) 817.

[19] A. De Rujula, Nucl. Phys. B435 (1995) 257.

[20] Y.M. Cho and D. Maison, Phys.Lett. B391:360-365,1997.

[21] Walter Troost, Patrizio Vinciarelli (CERN) . CERN-TH-2195, Jul 1976. 15pp

[22] T. Banks , M. Dine , H. Dykstra, W. Fischler, Phys.Lett.B212:45,1988.

[23] M. Bertani *et al.*, Europhys. Lett. 12, 613 (1990).

[24] G. Abbiendi *et al.*, Phys.Lett.B663, 37 (2008).

[25] J. Derkaoui et al., Astrop. Phys. 9 (1998) 173.

[26] G. Giacomelli and L. Patrizii, arXiv:hep-ex/0302011, (2003).

[27] V.A. Rubakov, JETP Lett. B219 (1981) 644; G.G.Callan, Phys. Rev. D26 (1982) 2058.

[28] H. Bradner and and W. M.Isbell, Phys. Rev. 114, 603 (1959).

[29] I. R. Kenyont, Rep. Prog. Phys. Vol. 45, (1982).

[30] C. Amsler *et al.*, Review of Particle Physics. By Particle Data Group, Phys. Lett. B667, 1 (2008).

[31] J. K. Yoh *et al.* Phys. rev. Lett. 41, No. 10, 684 (1978).

[32] F. Halzen and D. M. scott, Phys. rev. D21, 131 (1980).

[33] L. E. Roberts, Nuov Cimento 92A, 247 (1986).

[34] A. Abulencia, Phys. Rev. Lett. 49, 102 (1982).

[35] S.P. Martin hep-ph/9709356 (1997); X. Tata hep-ph/9706307 (1997).

[36] J.L. Feng, S. Su and F. Takayama, Phys. Rev. D70, 075019 (2004) 075019.

[37] L. Alvarez-Gaume, M. Claudson and M.B. Wise, Nucl. Phys. B207, 96 (1982); S. Dimopoulos, S.D. Thomas and J.D. Wells, Nucl. Phys. B488, 39 (1997); J.A. Bagger *et al.*, Phys. Rev. Lett. 78, 1002 (1997) 1002; G.F. Giudice and R. Rattazzi, Phys. Rept. 322, 419 (1999).

[38] S. Ambrosanio, G.D. Kribs and S.P. Martin, Phys. Rev. D56, 1761 (1997).

[39] G.F. Giudice and R. Rattazzi, Phys. Rept. 322, 419 (1999).

[40] S. Raby, Phys. Rev. D56, 2852 (1997); H. Baer, K.m. Cheung and J.F. Gunion, Phys. Rev. D59, 075002 (1999); A. Mafi and S. Raby, Phys. Rev. D63, 055010 (2001); S. Raby, Phys. Lett. B422, 158 (1998); A. Mafi and S. Raby, Phys. Rev. D62, 035003 (2000) 035003.

[41] N. Arkani-Hamed and S. Dimopoulos, JHEP 06, 073 (2005); G.F. Giudice and A. Romanino, Nucl. Phys. B699, 65 (2004) 65.

[42] A. Arvanitaki, S. Dimopolous, A. Pierce, S. Rajendran and J. Wacker, arXiv:hep-ph/0506242v2, (2005); A. C. Kraan, arXiv:hep-ex/0506009v1 (2005); S. Bressler, arXiV:hep-ex/0710.2111v3, (2007)

[43] L. Randall and R. Sundrum, Nucl. Phys. B557, 79 (1999) 79, G.F. Giudice *et al.*, JHEP 12, 027 (1998) 027; J.L. Feng and T. Moroi, Phys. Rev. D61, 095004 (2000).

[44] A.J. Barr et al., JHEP 03, 045 (2003).

[45] D.E. Kaplan, G.D. Kribs and M. Schmaltz, Phys. Rev. D62, 035010 (2000); Z. Chacko *et al.*, JHEP 01, 003 (2000).

[46] N.R. Shah and C.E.M.Wagner, (2006), hep-ph/0608140; J.L. Feng, A. Rajaraman and F. Takayama, Phys. Rev. D68, 085018 (2003).

[47] A. Delgado and T.M.P. Tait, JHEP 07, 023 (2005) 023.

[48] W.D. Goldberger, Y. Nomura and D.R. Smith, Phys. Rev. D67, 075021 (2003).

[49] Y. Nomura and D.R. Smith, Phys. Rev. D68, 075003 (2003); Y. Nomura, D. Tucker-Smith and B. Tweedie, Phys. Rev. D71, 075004 (2005); Y. Nomura and D. Tucker-Smith, Nucl. Phys. B698, 92 (2004).

[50] Y. Nomura and B. Tweedie, Phys. Rev. D72,015006 (2005).

[51] C. Friberg, E. Norrbin and T. Sjostrand, Phys. Lett. B403, 329 (1997).

[52] P. Fishbane, S. Meshkov and P. Ramond, Phys. Lett. B134, 81 (1984). P.M. Fishbane *et al.*, Phys. Rev. D31 (1985) 1119.

[53] P.H. Frampton and P.Q. Hung, Phys. Rev. D58, 057704 (1998).

[54] H.J. He, N. Polonsky and S. Su, Phys. Rev. D64, 053004 (2001); R. Barbieri, T. Gregoire and L. J. Hall, hep-ph/0509242 (2005); T. Banks and M. Karliner, Nucl. Phys. B281, 399 (1987).

[55] N. Polonsky and S. Su, Phys. Rev. D63, 035007 (2001).

[56] E. Ma, Phys. Lett. B58, 442 (1975); G. Karl, Phys. Rev. D14, 2374 (1976); F. Wilczek and A. Zee, Phys. Rev. D16, 860 (1977); Y. Ng and S. H. H. Tye, Phys. Rev. Lett. 41, 6 (1978); H. Georgi and S. Glashow: Nucl. Phys. B159, 29 (1979).

[57] H. Tanaka and I. Watanabe: Int. J. Mod. Phys. A7, 2679 (1992).

[58] A.C. Kraan, J.B. Hansen and P. Nevski, hep-ex/0511014 (2005).

[59] A. Nisati, S. Petrarca, G. Salvini, Mod. Phys. Lett. A12, 2213 (1997).

[60] R. N. Mohapatra and J. C. Pati, Phys. Rev. D11, 566 (1975); G. Senjanovic and R. N. Mohapatra, Phys. Rev. D12, 1502 (1975); R. N. Mohapatra and G. Senjanovic, Phys. Rev. D23, 165 (1981).

[61] B. Dutta, R.N. Mohapatra, D.J. Muller, Phys. Rev. D60, 095005 (1999).

[62] P.H. Frampton, Int. J. Mod. Phys. A 13 (1998)2345.

[63] T.G. Rizzo, Phys. Rev. D 25, 1355 (1982); J.F. Gunion, H.E. Haber, G. Kane, S. Dawson The Higgs Hunters Guide, Addison-Wesley (1990); K.Huitu and J. Maalampi, Phys. Lett. B 344, 217 (1995).

[64] G.G. Ross, Grand Unified Theories, Benjamin-Cummins (1985); E. Fahri, L. Suskind Phys. Rep. 74, 277 (1981); E. Eichten et al., Rev. Mod. Phys. 56, 579 (1984); W. Buchmuller, Acta Phys. Austr. Suppl XXVII, 517 (1985).

[65] F. Cuypers and S. Davidson, Eur. Phys. Jour. C 2, 503 (1998).

[66] N. Arkani-Hamed, S. Dimopoulos and G. R. Dvali, Phys. Lett. B 429, 263 (1998); I. Antoniadis, N. Arkani-Hamed, S. Dimopoulos and G. R. Dvali, Phys. Lett. B436, 257 (1998); N. Arkani-Hamed, S. Dimopoulos and G. R. Dvali, Phys. Rev. D 59, 086004 (1999).

[67] Benjamin Koch, Marcus Bleicher, Horst Stoecker, J. Phys. G34, S535 (2007).

[68] I. Antoniadis, Phys. Lett. B 246, 377 (1990); I. Antoniadis and M. Quiros, Phys. Lett. B 392, 61 (1997); K. R. Dienes, E. Dudas and T. Gherghetta, Nucl. Phys. B 537, 47 (1999).

[69] M. B. Voloshin, Phys. Lett. B 518, 137 (2001); Phys. Lett. B 524, 376 (2002); S. B. Giddings, in Proc. of the APS/DPF/DPB Summer Study on the Future of Particle Physics (Snowmass 2001) ed. N. Graf, eConf C010630, P328 (2001).

[70] S. N. Solodukhin, Phys. Lett. B 533, 153 (2002); A. Jevicki and J. Thaler, Phys. Rev. D 66, 024041 (2002); T. G. Rizzo, in Proc. of the APS/DPF/DPB Summer Study on the Future of Particle Physics (Snowmass 2001) ed. N. Graf, eConf C010630, P339 (2001); D. M. Eardley and S. B. Giddings, Phys. Rev. D 66, 044011 (2002).

[71] G. T. Horowitz and J. Polchinski, Phys. Rev. D 66 103512 (2002).

[72] D. N. Page, Phys. Rev. Lett. 44, 301 (1980); G. tHooft, Nucl. Phys. B 256 727 (1985); A. Mikovic, Phys. Lett. 304 B, 70 (1992); E. Verlinde and H. Verlinde, Nucl. Phys. B 406, 43 (1993); L. Susskind, L. Thorlacius and J. Uglum, Phys. Rev. D 48, 3743 (1993); D. N. Page, Phys. Rev. Lett. 71 3743 (1993).

[73] Y. Aharonov, A. Casher and S. Nussinov, Phys. Lett. 191 B, 51 (1987); T. Banks, A. Dabholkar, M. R. Douglas and M. OLoughlin, Phys. Rev. D 45 3607 (1992); T. Banks and M. OLoughlin, Phys. Rev. D 47, 540 (1993); T. Banks, M. OLoughlin and A. Strominger, Phys. Rev. D 47, 4476 (1993); S. B. Giddings, Phys. Rev. D 49, 947 (1994); M. D. Maia, [arXiv:gr-qc/0505119]; V. Husain and O. Winkler, [arXiv:gr-qc/0505153].

[74] C. M. Harris, P. Richardson and B. R. Webber, JHEP 0308, 033 (2003).

[75] Y. Ashie *et al.*, Super-Kamiokande Collaboration,Phys. Rev. Lett. 93, 101801 (2004) and references therein.

[76] R. N. Mohapatra and G. Senjanovic, Phys. Rev. Lett. 44, 912 (1980).

[77] K.Huitu, J.Maalampi, A.Pietila and M.Raidal, Nucl.Phys. B487, 27-42 (1997); M.L. Swartz, Phys. Rev. D40, 1521 (1989).

[78] ALEPH, D. Buskulic et al., Phys. Lett. B303, 198 (1993).

[79] P. B. Price, J. Guiru and K. Kinoshita, Phys. Rev. Lett., 65, 149 (1990)

[80] To be published

[81] M. S. Turner, Phys. Lett. 1158, 95 (1982).

[82] D. E. Groom, Phys. Rep. 140,323 (1986).

[83] G. Bauer, M.J. Mulhearn, C. Paus, P. Schieferdecker, S. Tether, Nucl. Instrum. Meth. A545, 503-515 (2005).

[84] S. Eidelman *et al.*, Phys. Lett. B 592, 1 (2004).

[85] T. Sjostrand, L. Lonnblad and S. Mrenna, arXiv:hep-ph/0108264, (2001).

[86] Benjamin Koch , Marcus Bleicher, Horst Stoecker, J. Phys. G34, S535-542 (2007).

[87] http://lhcb-release-area.web.cern.ch/LHCb-release-area/DOC/gauss/

[88] S. Balestra *eta al.*, Eur. Phys. J C55, 57 (2008); S. Cecchini *et al.* Eur. Phys. C57, 525, (2008).

[89] icnts2008.bo.infn.it/documents/Tuesday-sep2/plenary/Plenary%208%20Benton.ppt

[90] R.L. Fleischer *et al.*, Nuclear Tracks in Solid (U. Berkeley) (1975).

[91] S. Cecchini et al., Radiat. Meas. 34, 55 (2001).

[92] S. Kodaira et al., Proc. of the 20th European Cosmic Ray Symp. 2006.

[93] S. Singh and S. Prasher, Nucl. Instr. and Meth. B 222, 518 (2004).

[94] D. Sinha et al., Radiat. Meas. 33, 139 (2001).

[95] S. Brahimi et al., Radiat. Meas. 43 , S56 (2008).

[96] S. Singh and S. Parsher, Radiat. Meas. 40, 50 (2005).

[97] D. Sinha and K. K. Dwivedi, Radiat. Meas. 36, 713 (2003).

[98] G. Tarl et al., Nature 393, 556 (1981); [S. Cecchini et al., Proc. 28th ICRC (Tsukuba 2003) 3,1657; S. Balestra et al., hep-ex/0602036 (2006); [A. Zanini et al., J. Atmosph. Sol.-Terr. Phys. 67, 755 (2005).

[99] S. Balestra et al., Eur. Phys. J. 55, 57 (2008). S. Balestra et al., Nucl. Instrum. Meth. B 254, 254 (2007); S. Manzoor et al., Radiat. Meas. 40, 433 (2005).

[100] M. Ambrosio et al, Eur. Phys. J. C 25, 511 (2002).

[101] S. Cecchini et al, Il Nuovo Cimento C 24, 639 (2001).

[102] P.B. Price, "Proc. Of the Workshop on Experiments, Detectors, and Experimental Areas for the Supercollider", World Scientific, 899 (1987).

[103] FLUKA: Status and Prospective for Hadronic applications. A.Fasso, A.Ferrari, J.Ranft, P.R.Sala. invited talk in the Proceedings of the Monte Carlo 2000 Conference, Lisbon, October 23-26, 2000, A.Kling, F.Barao, M.Nakagana, L.Tavora, P.Vazeds, Springer-Verlag Berlin, p.955-960(2001).

[104] J.Ranft, DPMJET-II, a Dual Parton Model Event Generator for hadron-hadron, hadron-nuclus and nucleus-nucleus collisions, in Proc. of SARE2 workshop, CERN, October 9-11, 1995, CERN/TIS-RP/97-05/

[105] http://lhcb-background.web.cern.ch/lhcb-background/Radiation/RadLevels.htm

[106] G. Corti, L. Shekhtman, " Estimates of the Remanent Dose Rates in the LHCb Experimental Area", LHCb-2008-045 & EDMS 964229, September 5th (2007).

[107] Safety Code F, "Protection Against Ionizing Radiations, Radiation Safety Manual, Revision 2006, (2006), EDMS no, 335729.

[108] P. Bonnal and D. Forkel-Wirth, "L'approche ALARA au CERN", Note d'information, RGE 9/S5- NI1 (2006), EDMS no. 810169.

[109] Safety Code F, "Protection against Ionizing Radiations, Radiation Safety Manual", Revision 2006, (2006), EDMS no. 335729.

[110] D. Forkel-Wirth, J.-C. Gaborit, E. Cennini, M. Brugger, S. Roesler, H. Vincke, P. Vojtyla and J.Vollaire, "Rapport Provisoire de sûreté du SPS/CNGS et du LHC, Section 11.7, Referentiel de Radioprotection", (2006), EDMS no. 634785.

[111] P. Bonnal and D. Forkel-Wirth, "Criteres et exigences ALARA applicable aux interventions", Note d'information, RGE 9/S5-GSI1 (2006), EDMS no. 810176.

[112] P. Bonnal and D. Forkel-Wirth "Demarche ALARA applicable aux interventions", Note d'information, RGE 9/S5-GSI3 (2006), EDMS no. 825353.

[113] P. Bonnal, "Constitution et convocation du comité ALARA du CERN", Note d'information, RGE 9/S5-GSI2 (2006), EDMS no. 810178.

[114] M. Brugger *et al.*, Radiation Protection Dosimetry, Vol. 116, No. 14, p12, (2005).

[115] M. Fiederle *et al.*, NIM A591, 75, (2008).

[116] LHCb Collaboration. The LHCb Detector at LHC. http:// www.iop.org/ EJ/journal/ -page=extra.lhc/ jinst

[117] D. H. Lacarrère *et al.*, Radiation Shield for LHCb Experiment at Point 8. https://edms.cern.ch/document/111020/1.0

[118] J.C.Batista Lopes *et al.* , Radiation Shielding Wall in the UX85 Cavern. https://edms.cern.ch/document/406875/1

[119]] LHCb Collaboration, S. Amato et al., LHCb Magnet Technical Design Report, CERN-LHCC-2000-007, http://cdsweb.cern.ch/record/424338.

[120]] C.Theis et al, Ambient-dose-equivalent and Field Calibration studies for the final design of the LHCb Shielding. https://edms.cern.ch/document/847155/1

[121] LHCb Web page, Radiation section, http://lhcb-background.web.cern.ch/lhcb-background/Radiation/RadLevels.htm

[122] G.Corti, L. Shekhtman, Simulation of the remanent dose rates in LHCb experimental, https://edms.cern.ch/document/964229/1.0

[123]] LHCb Collaboration, P.R. Barbosa-Marinho *et al.*, Vertex Locator Technical Design Report, CERN-LHCC-2001-011, http://cdsweb.cern.ch/record/504321.

[124] L. Fernandez-Herando *et al.*, The radiation monitoring system for the LHC experimental areas, TS-Note-2004-006, http://cdsweb.cern.ch/record/740728 (2004).

[125] G.Corti, E.Thomas. Private communication. Document in preparation

[126] G. Baur, arXiv:hep-ph/0112239 (2001).

[127] A. J. Baltz and M. Strikman, Phys. rev. D 57, 548 (1998).

[128] E. Witten, Phys. Rev. D 30 (1984) 272.

[129] A. De Rujula and S.L. Glashow, Nature 312 (1984) 734.

[130] C. Besliu et al., J. Phys. G 18 (1992) 807.

[131] L. Popa et al., JINR Rapid Comm. 6[45] (1990) 14.

[132] S. Kasuya and M. Kawasaki, Phys. Rev. D62, 023512 (2000).

[133] S. Kasuya and M. Kawasaki, Phys. Rev. Lett. 85, 2677 (2000).

[134] A. Kusenko and M.E. Shaposhnikov, Phys. Lett. B418, 46 (1998); A. Kusenko *et al.*, Phys. Rev. Lett. 80, 3185 (1998).

[135] A.G. Cohen *et al.* , Nucl. Phys. B272, 301 (1986).

[136] T. D. Lee and G. C. Wick. Phys. Rev. D11, 1591 (1975).

[137] A. R. Bodmer, Phys. Rev. D4, 1601 (1971); A. B. Migdal, Zh. Eksp. Teor. Fiz. 61, 2209 (1971); Phys. JETP 34, 1184 (1972); T. D. Lee and M. Margulies, Phys. Rev. D 11, 1591 (1975); T. D. Lee, Rev. Mod. Phys. 47, 267 (1975); A. I. Chernoustan, G. A. Sorokin and D. N Voskresensky, Pis'ma Zh. Eksp. Teor. Fiz. 24, 507 (1976) (JetP Lett. 25, 465 (1977]; N. K. Glendenning, Nucl. Phys. A469, 600 (1987).

[138] R. J. Holt *et al.*, Phys. Rev. Lett. 36, 183 (1976); S. Frankel *et al.*, Phys. Rev. C 13, 737 (1976).

[139] P. B. Price and J. Stevenson, Phys. Rev. Lett. 34, 409 (1975); K. Frankel and J. Stevenson, Phys. Rev. C 14, 1455 (1976).

[140] A. K. Kerman and L. Dudley Miller (unpublished).

[141] Q. N. Zhang and X. G. Li, Z. Phys. A 343, 337 (1992).

[142] Y. D. He and P. B. Price, "A Proposal for a High-Sensitivity Search for Dirac Magnetic Monopoles and Ultradense Nuclear Matter in 160 A GeV Pb on Pb Collisions at the CERN SPS", CERN/SPSLC 95-14, SPSLC/P288, 27.02.1995

[143] B.G. Cartwright and E.K. Shirk, Nucl. Inst. and Meth. 153, 457 (1978).

[144] J. Derkaoui *et al.*, Astrop. Phys. 9, 173 (1998).

[145] J. Derkaoui *et al.*, Astrop. Phys. 9, 339 (1999).